AGU Advances

Second Revision (Accepted) of

Column-Compound Extremes in the Global Ocean

Joel Wong[1], Matthias Münnich[1], and Nicolas Gruber[1]

[1] Environmental Physics, Institute of Biogeochemistry and Pollutant Dynamics, ETH Zurich, Zurich, Switzerland

Column-Compound Extremes in the Global Ocean

Joel Wong[1], Matthias Münnich[1], and Nicolas Gruber[1]

[1]Environmental Physics, Institute of Biogeochemistry and Pollutant Dynamics, ETH Zurich, Zürich, Switzerland

Key Points:

- Column-compound extremes (CCX)- extremes in multiple parameters within the top 300 m - may reduce habitable space by up to 75%.
- From 1961 to 2020, CCX have become more intense, longer, and occupy more volume, driven by the trends in ocean warming and acidification.
- Triple CCX are confined to the tropics and the North Pacific and tend to be associated with ENSO.

Corresponding author: Joel Wong, joel.wong@usys.ethz.ch

Abstract

Marine extreme events such as marine heatwaves, ocean acidity extremes and low oxygen extremes can pose a substantial threat to marine organisms and ecosystems. Such extremes might be particularly detrimental (i) when they are compounded in more than one stressor, and (ii) when the extremes extend substantially across the water column, restricting the habitable space for marine organisms. Here, we use daily output of a hindcast simulation (1961-2020) from the ocean component of the Community Earth System Model to characterise such column-compound extreme events (CCX), employing a relative threshold approach to identify extremes and requiring them to extend vertically over at least 50 m. The diagnosed CCX are prevalent, occupying worldwide in the 1960s about 1% of the volume contained within the top 300 m. Over the duration of our simulation, CCX become more intense, last longer, and occupy more volume, driven by the trends in ocean warming and ocean acidification. For example, the triple CCX expanded 39-fold, now last 3-times longer, and became 6-times more intense since the early 1960s. Removing this effect with a moving baseline permits us to better understand the key characteristics of CCX, revealing a typical duration of 10-30 days and a predominant occurrence in the Tropics and high latitudes, regions of high potential biological vulnerability. Overall, the CCX fall into 16 clusters, reflecting different patterns and drivers. Triple CCX are largely confined to the tropics and the North Pacific and tend to be associated with the El Niño-Southern Oscillation.

Plain Language Summary

The global ocean is becoming warmer, more acidic, and losing oxygen due to climate change. On top of this trend, sudden increases in temperature, or drops in pH or oxygen adversely affect marine organisms when they cannot quickly adapt to these extreme conditions. These conditions are worse for marine organisms when such extremes occur together in the vertical water column, leading to column-compound extreme (CCX) events, severely reducing the available habitable space. To investigate such CCX, we used a numerical model simulation of the global ocean during the historical period of 1961 to 2020. Singular extreme events are identified primarily with relative percentile thresholds, while CCX require a 50 m minimum depth threshold in the water column. We find that CCX have been increasing in volume, occupying up to 20 % of the global ocean volume toward 2020. We then remove the climate trend to better understand the drivers behind CCX. Many CCX occur in the tropics and high latitudes, lasting 10 to 30 days and reducing habitable space by up to 75 %. This study is the first to systematically detect compound extremes in the water column and may form the basis for determining their detrimental effects on marine organisms and ecosystems.

1 Introduction

Climate change has measurably heated the ocean, increased its acidity, and decreased its oxygen content (Masson-Delmotte et al., 2021). These trends are punctuated by extreme events whose intensities and rapid onsets may impact marine organisms and ecosystems more than slowly evolving trends (Collins et al., 2019; Gruber et al., 2021). The study of marine extremes has emerged strongly in the last decade, with the vast majority of studies focusing on marine heat waves (Hobday et al., 2016; Holbrook, Sen Gupta, et al., 2020; Oliver et al., 2021), their drivers (Holbrook et al., 2019; Sen Gupta et al., 2020), and impacts (Smale et al., 2019; K. E. Smith et al., 2023). Receiving increased attention are extremes in ocean acidity (OAX) (Hauri et al., 2013; Kwiatkowski & Orr, 2018; Negrete-García et al., 2019; Burger et al., 2020; Desmet et al., 2022; ?, ?) and low oxygen (LOX) (Chan et al., 2008; Hofmann et al., 2011; Leung, Mislan, et al., 2019; Köhn et al., 2022), with a particular emerging concern about compound marine extremes, when

conditions are extreme in more than one stressor (Gruber et al., 2021; Le Grix et al., 2021; Burger et al., 2022; Le Grix et al., 2022; Hauri et al., 2024).

Such compounded extreme events can have a large impact on marine biota. When different stressors act synergistically, they can have a disproportionately larger impact than that of individual stressors (Crain et al., 2008; Boyd & Brown, 2015; Pirotta et al., 2022). A well-known example is the increase in aerobic metabolic rates and oxygen demand with increasing temperature (Pörtner & Knust, 2007; Deutsch et al., 2015), making ectotherms especially susceptible to compounded MHW and LOX. Bednaršek et al. (2018) also showed biological implications for pteropods during anomalously high temperature and acidity events (the latter corresponding to anomalously low pH events, with pH = - log[H+], and [H+] being the concentration of the hydrogen ion). Multiple extremes occurring at the same time and place have been explored with properties such as temperature and pH (Burger et al., 2022), temperature and chlorophyll (Le Grix et al., 2021), pH and oxygen (Nam et al., 2011; Köhn et al., 2022), and for triple extremes involving pH, oxygen, and temperature (Gruber et al., 2021).

Warming of the ocean in the past 150 years and the strong trend of ocean acidification have led to substantial increases in MHW and OAX (Oliver et al., 2018; Gruber et al., 2021) and are certain to increase in the future as long as these driving trends continue (Frölicher et al., 2018). For example, Oliver et al. (2018) showed on a fixed baseline approach that between 1925 and 2016, the frequency and duration of MHW increased by 34% and 17%, respectively, resulting globally in a greater than 50% increase in the number of MHW days. For OAX, the trends are even stronger, increasing from a pre-industrial situation of about 4 extreme days a year to a nearly permanent state of extremes (Gruber et al., 2021; Burger et al., 2022). Corresponding trends are also expected for LOX events driven by ocean deoxygenation (Gruber et al., 2021), but global ocean deoxygenation trends tend to be smaller compared to the level of variability, leading to smaller, and not yet well-established trends in LOX. As a consequence of these trends in the single stressor extremes, increasing compound extremes naturally follow. For example, Gruber et al. (2021) attributed the development of widespread double compound extremes in the Northeast Pacific over the past 40 years, and especially the triple compound extreme at the height of the 'Blob' event (2013-2016), in part, to the underlying trends of ocean warming, acidification, and deoxygenation. They speculated that part of the broad ecological impacts of the "Blob" might have been caused by these compound extremes. To better understand the mechanisms driving these extremes, we remove the underlying trends using a so-called moving baseline (Oliver et al., 2021; Burger et al., 2020; Gruber et al., 2021; Burger et al., 2022). Analysis of extremes and especially compound extremes on a moving baseline is also appropriate when considering the impact of these extremes on organisms that have the capacity to adapt to the more slowly evolving changes in temperature, ocean acidification, and oxygen (see also the discussion by Sen Gupta (2023)).

So far, the vast majority of MHW studies have focused on the surface ocean only, although many organisms might have the potential to migrate to colder temperatures at deeper depths when a surface heat wave affects them (Jorda et al., 2020). Furthermore, the habitat of vertically migrating organisms can be considered to include the water column down to about 400 m (Bianchi et al., 2013; Bianchi & Mislan, 2016). Detecting extremes across the vertical dimension is thus an important step towards understanding the compression of habitable space during such extremes. Some MHW studies have looked into the subsurface, (Schaeffer & Roughan, 2017; Elzahaby et al., 2021; Scannell et al., 2020; McAdam et al., 2022; Fragkopoulou et al., 2023; Amaya et al., 2023; ?, ?), while the concept of habitat compression has been considered with respect to temperature and oxygen changes (Jorda et al., 2020; Köhn et al., 2022). However, a consistent definition of compound extremes in the column has yet to be defined. The well-studied

surface MHW may extend into the subsurface, vertically compounding with OAX and LOX to deteriorate the habitable conditions of the water column.

Marine extremes can be driven by various mechanisms, and the study of extremes compounded in the vertical dimension increases the complexity of this task (Gruber et al., 2021). Surface MHW are understood to be driven primarily from the atmosphere through anomalous air-sea heat fluxes, or oceanic processes such as lateral heat advection (Sen Gupta et al., 2020; Holbrook, Sen Gupta, et al., 2020; Marin et al., 2022) and mesoscale eddies (Bian et al., 2023). Such surface MHW may cause higher stratification in the upper ocean, suppressing the upwelling of carbon-rich and low-oxygen waters and hence decreasing the likelihood of surface OAX and LOX. However, temperature anomalies have been shown to influence OAX occurrence by shifting the carbonate chemistry equilibrium (Burger et al., 2022) and increasing or decreasing $[H^+]$ respectively. At depth, vertical or lateral displacement of waters across strong temperature, $[H^+]$, or oxygen gradients tends to be an important driver of subsurface extremes, often coupled with other biological mechanisms (Gruber et al., 2021; Köhn et al., 2022; Desmet et al., 2022)).

Taking into account the various physical, chemical, and biogeochemical processes in the ocean, inferring the mechanisms behind compound extreme events can be a complex task. Extremes that are compounded may share a common driver, be driven by one another, or co-occur in the column with different drivers (Gruber et al., 2021). With percentile thresholds, some detected compound extremes may arise purely out of statistical chance (Burger et al., 2022). Extremes with affiliated drivers have a higher propensity of co-occurrence above such a random signal. Such compound extremes are significant and merit investigation.

Extreme events across the globe have been linked to large-scale climate modes, the dominant one being the El Niño-Southern Oscillation (ENSO) (Santoso et al., 2017; Holbrook, Claar, et al., 2020). The prevalence of ENSO in the study of marine extremes is due in part to the large area it affects in the Pacific, but also to its teleconnections with other ocean basins (Roy & Reason, 2001; Luo et al., 2010). ENSO events are triggered by changes in winds in the eastern tropical Pacific, but they affect many remote regions through connected changes in large-scale ocean and atmospheric circulations (aka teleconnections). Although ENSO might not directly cause the extreme, ENSO-driven changes in the mean state can make the occurrence of extremes more likely or prolong and intensify existing extremes. A good example is the 2013-2015 "Blob" marine heatwave in the Northeast Pacific, which became one of the largest and longest lasting MHW owing to the coalescence of regional circulation changes and ENSO-driven warming (Di Lorenzo & Mantua, 2016; Holbrook et al., 2019; Gruber et al., 2021). ENSO has also been associated with MHW in the Indian and Southern Oceans (Holbrook et al., 2019; Sen Gupta et al., 2020; Oliver et al., 2021). Furthermore, ENSO has been shown to be strongly correlated with OAX and LOX in the Pacific Ocean, especially at depth (Turi et al., 2018; Leung, Thompson, et al., 2019; Köhn et al., 2022; ?, ?).

Here, we extend the existing work on marine extremes by simultaneously expanding our analysis in two directions. We expand in depth by analyzing extremes across the upper water column, and we expand in terms of stressors by focusing on compound events. Thus, we will define and characterise column-compound extreme events in the vertical water column at the global scale, and aim to understand their drivers. To this end, we will use results from a hindcast simulation undertaken with a global ocean coupled physical-biogeochemical model, sampled at high temporal frequency to permit us to identify extremes. We rely on model simulation results, since there are no observational records available across all parameters or depth that would permit us to undertake this study.

We also develop a framework to analyze such events, which we call Column-Single eXtreme events (CSX) in the case of a single parameter being extreme across a good portion of the water column, and Column-Compound eXtreme events (CCX) when more

than one CSX is detected in the same column at the same time. We will show that these events are prevalent in the ocean, primarily occurring at low latitudes, and that their frequency, duration, and intensity have increased in recent decades. Although we cannot yet identify the potential impacts of these extremes on marine organisms and ecosystems, the compounding of extreme conditions in the water column may have a detrimental effect. We will show the places and times where these column extremes tend to occur, giving insight into where and when one should look for these potential ecological impacts.

2 Detecting Extreme Events in the Water Column

No consistent definition of single or compound marine extreme events exists so far, much less if they are co-occurring in the same vertical column. We thus first review the issues at hand and then illustrate the framework we have used to identify the Column-Single eXtreme events (CSX) and the Column-Compound eXtreme events (CCX).

A common issue to be resolved in all studies is the choice of thresholds and baselines. Regarding the threshold, MHW-related studies have relied on a relative percentile threshold approach, with the majority of studies using a seasonally-varying threshold (Oliver et al., 2018; Holbrook, Sen Gupta, et al., 2020), so that extreme conditions can be detected regardless of the season. On the contrary, absolute thresholds remain pertinent to extremes such as LOX, where the metabolic requirement for organisms tends to be fixed (Hofmann et al., 2011), with some degree of variability with temperature (Seibel, 2011; Deutsch et al., 2015). Absolute thresholds have also been used to detect extremes in aragonite saturation state (Hauri et al., 2013; Negrete-García et al., 2019; Desmet et al., 2022), where a thermodynamic threshold determines the state of dissolution of the shells of calcifying organisms. Thus, there are clear grounds for using either relative or absolute thresholds, and we make use of both in this study.

The baseline, that is, the time period used to identify thresholds, is also a critical choice in detecting extremes (Jacox, 2019; Oliver et al., 2021; Sen Gupta, 2023). In the case of a fixed baseline, the thresholds remain invariant, such that trends in temperature, pH, and oxygen imply an increase in the frequency and intensity of extreme events (Gruber et al., 2021). This could be problematic when cold spells in subsequent years are potentially marked as heatwaves (Jacox, 2019), or when waters become classified as permanently extreme with respect to ocean acidification (Hauri et al., 2013; Burger et al., 2020, 2022; Gruber et al., 2021). An alternative is the use of a moving baseline, that is, where the reference period used to identify the relative thresholds is shifting in time with the analysis, or where the thresholds are computed based on detrended data. An analysis with such a moving baseline gives equal weight to extreme events throughout the time period (Burger et al., 2020; Rosselló et al., 2023), and is more suitable for the investigation of drivers (Chiswell, 2022). It is also more relevant to organisms that are able to adapt to the gradually changing conditions (Holbrook, Sen Gupta, et al., 2020; Oliver et al., 2021), but are still affected by sudden changes in conditions during an extreme event. In this study, we first present our results on a fixed baseline, illustrating the response of extreme events to the climate trend. Then, we primarily use the moving baseline to analyse extreme events and postulate drivers. A quadratic moving baseline is chosen to fit the long-term trend in the three variables (Hauri et al., 2021) (Text S1 and Figures S1-S2).

The next choices concern the vertical structure and compounding of the stressors. For the vertical structure, we define columns to be Column-Single eXtreme events (CSX) of a particular type (MHW, OAX, or LOX) when the grid cells considered extreme with respect to this particular parameter occupy more than 50 m of the upper 300 m of the water column. For the compounding, we identify columns to be Column-Compound eXtreme events (CCX) when more than one CSX is detected in the same column at the same

time. This leads to three types of double stressor CCX, that is, MHW-OAX, MHW-LOX, and OAX-LOX, and one type of triple stressor CCX, i.e., MHW-OAX-LOX.

In Figure 1a, a conceptual sketch of the various types of defined extremes is shown for a single column over time. Grid cell extreme events are coloured within the time-depth diagram, where they occur. However, this does not necessarily mean that a column extreme is occurring. For example, a CSX-MHW starts at day 20 from the surface, while a CSX-OAX and CSX-LOX start from the bottom of the column at days 35 and 47 respectively. The durations of the CSX and CCX are marked with arrow ranges below Figure 1b.

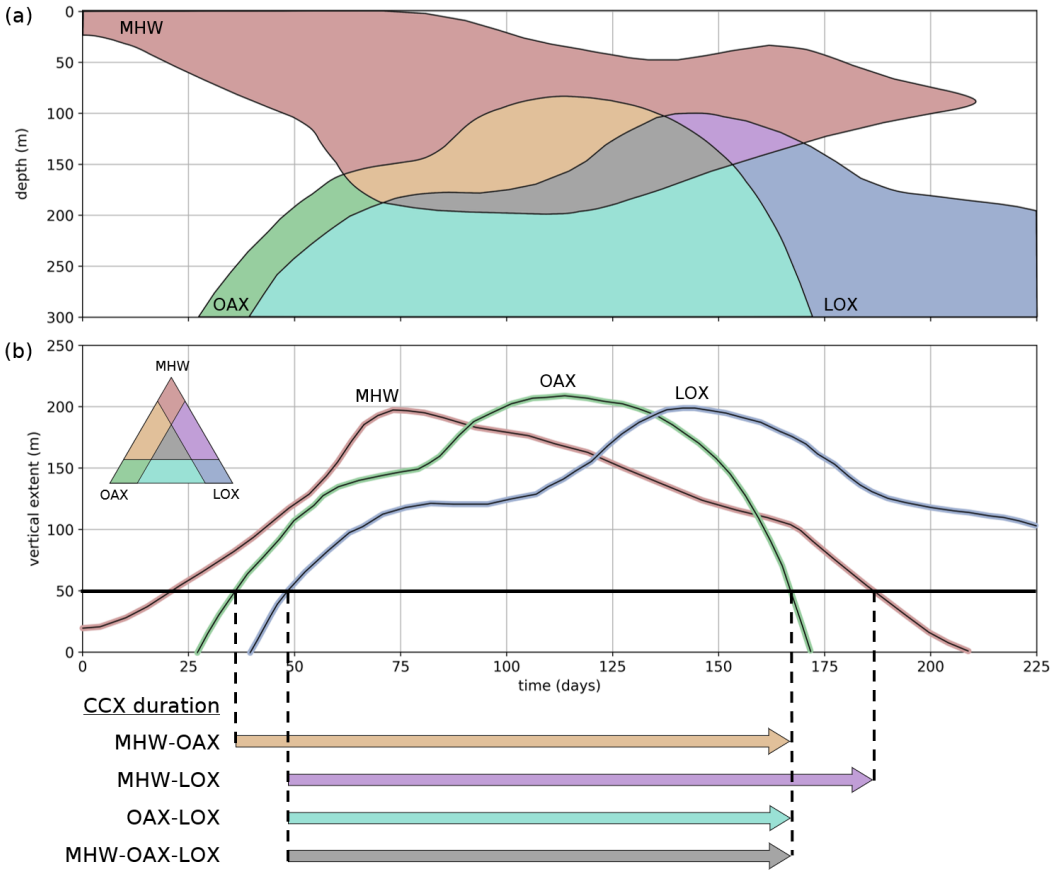

Figure 1. Illustration of the concepts used to detect and analyze column compound extremes. (a) Idealized diagram illustrating the time-depth evolution of extreme conditions in a hypothetical water column from the surface down to 300 m depth. The coloured regions within the plot are considered extreme, with the colours brown, green and blue representing pure MHW, OAX and LOX, respectively. The areas where the different extremes overlap are given colours according to the mixing diagram in panel (b). (b) Timeseries of the total vertical extent (within the top 300 m of the water column) for each extreme type. When the vertical extent for a particular type of extreme exceeds 50 m, we call it a *Column-single eXtreme event* (CSX) of this parameter and when more than one of these occur at the same time a *Column-Compound eXtreme event* (CCX). The duration of the four different types of CCX is indicated by arrows.

3 Methods

3.1 Model Simulations

To identify the CSX and CCX, we used results from a hindcast simulation performed with the ocean component of the global Community Earth System Model (CESM) Version 1.2 (Gent et al., 2011). The ocean component consists of the Parallel Ocean Program 2 (POP2) (R. Smith & Gent, 2010) that simulates ocean circulation and mixing, the Community Ice CodE 4 (CICE4) model, also known as the Los Alamos Sea Ice Model (Hunke & Lipscomb, 2008) simulating the presence and thickness of sea ice, and the Biological Elemental Cycling (BEC) model (Moore et al., 2004, 2013) representing ocean ecology and biogeochemistry. The model has a nominal meridional resolution of 0.5° near the poles, refined to 0.3° at the equator, and a nominal zonal resolution of 1°. There are 60 depth levels in the vertical dimension, extending from the surface to 5375 m. BEC includes three phytoplankton functional types that are grazed by one zooplankton type. Temperature and dissolved oxygen fields are prognostic variables of the coupled model, while the hydrogen ion concentration (on the total scale) was obtained from the simulated inorganic carbon parameters by applying calculations of the carbonate system based on the OCMIP2 routines (Orr et al., 2005). Details of the model can be found in Yang and Gruber (2016).

The model simulation started from a spun-up preindustrial state (Yang & Gruber, 2016) and was brought forward from 1850 to 1957 with cyclically repeated 3-hourly atmospheric forcing from the Japanese 55-year Re-analysis (JRA-55) product (Ebita et al., 2011) and atmospheric CO_2 prescribed according to observations provided by the Global Carbon Project (Friedlingstein et al., 2022). The hindcast simulation was then produced with daily output for the years 1958 to 2020 also using the historical JRA-55 forcing. To allow the ocean state to relax from the cyclic atmospheric forcing during the spinup, we discard the first three years and limit our analysis to the 60-year period between 1961 and 2020. The results of this simulation were also used for the Global Carbon Budgets 2020 and 2021 (Friedlingstein et al., 2022) in Hauck et al. (2020) and in RECCAP2 papers DeVries et al. (2023); Hauck et al. (2023).

3.2 Extreme Events Detection

In the first step, single extreme events of MHW, OAX, and LOX are detected for each grid cell for each day. For MHW and OAX, a 95th percentile threshold is applied to temperature and $[H^+]$, respectively, using seasonally-varying thresholds. For LOX, we require the oxygen concentration to be below the 5th percentile value (again seasonally varying), after which values above 150 μM ($\sim$ 3.5 ml/L) are masked. The absolute threshold for LOX was added because LOX at high oxygen levels have very little biological impact. The chosen value is the hypoxic threshold of some larger fish species such as yellowfin and skipjack tuna, marlin, and sailfish (Braun et al., 2015; Leung, Mislan, et al., 2019; Rose et al., 2019). The absolute threshold for LOX is applied directly on the (non-detrended) model output. The detection thresholds for single events in the grid cell are summarised in Table 1. In this work, we do not impose additional criteria, such as minimum duration (Hobday et al., 2016), since one goal of this study is to identify drivers behind exceedances of the threshold. For fixed baseline thresholds, the data are detrended with a quadratic trend to a reference year of 1958 prior to computing the percentile thresholds. For the moving baseline results, the thresholds change with time with respect to the fitted quadratic trend. A detailed description of the detrending for fixed and moving baselines and the computation of thresholds can be found in Text S1.

Table 1. Single extremes and the thresholds used for their detection

Single Extreme Type	Variable	Percentile Threshold	Additional Absolute Threshold
Marine Heatwave (MHW)	T	$> 95^{\text{th}}$	-
Ocean Acidification Extreme (OAX)	$[H^+]$	$> 95^{\text{th}}$	-
Low Oxygen Extreme (LOX)	$[O_2]$	$< 5^{\text{th}}$	$< 150\,\mu$M

To define extreme events in the vertical column, we require that at least 50 m of the top 300 m be extreme with respect to each stressor. The analysis range of 300 m reflects the vertical habitat range of epipelagic and other vertically migrating organisms (Bertrand et al., 2010; Bianchi et al., 2013; Bianchi & Mislan, 2016). This choice is arguably somewhat subjective, but it encompasses the depth range of the vast majority of marine organisms. The value of the minimum extension of 50 m is also subjective, but aims to capture the occasion when a substantial fraction of the water column is extreme, affecting the organisms that live within this water column in a major way. Adjusting this minimum extension modulates the number of column extremes detected, but does not significantly change their spatial or temporal distribution (Text S2 and Figures S3-S6). When the 50 m vertical threshold is met for a single stressor, it is denoted as a column-single extreme event (CSX), illustrated in Figure 2a. The criteria for a CCX are met when two or more CSX occur in the same vertical column at the same time. Various configurations of CCX are illustrated in Figure 2b. CSX can be located separately in column (c) or have some overlap (e). The single extreme grid cells do not need to be vertically connected to meet the 50 m threshold, as seen in (b) and (d).

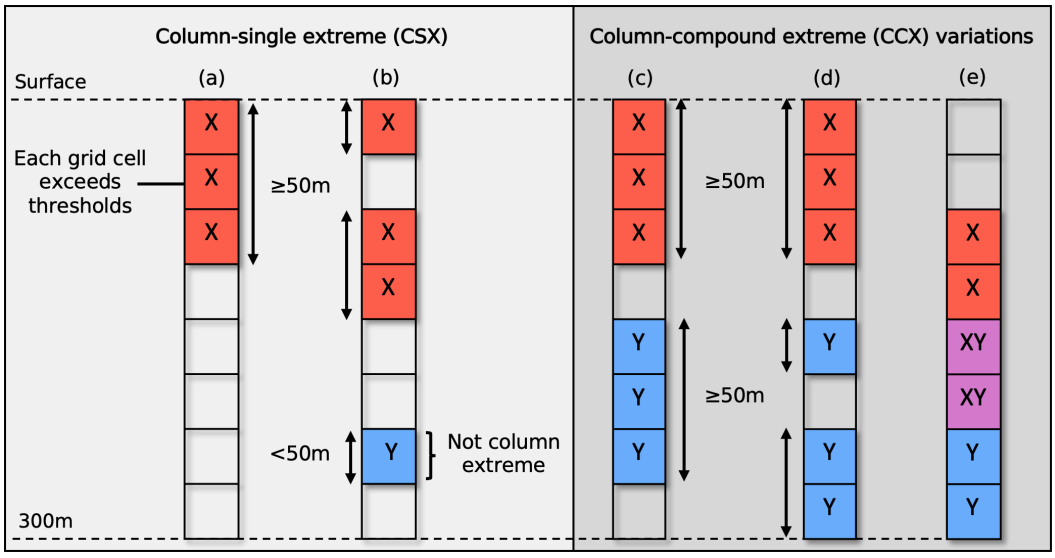

Figure 2. Illustration of different types of column-extreme events within the water column. (a) Column-single extreme (CSX), (b) CSX with discontiguous grid cells of extreme type 'X', (c) Column-compound extreme (CCX), (d) CCX with discontiguous grid cells of extreme type 'Y', (e) CCX with overlapping 'X' and 'Y' type extremes.

3.3 Extreme Event Metrics

The metrics used to characterise extreme events can be broadly grouped into frequency, intensity, and duration categories. Regarding the extremes in the vertical column, we also quantify their size, location, and remaining contiguous habitable space (see Table 2). Although many of these metrics are commonly used in extreme studies, some had to be redefined in the context of our work on column extremes. We do not include severity in our analyses, that is, the cumulative sum of the intensity value over the duration of the event (Hobday et al., 2016; Hauri et al., 2013; Samuels et al., 2021), since it strongly correlates with the event duration in our analyses. Note that triple CCX are also double CCX and are thus included in their metrics.

Table 2. Metrics used in the analysis of extreme events

Name	Symbol	Definition
Frequency metrics		
Days per year	N	Mean number of extreme days per year
Co-occurrence propensity	CP	Likelihood of two or more CSX occurring within the same vertical water column at the same time
Enhancement (Suppression) of CCX during ENSO	ΔN	Mean increase (decrease) in the number of extreme days per year during ENSO events, compared to that in the neutral phase
Intensity metrics		
Intensity index	ψ_i	Ratio of an event variable's i difference from its climatological value to the difference between the threshold and the climatological value.
Compound intensity index	Ψ	Square-root of the sum of squares of the intensity index of individual events that make up a compound event
Maximum intensity index	$\psi^{\max}$	Maximum value of the intensity index over time and the vertical column
Duration metrics		
Duration	D	Lifetime of an event for which the thresholds are met continuously
Size and location metrics		
Volume fraction	f_V	Fraction of total volume (top 300 m) of a defined region that is affected by extremes at any time
Vertical fraction	f_z	Fraction of top 300 m of a column occupied by extremes during a column extreme event
Contiguous habitable space fraction	f_h	Fraction of the top 300 m within a column contiguously unaffected by extremes during a column extreme event

The duration of an event refers to the total length of time for which the specified extreme type exists in the water column. For example, a MHW-OAX event starts from the time CSX-MHW and CSX-OAX both exist in the water column, even if the CSX-MHW started earlier (see Figure 1). The same applies to the end of a CCX.

The intensity index expresses the strength of an extreme event in a unitless way. It is inspired by the MHW categories of Hobday et al. (2018), and defined as the con-

tinuous severity index by Sen Gupta et al. (2020). Using the intensity index as a measure of event intensity permits us to compare the intensities of multiple extremes and even combine them. For a single grid cell, it is expressed as:

$$\psi_X = \frac{X - X_c}{X_t - X_c}, \tag{1}$$

where X is the parameter of interest, X_c is its climatological value for that day of the year, and X_t is the threshold value. For the climatology, we use the median value to avoid instances where it is skewed by exceptionally intense extreme events. The median value is obtained from a seasonally varying 11-day rolling window. To express the intensity index of multiple extremes occurring in the same grid cell, we take the Euclidean norm of ψ of the single extremes:

$$\Psi = \sqrt{\psi_X^2 + \psi_Y^2 + \psi_Z^2}, \tag{2}$$

where ψ_X, ψ_Y, and ψ_Z are the intensity index values of single extremes.

The co-occurrence propensity (CP) is a central metric for the study of compound extremes, as it allows us to assess whether two extremes co-occur by chance, or whether they co-occur as a result of a common process forcing them. Likewise, the propensity can be used to assess whether two extremes co-occur much less frequently than expected by chance, since the process forcing one extreme may lead to conditions that suppress its co-occurrence with another. The CP metric is defined as the likelihood that two (or three) different CSX occur in the vertical column at the same time. It is scaled to the range of [-1,1]. A value of 1 indicates that the CSX occur together as often as the global maximum occurrence, while a value of -1 indicates that they never occur together. A value of 0 suggests that their occurrences are independent, as if randomly distributed in time. A positive value suggests that the CSX in consideration have similar or related drivers, while a negative value suggests that they have opposing drivers.

First, the independent (random) value of CCX days per year is computed using the mean number of CSX days per year:

$$N_r = \begin{cases} \frac{N_1}{D_Y}\frac{N_2}{D_Y} \times D_Y, & \text{for double extremes,} \\ \frac{N_1}{D_Y}\frac{N_2}{D_Y}\frac{N_3}{D_Y} \times D_Y, & \text{for triple extremes,} \end{cases} \tag{3}$$

where N_1, N_2, N_3 are the mean number of days per year of different CSX, and $D_Y = 365$ is the number of days in a year. The CP metric is then defined as:

$$\mathrm{CP} = \begin{cases} \frac{N - N_r}{N_{\max} - N_r}, & N \geq N_r \\ \frac{N - N_r}{N_r}, & N < N_r \\ 0, & N_r = 0 \end{cases} \tag{4}$$

where N is the mean number of days per year of the CCX, and $N_{\max}$ is the global maximum value of N. The CESM hindcast does not simulate leap years. The CP metric is similar in concept to the likelihood multiplication factor (LMF) (Zscheischler & Seneviratne, 2017; Burger et al., 2022), but differs in that the maximum value of CP is 1.0, giving us the view of how far away a grid cell is from the highest global occurrence of the CCX. On the other hand, the LMF value directly indicates the change in likelihood of compound events.

The fraction of contiguous habitable space is calculated by identifying vertically connected non-extreme grid cells within the column. This metric quantifies the amount

of space within the 300 m deep column an organism can inhabit before it encounters waters under extreme conditions. An organism that performs diel vertical migration may not be impacted if 25 % of the column is extreme at the bottom of the column. However, if these extreme conditions occur in the middle of the column, the organism is more likely to encounter extreme conditions during its migration.

3.4 Clustering of Extremes

To find commonalities of the detected CCX with regard to their vertical structure and to help us identify the underlying drivers, we cluster the detected CCX with a k-means clustering approach (MacQueen, 1967). The clustering algorithm is performed on the vertical locations of single extreme events in the column, exclusively during CCX and for grid cells with a positive co-occurrence propensity. In detail, the water column is first divided into 6 bins of 50 m each, and then, over the 60-year analysis period, the number of occurrences of single extremes in each bin during CCX is counted and weighted by their intensity index. These bins of vertical locations are then used as the clustering dimensions, with 12 dimensions for the double CCX and 18 dimensions for the triple CCX. These dimensions are chosen as the vertical locations of single extremes reflect the conditions under which they occur and allude to their drivers. More information on the clustering approach and the choice of the number of clusters is provided in Text S3 and Figure S19.

3.5 Model Evaluation

Given our reliance on model simulation results for detecting single and compound extremes across the upper water column, it behooves us to evaluate the model with regard to its ability to represent extremes. However, our evaluations are largely limited to the surface. For MHW, we used daily observations of sea-surface temperature from the Optimally Interpolated Sea Surface Temperature (OISSTv2) product (Huang et al., 2021) covering the period 1982 to 2020. For OAX, we relied on the OceanSODA-ETHZ dataset (Gregor & Gruber, 2021) that covers the period 1982 to 2020. Surface daily MHW and monthly OAX are detected in the observational products with a seasonally-varying 95th percentile threshold on a quadratic moving baseline, analogous to how this was done for the model output (see Section 3.2). Furthermore, the climatological distributions of pH and $[O_2]$ are evaluated with respect to the Global Ocean Data Analysis Project for Carbon (GLODAPv2) (Lauvset et al., 2016) and Gridded Ocean Biogeochemistry from Artificial Intelligence (GOBAI-O2) (Sharp et al., 2022) respectively. In particular, we evaluated the depths where $[O_2] = 150\,\mu$M since this value is used as an absolute threshold in this study. As the El Niño-Southern Oscillation (ENSO) turns out to be a major driver for the variability in extremes, we also evaluate the model with respect to ENSO, using the Oceanic Niño Index (ONI) and the depth of the 20 °C isotherm across the equatorial Pacific.

The model captures the observed variations and global coverage of surface MHW with high fidelity (Figure 3(a)). In particular, the model captures well the strong year-to-year fluctuations, which tend to be closely coupled to ENSO, for example, in the years 1998 and 2015-2016. The model also correctly simulates the spatial pattern of the mean duration of these surface MHW (Figure 3(b-c)). However, the model overestimates the duration across the globe, particularly in the eastern tropical Pacific (Figure 3(d)). This is a common shortcoming of models for reasons not yet established firmly (Frölicher et al., 2018; Gruber et al., 2021; ?, ?). It is also possible that observations tend to underestimate the duration due to observational gaps (Gruber et al., 2021). We also need to point out that the MHW durations reported here on the basis of OISSTv2 tend to be shorter than those reported elsewhere on the basis of the same data (Oliver et al., 2018; Holbrook et al., 2019). This is due to our use of a higher percentile threshold and not filling in gaps between events (Hobday et al., 2016). Finally, the model represents well

the distribution of surface MHW intensities (Figure 3 (e-f)), with higher intensities seen in the equatorial and temperate regions. It underestimates the mean annual maximum intensity almost everywhere by about 0.3 °C (Figure 3(g)), likely a result of our using a relatively coarse resolution model, except in the eastern tropical Pacific where it overestimates the intensity by up to 0.6 °C in a small area.

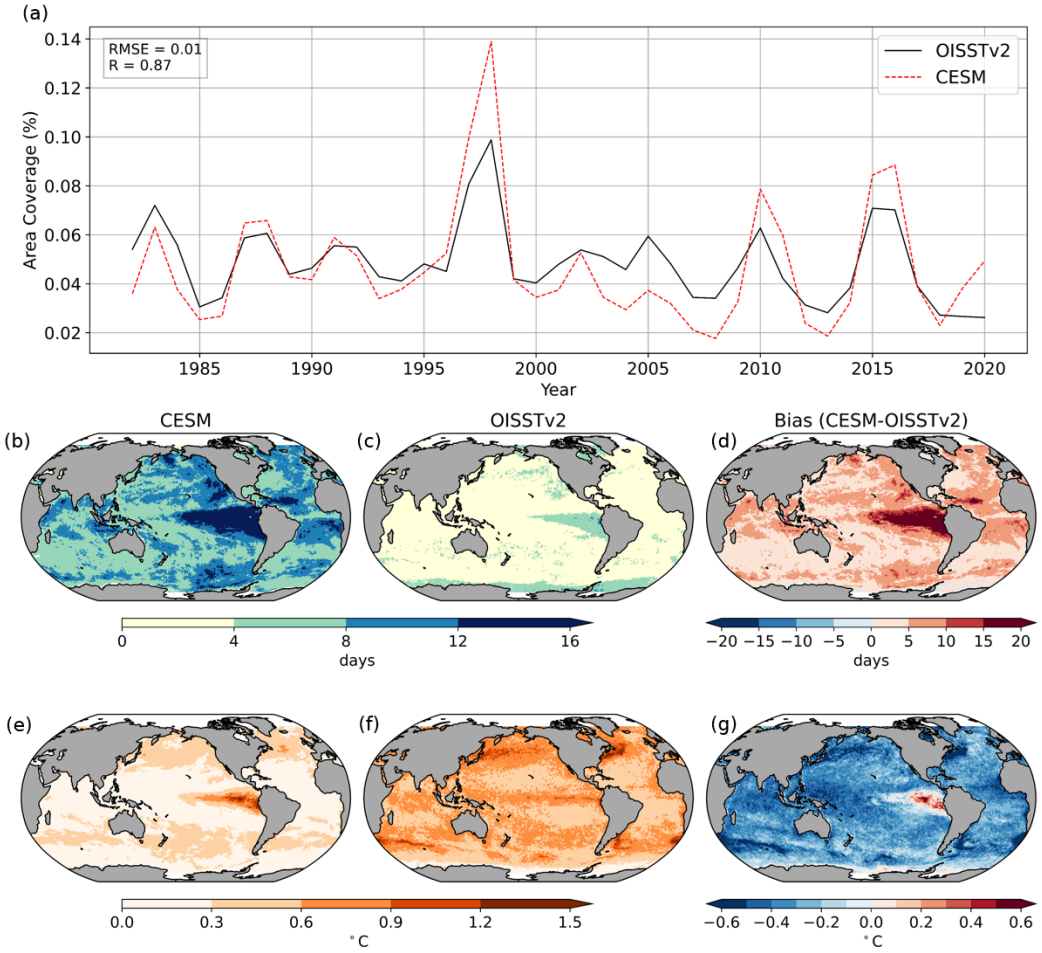

Figure 3. Evaluation of the hindcast model CESM with regard to its representation of surface marine heatwaves (MHW).(a) Timeseries of annual global area coverage of surface MHW identified by the OISSTv2 observational product compared to those diagnosed in the CESM hindcast. (b) CESM and (c) OISSTv2 mean duration of surface MHW and (d) the corresponding bias. (e) CESM and (f) OISSTv2 mean annual maximum MHW intensity and (g) the corresponding bias. The MHW were diagnosed in the observations in the same manner as done for the model.

The evaluation of surface OAX with the observation-based product OceanSODA-ETHZ (Gregor & Gruber, 2021) confirms the fidelity of the model simulations, but also reveals more differences than those seen for surface MHW. However, one needs to note that the uncertainties associated with this product are much larger than those associated with SST. This is a consequence of the several orders of magnitude fewer observations available to construct the space-time distribution of $[H^+]$. Still, the model-based time-series of the global area coverage of surface OAX (based on $[H^+]$) agrees remarkably well with that inferred from the observation-based product, both in terms of mean

and year-to-year variations (Figure 4(a)). However, the peak values differ by up to about 50%, with this difference especially apparent in the years 1988-1989 and 1997. The surface OAX detected with CESM have a spatial pattern similar to that inferred from the observation-based product, especially with regard to the locations of the longest and most intense OAX found in the tropical Pacific (Figure 4(b-c) and (e-f)). However, there is a mismatch in the high latitudes, especially in the North Pacific and the Southern Ocean, where the model identifies long-lasting and intense surface OAX, whereas they are not detected in the observation-based product. We suspect that this difference is probably a consequence of the observation-based product underestimating the variability of $[H^+]$ (Ma et al., 2023), thus detecting shorter and less intense OAX. It may also be a consequence of biases in the model and should be taken into account during the analysis. Regardless, biases in intensity tend to have a minor effect on most conclusions drawn in this study, especially those related to the propensity or mechanisms of OAX. However, biases in intensity will impact derived metrics such as the compound intensity index of compound-OAX.

We also evaluate the model's ability to reproduce the climatological distributions of pH and $[O_2]$ at various depths, since they are less directly related to the forcing applied to the model. Overall, we find that the model captures well the spatial distribution of pH and $[O_2]$ (Figures S7-S10). In general, the biases are low, about $\pm 40\,\mu$M for $[O_2]$ and ± 0.1 for pH. With the exception of pH on the surface, we find a high correlation ($R > 0.8$) for both properties at all depths. In certain regions such as the oxygen-deficient zones (ODZs) and the Southern Ocean, we find an increasing bias with depth, up to $\pm 60\,\mu$M for $[O_2]$ and ± 0.4 for pH. The sign and location of the biases between the two properties are similar, suggesting that they probably arise from physical properties such as stratification and the depth of the thermocline, or biological processes such as remineralisation and sinking rates of particulate organic carbon (POC). For example, a positive bias in the Pacific upwelling regions indicates a deeper oxycline in the hindcast, which may have resulted from too much mixing at the surface. Examining the seasonal variability of $[O_2]$ (Figure S11), we find that the model reproduces the relative changes well on a monthly time scale and therefore accurately represents the seasonal variations of physical and biogeochemical cycles.

Although the absolute value of the bias is less important for relative thresholds in extremes, we use an absolute threshold of $150\,\mu$M for $[O_2]$ in this study and hence conduct a further evaluation of the hindcast. The depths at which $[O_2] = 150\,\mu$M (Figures S12-S13) are typically deeper by about 30 m in the hindcast especially at the location of ODZs, confirming our observations in the previous paragraph. This bias reverses in the western tropical and north Pacific, where the hindcast reaches $150\,\mu$M at a shallower depth of about 30 m. These biases, although generally low, may potentially include or exclude LOX in the hindcast, especially near the boundaries of the absolute threshold.

The hindcast model simulates the time-series of the Oceanic Niño index ONI well with a bias of 0.11 °C, and a correlation coefficient of $R^2 = 0.91$, based on ORAS5 (Zuo et al., 2019)). It also replicates the variation of the thermocline structure in the eastern Pacific. Concretely, we assess the ability of the model to reproduce the depth of the 20 °C isotherm at monthly resolution (Figure S14). The interannual variability of the isotherm depth is comparable between the two, and the time scales of ENSO events are similar. We find a weaker zonal gradient in the CESM hindcast with a deeper thermocline in the east and shallower in the west. Overall, we conclude that the hindcast model is capable of capturing not only the mean state of the ocean's physical and biogeochemical state, but also its variability, which is a critical requirement for investigating extremes.

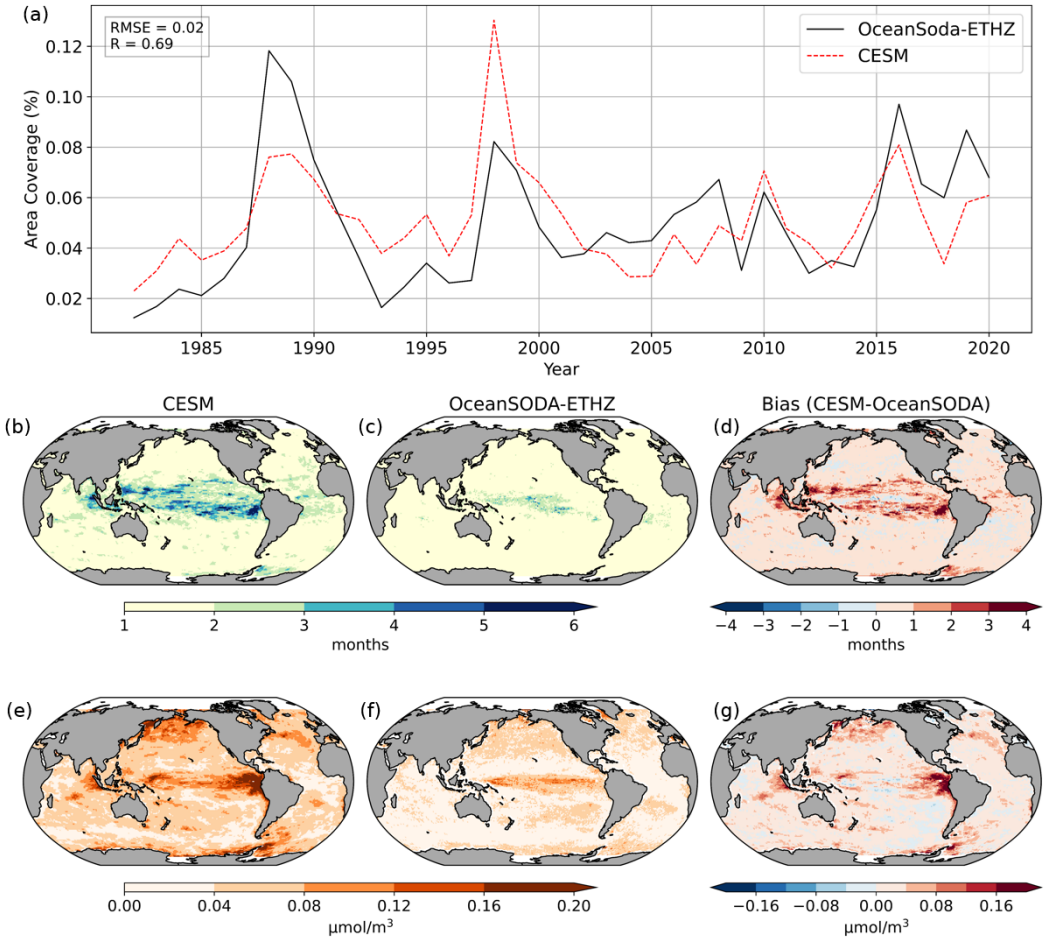

Figure 4. Evaluation of the hindcast model CESM with regard to its representation of surface ocean acidification extreme events (OAX) (a) Time-series of annual global area coverage of surface OAX identified on the basis of the OceanSODA-ETHZ observational product (Gregor & Gruber, 2021) compared to those diagnosed in the CESM hindcast. (b) CESM and (c) OceanSODA-ETHZ mean duration of surface OAX and (d) the corresponding bias. (e) CESM and (f) OceanSODA-ETHZ mean annual maximum OAX intensity and (g) the corresponding bias.

4 Results and Analysis

4.1 Trends of Column Extremes

The volumes occupied by all single-parameter column extremes are modeled to have increased substantially over the 60 years of our analysis (Figure 5a). Extreme volume fractions started from values of a few percent in the 1960s and doubled for LOX, more than quadrupled for MHW to more than 20 % and reached almost 100 % for OAX at the end of the simulation in 2020. As these metrics were calculated with a fixed baseline reflecting the conditions of the 1950s, these increases are a direct consequence of the underlying changes in temperature, oxygen, and acidity. Specifically, averaged over the top 300 m, temperature increased by 0.18 °C, $[H^+]$ increased by 1.56 μmolm^{-3}, and $[O_2]$ decreased by 1.18 μM between the first and last decade (Figure S15-S16). The rapid changes in OAX and the more moderate increases in MHW diagnosed for the column extremes

mirror the results obtained for the surface (Oliver et al., 2018; Burger et al., 2020; Gruber et al., 2021). This reflects the fact that ocean warming and ocean acidification are not limited to the surface, but extend over much of the upper ocean (Gleckler et al., 2016; Kwiatkowski et al., 2020), causing strong trends also in column extremes. The trend is particularly strong for the volume fraction of OAX, reflecting the rapid forcing through ocean acidification relative to the magnitude of the natural variability of $[H^+]$, an effect seen in previous work (Burger et al., 2020; Gruber et al., 2021). The trend of the LOX volume fraction is comparatively muted due to smaller global trends in oxygen. Furthermore, the trend in $[O_2]$ is not homogeneous across the globe and could be increasing or decreasing in certain basins, leading to a muted global average trend. The overall volume fraction of LOX is also relatively smaller in magnitude compared to the other CCX due to the additional absolute threshold of 150 μM used in this study.

The increasing volume fraction of single parameter CSX also causes the volume fraction of column compound extremes (CCX) to increase, but the increases are less steep and also not as monotonic (Figure 5b). In the 1960s and 1970s, the volume fractions of the different combinations hover around $0.1-2\,\%$, with OAX-LOX events being the most prevalent at around 1 %, and the triple compound extreme occupying less than 0.1 % of the water column, on average. Then at various points in time, the prevalence of these CCX suddenly increased. In the case of the MHW-OAX events, this occurred around 1980 with a relatively steady growth thereafter, reaching a volume fraction of nearly 50 % in 2020. The volume fraction of OAX-LOX more than doubled in 1998, and then remained fairly constant near 10 %. The smallest increases are seen for the volume fraction of MHW-LOX and MHW-OAX-LOX, but they still increased 4.5 and 32 times when comparing the first and last 20 years.

As the volume of CCX has increased over the last 60 years, their duration has also increased (Figure 5c). MHW-OAX and OAX-LOX events lasted on average less than 50 days before $\sim$1995, but saw a sudden increase in 1997. Thereafter, the mean duration of these CCX rarely fell below 50 days and instead achieved new records with durations of close to 200 days. MHW-LOX and the triple compound events have also increased in duration over the hindcast period, averaging close to 50 days per event towards 2020.

The starkest changes in the CCX properties occurred with the maximum intensity index (Figure 5d). In the 1960s and 1970s, it hovered around 2 for all compound extremes. But then, as the intensity of OAX began to increase rapidly due to strong trends in ocean acidification (Ma et al., 2023), the maximum intensities of all OAX-related CCX began to increase rapidly as well, reaching a nearly 10-fold increase by 2020. This rapid increase can be attributed to the increase in OAX intensity. The exception is MHW-LOX, which experienced "only" a doubling in their maximum intensity.

In summary, column compound extremes used to be relatively rare, but have become much more prevalent and frequent over the last few decades and, in particular, have become much more intense. This is best illustrated for the triple column compound extremes that have expanded 39-fold, now last 3-times longer, and have become 6-times more intense since the early 1960s. This strong increase is driven to a substantial degree by the increase in the intensity of the OAX. 2.3 % of the volume of the global upper ocean is now under conditions of triple compound extremes, corresponding to a volume of $2\,300\,000\,\mathrm{km}^3$. This is much greater than, for example, the volume of the ocean that is considered 'dead' as a consequence of coastal eutrophication (Diaz & Rosenberg, 2008). Thus, while many studies have already shown the increasing frequency, duration, and intensities of surface extremes, especially those of MHW, our work now shows that this leads to severe reductions in habitable space below the surface, restricting the ability of organisms to cope with, for example, surface MHW by migrating to deeper depths. These analyses also show how important it is to better understand the impact of compound extremes on marine organisms, as these compound extremes are becoming more common (Hauri et al., 2024).

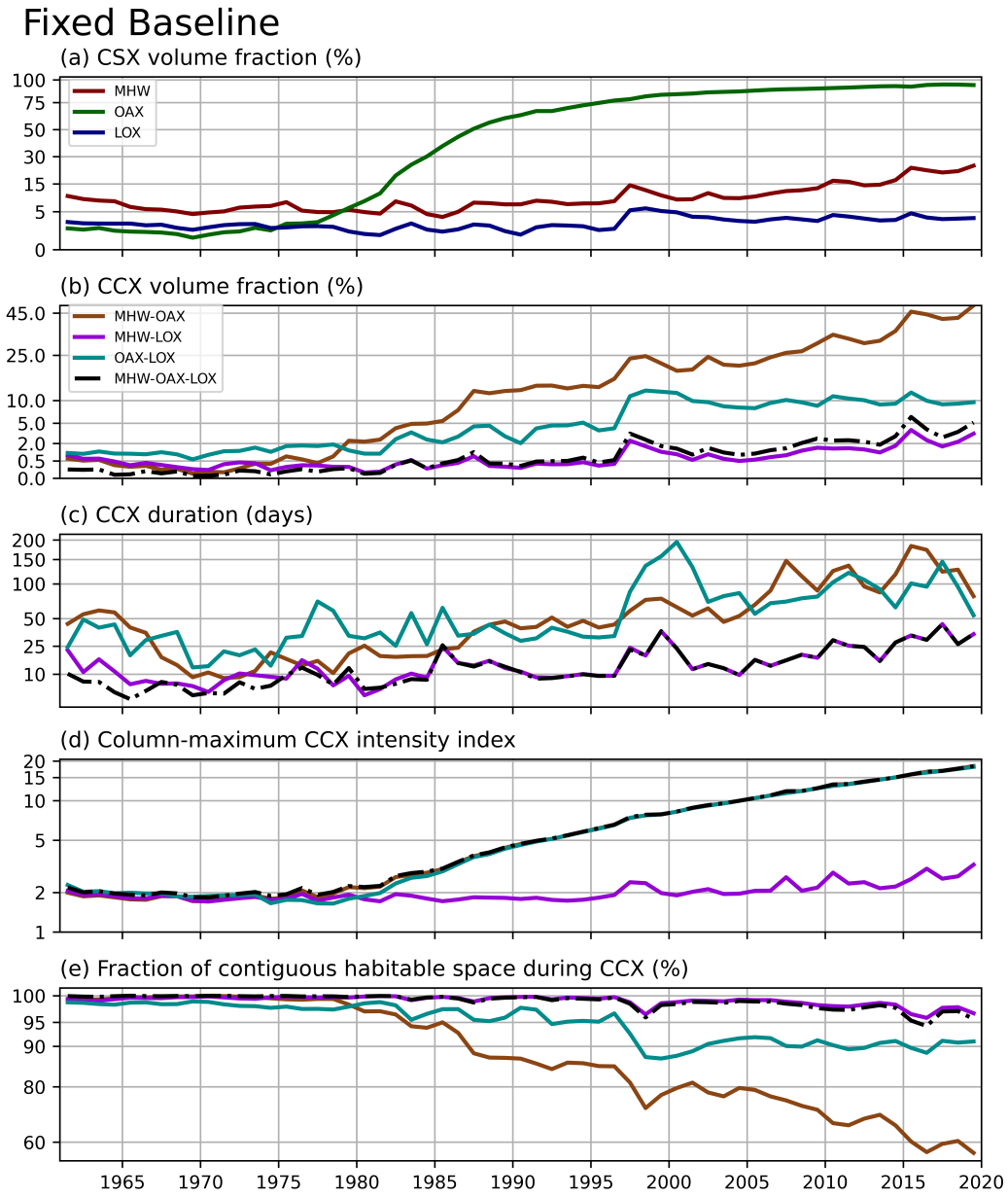

Figure 5. Temporal evolution of model simulated column extremes over the past 60 years on a fixed baseline. Shown are the timeseries of (a) annual mean global volume fraction of the three single column extremes (CSX), (b) annual mean global volume fraction of column compound extremes (CCX) of the four different types, (c) mean CCX duration, and (d) annual column-maximum CCX intensity index.

Next, we would like to investigate the processes behind these events, and also understand what causes, e.g., also the strong year-to-year variations in the trends. We also would like to characterize the events more specifically with regard to where they occur and what properties they have. To this effect, we change our perspective to a moving baseline, which removes the long-term trend. We do this without the intention of understating the increasing severity of marine extremes under climate change.

4.2 Temporal Variability of Column-Compound Extremes

By removing the underlying climate trend through the use of a moving baseline, the strong year-to-year variability of the column-compound extremes becomes clearer (Figure 6). In particular, local peaks in the global volume fraction, duration, and intensities of CCX coincide with strong ENSO events of high Oceanic Niño index (ONI). Most visible are the alignments of the peaks during moderate and strong ENSO events in 1972-1973, 1982-1985, 1997-1998, 2009-2011, and 2015-2016. The global mean volume fractions of CCX are strongly correlated with positive ONI (Pearson $R = 0.50$ to 0.68), but less so with negative ONI (Pearson $R = -0.06$ to -0.27). The negative R indicates an increase in volume fraction with more negative ONI. We examine ENSO as a driver of CCX on a regional scale in Section 4.5.

OAX-LOX events affect the water column more than any other type of CCX. On average, they have the highest mean volume fraction of 1.2 % (1 208 000 km^3), reaching up to 4.7 % (4 732 000 km^3) during the strong consecutive El Niño/La Niña events of 1997-1998. They also last the longest, having a duration of about 18 days on average but exceeding 40 days during some periods. Due to their large volume, they also contract the habitable space the most out of all the CCX types. The maximum intensity of OAX-LOX at about 2.5 is among the highest of double CCX. The second most extensive type of CCX is MHW-OAX, which typically occupies about 0.9 % of the global volume (906 000 km^3), and lasts 11 days, on average. It trails behind OAX-LOX in intensity, with a maximum intensity index typically higher than 2. Although some peaks may be seen coinciding with major ENSO events, their association with ENSO is weaker than that of OAX-LOX. Finally, there is a relatively smaller mean volume of MHW-LOX and triple CCX (MHW-OAX-LOX), of 0.16 % (161 000 km^3) and 0.11 % (111 000 km^3) respectively. These two CCX types have the same interannual variability, suggesting that many MHW-LOX events are also triple compound events.

4.3 Spatiotemporal Distribution of Column-Compound Extremes

The four different types of CCX have rather different global distributions in terms of annual extreme days (Figure 7a,c,e,g), and in terms of the co-occurrence propensity (Figure 7b,d,f,h) (see also Table 2). MHW-OAX occur globally, but most frequently in the subtropics and the high-latitude Southern Ocean, where between 5 to more than 25 days per year are characterised as MHW-OAX events (Figure 7a). In contrast, the number of MHW-OAX days in the equatorial regions is low, typically less than 10 days. The co-occurrence propensity (later referred to as just propensity) helps to explain these distributions. For example, the strongly negative propensity of MHW-OAX events in the eastern tropical Pacific explains well why the number of CCX days in this region is so low (Figure 7b). This negative propensity means that whenever there is, for example, a heatwave in this region, the likelihood that this region also has an OAX is substantially lower than by chance. This is a result of the fact that most MHW in the eastern tropical Pacific are associated with El Niño, which tend to push the thermocline and therefore also the waters with high $[H^+]$ down, thereby suppressing the formation of subsurface OAX (Burger et al., 2022). Similarly, the negative propensities in the boundary upwelling regions are the result of surface OAX events that are typically driven by strong upwelling events (Desmet et al., 2022), which tend to cool the surface ocean and therefore suppress the formation of MHW.

The OAX-LOX events have nearly the opposite spatial pattern to that of the MHW-OAX events (Figures 7c,d). The OAX-LOX events occur primarily in the tropics, in the Eastern Boundary Upwelling Systems (EBUS), and the north subpolar Pacific, typically more than 15 days per year under CCX conditions. On the contrary, OAX-LOX events are entirely absent in the North Atlantic and the ocean south of about 30°S. This absence is a consequence of the high level of oxygenation in these regions with $[O_2]$ stay-

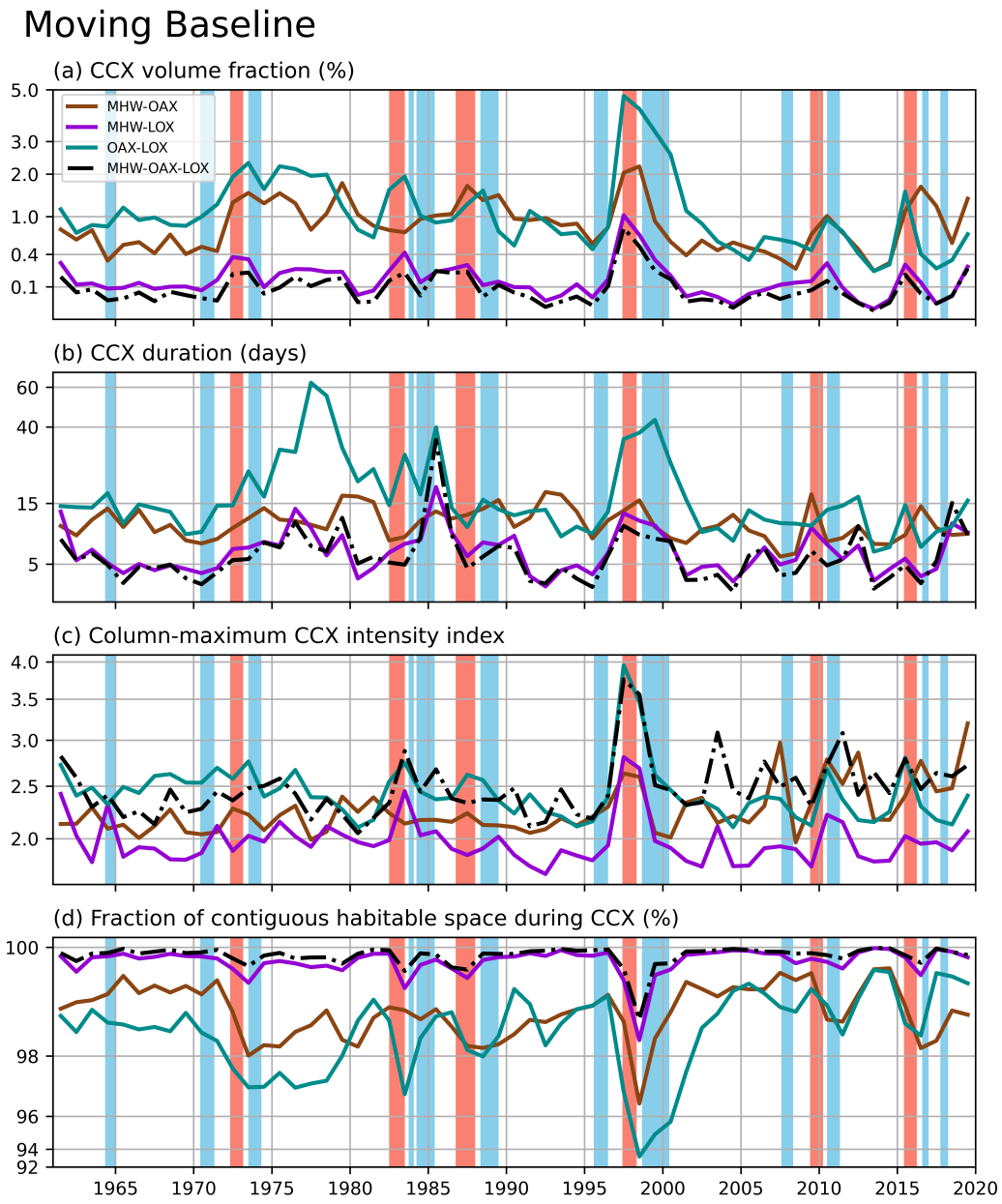

Figure 6. As Figure 5, but for a moving baseline, i.e., when the trends are removed using a quadratic fit. Strong El Niño events (ONI $\geq 1.5\,^{\circ}$C) are shaded in red, and strong La Niña events (ONI ≤ -1.0 are shaded in blue.)

ing generally above the 150 μM threshold. This contrasts with the low-latitude regions, many of which are characterised as oxygen-deficient zones (ODZs) (Paulmier & Ruiz-Pino, 2009), fostering the presence of LOX (Köhn et al., 2022). The high prevalence of the OAX-LOX events in the low latitudes can be understood by their very positive propensity, which means that when there is a LOX, there is a very high chance that there is also an OAX. This can be understood from the fact that OAX and LOX tend to be generated by the same processes, such as remineralisation, upwelling, or thermocline heav-

ing (Gruber et al., 2021), substantially increasing the likelihood that the two extremes occur together.

Compared to these first two CCX types, MHW-LOX and the triple compound occur substantially less frequently (Figure 7e,g). The spatial pattern is similar to that of the OAX-LOX events with a low-latitude focus, suggesting that the absence of LOX in the high latitudes due to the oxygen threshold is also an important determinant for the triple compound events. However, the propensity plots exhibit a clear difference (Figures 7f,h), with most areas having substantially lower propensity than those exhibited by the OAX-LOX events, and some regions even having a negative propensity. The reasons behind this distribution are complex and will be discussed later in this study.

Thus, we can identify two general patterns of the occurrence and propensity of CCX. A more global and high-latitude pattern for MHW-OAX events and a more low-latitude/tropical pattern for the other three CCX types due to the oxygen concentration threshold. This allows us to focus on only two of the four types in the following discussion of the full sets of CCX metrics, i.e. MHW-OAX events (Figure 8) and MHW-OAX-LOX triple compounds (Figure 9). Figures for the other two CCX types, i.e., OAX-LOX and and MHW-LOX, can be found in Figures S17-S18.

MHW-OAX events in the subtropics and Antarctic zone last the longest (more than 20 days) (Figure 8a). In these regions, we also see a maximum intensity index of 2 to 4 (Figure 8b), which means that the intensity of the combined events is approximately 2 to 4 times the intensity of the threshold for a single event. This shows that where MHW-OAX occur most frequently, they are also long and intense. Likewise, in tropical regions where the number of CCX days is small and where the CCX events are short (Figure 8a,c) they are also relatively weaker, between 1 and 3 in the maximum intensity index. This is also the region of very low propensity (Figure 8d). But while the CCX events in the tropics are less frequent, shorter, and less intense, they still contract the habitable space, between 25 % to 75 % of the column (Figure 8e). In some areas, the remaining contiguous habitable space is less than 25 % (Figure 8f).

The spatial distribution of the triple compound events (MHW-OAX-LOX) can be understood in conjunction with that of the OAX-LOX. OAX-LOX events are unique from the other CCX types due to their high number of days per year (Figure 7c) and positive propensity everywhere they occur (Figure 7d). This means that when either OAX or LOX occurs, the other almost always occurs together with it. Thus, the triple compound occurs when an MHW is induced in the same column. We see this more frequently in the tropics and the Bering Sea, up to 21 days a year in some areas (Figure 9c). When triple CCX occur, they typically have moderate maximum intensity indices of 2 to 3, but can exceed 4 in the central tropical Pacific (Figure 9b). In the equatorial regions, they typically last up to 10 days (Figure 9c). However, their durations are more than double in the Bering Sea and along the boundaries of the subtropical gyres. The triple compound events contract the habitable space by far the most (Figure 9f). During such events, less than 50 % remains habitable, with some regions going to 0% in some areas.

4.4 Vertical Structure and Clustering of CCX

The k-means clustering for the MHW-OAX events according to the vertical distribution of extreme conditions results in four clusters (see Figure 10 left column) with distinct properties and spatial distributions. This clear separation confirms our choice of clustering only on the basis of the vertical distribution of the extremes. Cluster 2 (24%) occupies much of the subtropical gyres, while clusters 3 (14 %) and 4 (5 %) occur in the Subantarctic zone of the Antarctic Circumpolar Current (ACC) and in the Antarctic zone, respectively. Cluster 1 occurs along the borders of the other clusters, accounting for nearly 60 % of the total area of all MHW-OAX events. However, it also has the shortest average duration, the lowest average days per year, and the lowest maximum intensity in-

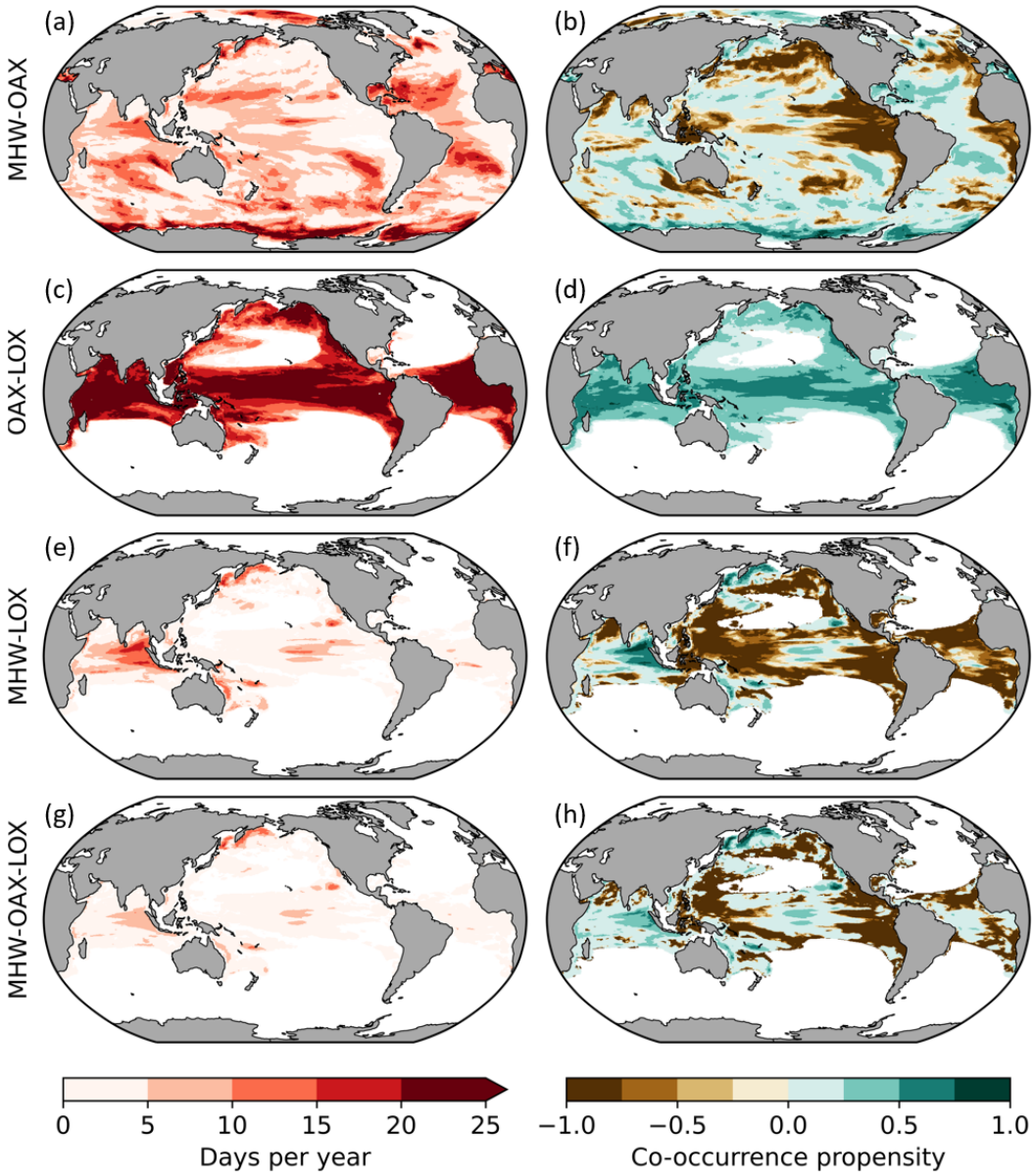

Figure 7. Spatial distribution of CCX illustrated by: CCX days per year (left column) and mean co-occurrence propensity (CP) of CCX (right column). A positive CP indicates two column-single extremes occurring in the same column more frequently than by random occurrence. Conversely, a negative CP indicates a lower frequency than random occurrence. (Section 3.3). Each row corresponds to one CCX type, i.e. (a,b): MHW-OAX, (c,d): OAX-LOX, (e,f): MHW-LOX, (g,h): MHW-OAX-LOX.

dex. In contrast, cluster 4 is the highest in these metrics, with the other two clusters in between. In terms of vertical fraction, the four clusters are similar, ranging between 41% and 46%.

We discuss these clusters in turn, using their characteristics as an indication of the likely processes driving them. Since increases in temperature during MHW directly lead to an increase in $[H^+]$ through shifts in the carbonate chemistry equilibrium, some of the

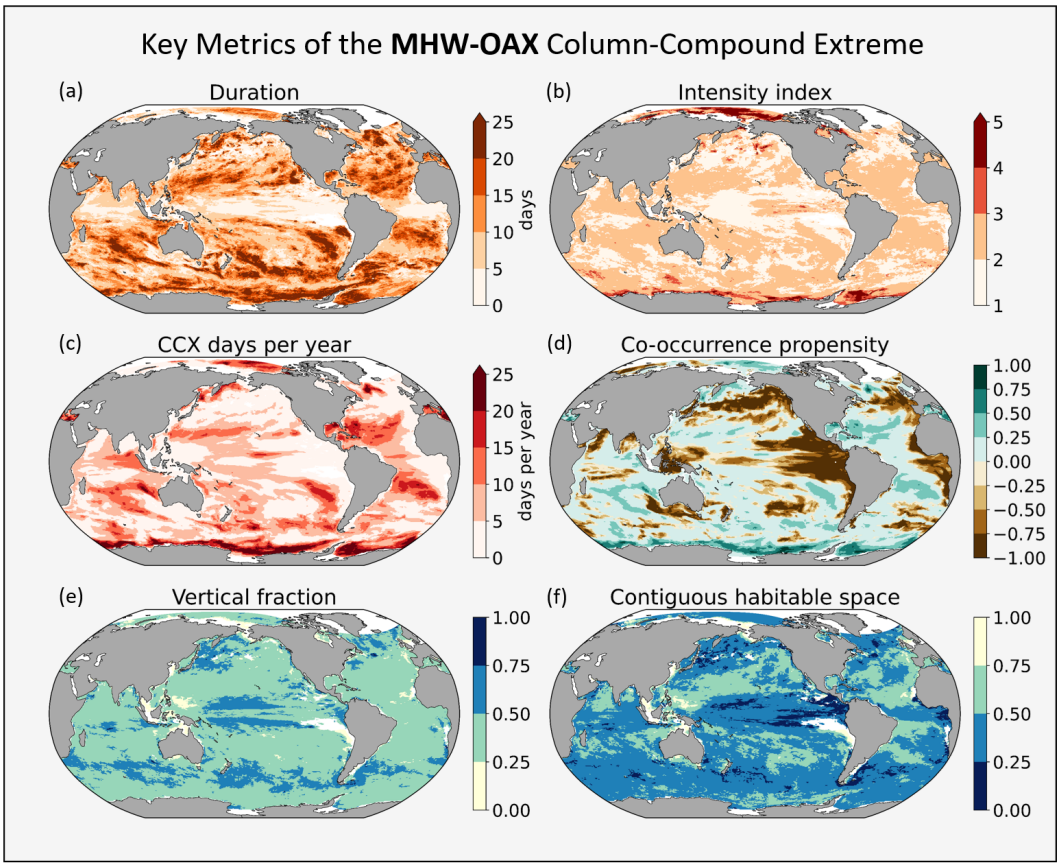

Figure 8. Key metrics of MHW-OAX events in the global ocean. (a) Mean duration, (b) mean annual maximum intensity index, (c) mean annual CCX days, (d) mean co-occurrence propensity, (e) mean fraction of water column occupied by extremes, and (f) mean fraction of contiguous habitable space in the vertical column. (c) and (d) are the same plots as Figure 7(a) and 7(b).

OAX must be driven by the MHW (Burger et al., 2022; Burger & Frölicher, 2023). As the isochemical sensitivity of $[H^+]$ is well known, we can compute the fractional contribution of the temperature changes to the changes in $[H^+]$ (Text S4) (Orr & Epitalon, 2015). We do not have sufficient information stored during the simulation to determine all the processes that drive the changes in DIC and Alk underlying the non-thermal changes in $[H^+]$ (Burger & Frölicher, 2023), but we use anomalies in the export and sinking of particulate organic carbon (POC) and a logistic regression (Mahlstein et al., 2012; Filho et al., 2013; Le Grix et al., 2023) to infer the potential contribution of changes in the biological pump to the OAX (Text S5).

Cluster 1 is characterised by the bimodal depth distribution of the MHW and OAX signals, with a surface signal similar to cluster 2, and a weaker maximum in the subsurface reminiscent of the signals in clusters 3 and 4. Since the violin plots reflect the sum of extreme signals over the hindcast period, these modes do not necessarily occur at the same time. On average over all grid columns contributing to cluster 1, the warming associated with MHW can account for nearly 80% of the OAX (Figure S21), suggesting that it is primarily the MHW that drives this CCX cluster. We did not find a strong relationship between the events in Cluster 1 and POC export (Table S1), leaving advection and mixing processes as the most likely processes driving the remaining 20% of the

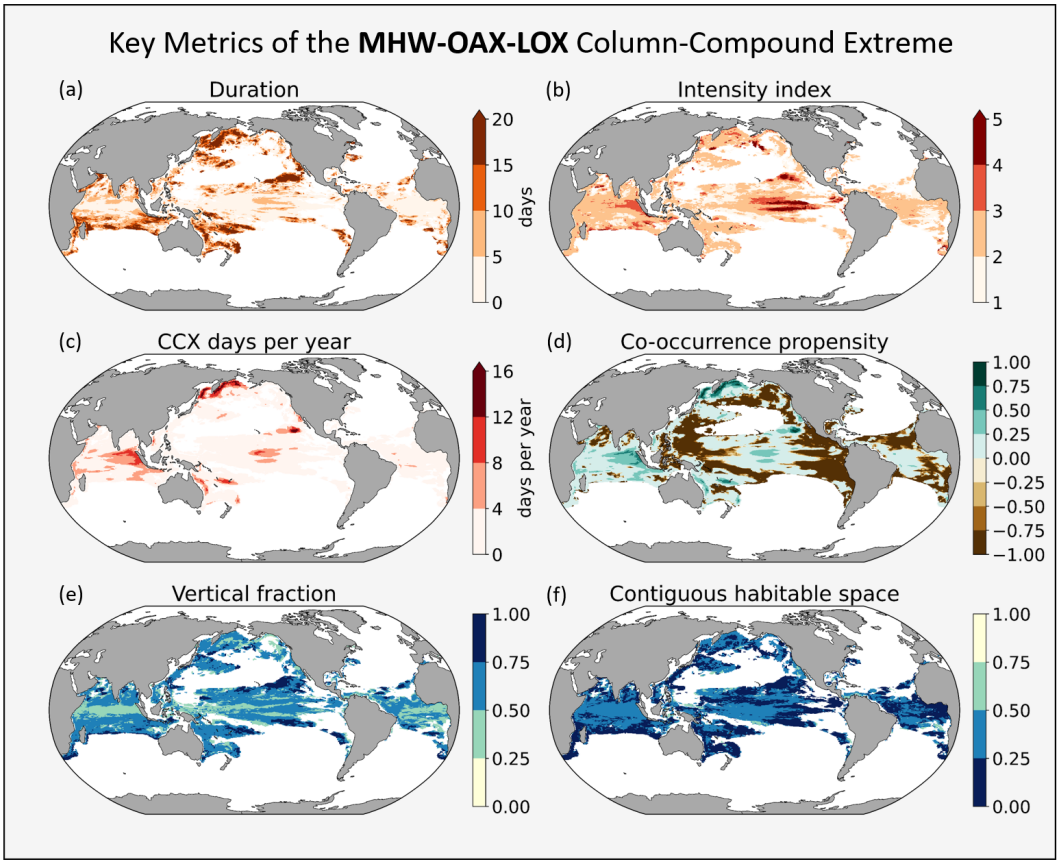

Figure 9. As Figure 8, but for triple compound events. (c) and (d) are the same plots as Figure 7(g) and 7(h).

OAX signal in this cluster. Potential mechanisms include the advection of surface waters with MHW or OAX characteristics from adjacent regions (Holbrook et al., 2019; Sen Gupta et al., 2020; Elzahaby et al., 2021), possibly combined with downwelling Kelvin and Rossby waves that can propagate, maintain, and deepen the extreme signals (Holbrook et al., 2019; Zhang et al., 2021; Maulida et al., 2022; Qi et al., 2022).

Cluster 2 has a pure surface intensified signal, with MHW and OAX co-occurring from the surface down to 100 m. More than 100 % of the change in $[H^+]$ can be explained by the warming (Figure S21), suggesting that a surface ocean driven MHW is the key process driving this type of CCX. Compound surface MHW and OAX have previously been detected by Burger et al. (2022) in similar regions of the tropics and subtropics, and our analysis shows that these events tend to extend further below the surface.

MHW-OAX cluster 3 is the opposite of cluster 2, with a strong subsurface intensified signal. In cluster 3, MHW occur beneath the surface between 50 −300 m, and OAX occur in the lower half of the water column below 100 m. The spread across the water column causes this cluster to have the highest vertical fraction of 46 %. Up to 60 % of the change in $[H^+]$ in co-occurring OAX can be attributed to the increase in temperature (Figure S21). In addition, enhanced export and remineralisation appears to be driving part of the OAX signal, as indicated by the positive correlation between MHW-OAX events and increased POC export (Table S1). Another contribution might stem from anomalous advection and mixing. In fact, the regions occupied by this cluster, such as the Scotia Sea, Drake Passage, and Macquarie Ridge, stand out as regions with enhanced di-

apycncal mixing (Ledwell et al., 2011). Strong wind-driven currents and rough bathymetry have been shown to drive mixing in the upper water column (Pellichero et al., 2017; Vogt et al., 2022) and may be drivers of intrusions of MHW in the subsurface. Local parcels of water carrying the MHW signal may be disconnected from the surface and later reconnected by mixing and heating the surface. An example from the hindcast is shown in Figure S23.

Cluster 4 events occur along the Antarctic continent, with co-located MHW and OAX occurring largely beneath the surface between $100-300$ m. Here, MHW-OAX events have the highest frequency of 21 days per year, the longest mean duration of 19 days, and the highest maximum intensity index of 3.3. We suggest the upwelling of Circumpolar Deep Water (CDW) as the primary mechanism for driving the MHW-OAX events of this cluster, since CDW is warmer and more acidic than the upper waters in the Antarctic zone (Dinniman et al., 2011; Pellichero et al., 2017; Wang et al., 2023). Such upward intrusions of the CDW may be driven by strengthened zonal westerlies (Morrison et al., 2015; Wilson et al., 2019; Ramadhan et al., 2022) or low sea-ice extent (Ramadhan et al., 2022). The effect of upwelling on OAX may be enhanced by greater export and remineralisation of POC, which we identify through logistic regressions (Table S1). An example of such an event is shown in a time-depth diagram (Figure S24).

OAX-LOX events are separated into three clusters (see Figure10 middle column), where each cluster may be found in the same areas of each ocean basin. Cluster 1 roughly corresponds to the eastern tropics and the EBUS regions, with OAX and LOX located together between 50 m and 200 m deep. Cluster 2 events are located deeper in the water column, between 100 m and 300 m, and are located along the boundaries of cluster 1, reaching the western side of the basins. Cluster 3 is located along the boundaries of the subtropical gyres, where the deepest events are found below 100 m. The three clusters are likely driven by the same processes, with the specifics determined by the background state. This is due to the very strong negative correlation between $[O_2]$ and $[H^+]$ in the ocean interior as a result of the biological pump (Sarmiento & Gruber, 2006; Paulmier et al., 2011; Gobler & Baumann, 2016). This negative correlation means that any lateral or vertical displacement of water masses has the potential to create a combined OAX and LOX event (Gruber et al., 2021). The specific occurrence of this type of CCX is modulated by our use of the $150\,\mu$M threshold for $[O_2]$. This threshold is closest to the surface in the EBUS, the eastern tropical Pacific, the subarctic Pacific, and the Indian Ocean, deeper in the western tropics, and is not reached within the upper 300 m of the subtropical gyres or the high latitudes (Gilly et al., 2013). Thus, the three clusters track this depth distribution. Our hypothesis of anomalous displacement driving OAX-LOX events is supported by strongly positive logistic regressions between OAX-LOX occurrences and the shoaling of the thermocline depth (Fiedler, 2010) (Table S1). The respective odds ratios of each cluster indicate an increased probability of CCX by 2.10 , 1.77 , and 1.43 times for every 10 m of thermocline shoaling. The OAX signal may further be enhanced by the consequence of increased biological productivity (inferred from regressions on POC export anomalies) driving additional remineralisation.

The clustering separates the MHW-LOX events into 4 clusters (Figure 10 right column). Very similar clusters are obtained for the triple compound MHW-OAX-LOX events (Figure 10 bottom row), which is the result of the high spatial correlation between the MHW-LOX and the triple compound extremes in all characteristics (see Figure 7). As a consequence, we focus on the clusters of the triple compound extremes.

MHW-OAX-LOX cluster 5 (MHW-LOX cluster 4) is found in the central equatorial Pacific. It is the most intense of all CCX clusters with a maximum intensity index of 3.6 , but it has a relatively short duration of 9 days and occurs only 4 days per year on average. The triple compound cluster with the longest duration of 32 days and occurring 10 days per year is cluster 4 (MHW-LOX cluster 2), found in the Bering Sea. In the eastern tropical Indian ocean, we find MHW-OAX-LOX cluster 3 (MHW-LOX clus-

ter 2) occurring 7 days per year. Finally, MHW-OAX-LOX clusters 1 and 2 (MHW-LOX clusters 1 and 3) occupy the largest area fraction of 86.8 %, and border the other clusters in the tropics and North Pacific.

In MHW-OAX-LOX clusters 1 and 2, surface intensified extreme signals in temperature are clearly separated from the depth intensified signals in acidity and oxygen, as vertical entrainment and/or mixing is restricted across the thermocline. We suspect that the anomalous heating of the surface stratifies the surface layer and confines the MHW signal to the top 100 −150 m of the column. Meanwhile, OAX and LOX are intensified below the MHW. Changes in biological production and export cannot be the primary driver of these subsurface changes, since we find in cluster 2 a significant odds ratio of 0.64 , which means that biological production, export, and remineralisation are reduced during these events, thus adding less $[H^+]$ to the water column and removing less $[O_2]$. In cluster 1 the correlation with POC export is relatively weaker but still negative, and thus also not explaining the co-occurrence. Instead, we propose that these subsurface extremes are a consequence of two related mechanisms. Increased stratification leads to decreased subsurface ventilation and therefore anomalously high DIC and low $[O_2]$. Increased stratification also drives an increase in the efficiency of the biological pump (Sarmiento & Gruber, 2006), further strengthening the gradient and causing the subsurface concentrations of $[H^+]$ to increase and that of $[O_2]$ to decrease.

In contrast, certain conditions allow heat to be transferred below the thermocline, leading to distinctive CCX depth profiles. The MHW-OAX-LOX Cluster 5 in the central tropical Pacific is one such example, where MHW is intensified at the surface (0 −50 m), and at depth (150 −300 m). Meanwhile, OAX and LOX occupy the gap between 50 −150 m. During El Niño periods, strong anomalous surface heating occurs in the eastern tropical Pacific, deepening the thermocline and inducing MHW throughout the water column (Fiedler & Lavín, 2017). On the western side of the Pacific, the thermocline shoals, causing subsurface OAX and LOX to extend into the central tropical Pacific (Xu et al., 2017; Leung, Thompson, et al., 2019). Thus, the triple compound occurs when all three stressors occur in the same column, albeit at different vertical locations. When the surface heating tapers towards the end of El Niño, the MHW signal at the bottom of the column remains below the thermocline and is cut off from surface ventilation, leading to the characteristic depth profile seen in Figure 10. This subsurface MHW signal persists even into the succeeding La Niña event, where the shoaling thermocline in the east leads to intensified OAX and LOX above the MHW. This process is illustrated through a video (Movie S1). The logistic regression supports the described process occurring during La Niña with a strong correlation between shoaled thermocline depth, decreased stratification, and increased biological productivity (Table S1). Since the violin plots are a sum of the extreme signals across the hindcast period, the MHW signals at the surface and subsurface may also occur separately with OAX and LOX as triple compound events.

In the eastern tropical Indian ocean and the Bering Sea, corresponding to MHW-OAX-LOX clusters 3 and 4, an unusual combination of all three stressors co-occur in the subsurface below 100 m with little to no concurrent surface-MHW expression. One possible cause of MHW-OAX-LOX in cluster 4 is preceding warm atmospheric conditions that cause sea ice retreat and surface MHW (Carvalho et al., 2021). Another source of warm waters in the specific case of 2018 could be the Pacific Blob event in 2014-2016, which saw intense MHW covering the northeastern Pacific, mixing into the subsurface and persisting below the mixed layer, then advecting northward. Subsequently, lower sea-ice cover in the winter led to weakened stratification and allowed warm water to penetrate the subsurface (Stabeno & Bell, 2019; Basyuk & Zuenko, 2020; Scannell et al., 2020). OAX and LOX are then partially the result of anomalous temperatures driving an increase $[H^+]$ and a decrease in oxygen solubility. This is seen by the change in temperature accounting for 22 % of the change in $[H^+]$ (Figure S22). Later, the increased stratification associated with this cluster (Table S1) hindered the ventilation of the subsur-

face, maintaining the triple compound at depth. An example from this cluster is illustrated in a time-depth diagram (Figure S25). Although there are no existing works on subsurface extreme events in the Bering Sea, the subsurface compound extremes found by Hauri et al. (2024) in the Gulf of Alaska reflect the timing and processes associated with this cluster in the Bering Sea. Carvalho et al. (2021) also found an increase in the number of surface MHW in the Bering Sea in the time periods leading up to those of cluster 4 (Figure S20). In cluster 3, the largest event occurred in 1997, corresponding to the largest event of cluster 5, and a strong El Niño event (S20). This suggests an ENSO teleconnection in the Indian Ocean leading to subsurface MHW-OAX-LOX. In these two clusters, few MHW studies have been conducted and even less so on subsurface MHW, OAX, and LOX. As research in this space has been gradually gaining attention, we expect to better understand the mechanisms behind these subsurface triple compound events in the future.

4.5 Enhancement and Suppression of CCX during ENSO Events

Further insights into the potential drivers of CCX can be deduced from when the CCX occur. We have already seen that, on the global scale, most CCX tend to correlate positively with ENSO (Figure 6). However, we also identified more complex responses with enhanced occurrences during both strong El Niños and strong La Niñas. Therefore, it is worth examining this connection, looking at the cluster-level changes in CCX days during El Niño (Figure 11a,c,e,g) and La Niña (Figure 11b,d,f,h) events. Correlating ENSO with extreme events on a global scale is not a trivial task, as remote teleconnections with varying lag times are involved. By performing this analysis on an annual timescale, we aim to capture all ENSO effects within a calendar year. Certainly, more sophisticated methods could be applied (Holbrook et al., 2019; Deser et al., 2024), but here we opt for the simplest. The calculation of the change in CCX days with ENSO is described in the Supporting Information Text S6, and the numbers used in Figure 11 are listed in Table S2.

During both phases of ENSO, the number of extreme days per year generally increases throughout the global ocean for all types of CCX (Figure 11). Exceptions are found in the Antarctic sector during MHW-OAX events and in the Bering Sea during MHW-OAX-LOX events. OAX-LOX events stand out as having the strongest and most distinct ENSO associations (Figure 11c-d). In the tropical Pacific, El Niño and La Niña phases have distinctly different pattern. During El Niño, OAX-LOX events are enhanced in the west by up to 16 days a year (cluster 2), representing a 69 % increase over the mean annual CCX days in that cluster. Conversely during La Niña, the eastern tropical Pacific (cluster 1) experiences an enhancement of OAX-LOX of a similar magnitude and a weaker suppression in the west of 7 days per year (cluster 2). These events can be strongly linked to ENSO dynamics with the shoaling and deepening of the thermocline, as highlighted in the previous section. The effects of ENSO on OAX-LOX in other ocean basins are also strong with a similar east-west polarity. They are typically facilitated by atmospheric teleconnections (Roy & Reason, 2001) and ocean currents (Susanto et al., 2001; Feng et al., 2018), through mechanisms such as thermocline and upwelling modulations.

The changes in annual MHW-OAX days (Figure 11a-b) are similar in magnitude and sign between both phases of ENSO, with the strongest response in the subtropics (cluster 2). Here, an increase of up to 6 days per year is observed during ENSO events, representing a 50 % increase over the mean. Close to the Antarctic continent (cluster 4), the response is relatively muted with a small decrease of 2-4 days a year during ENSO years. Within this cluster, smaller regions may exhibit different responses to ENSO, alluded to by Holbrook et al. (2019) and Sallée et al. (2010) who linked surface MHW and mixed layer depth changes to various climate modes such as ENSO, the Southern Annular Mode (SAM), and the Interdecadal Pacific Oscillation (IPO). Surface wind stress variability during SAM leads to changes in the depth of the thermocline and is a pos-

sible mechanism for the subsurface CCX observed in this cluster. Although we have performed logistic regressions of CCX with local wind stress anomalies (Table S1), we did not find a significant correlation of CCX in the Southern Ocean with changes in wind. This is likely because the subsurface effects of upwelling and thermocline changes may be driven by non-local changes in wind stress (Tamsitt et al., 2017).

With MHW-LOX and MHW-OAX-LOX, there are few spatial differences between the positive and negative phases of ENSO (Figure 11e-h). The central tropical Pacific stands out with the strongest response to ENSO, with an increase of 14 days during El Niño and 9 days during La Ni na during MHW-LOX, and 7 and 5 days, respectively, for MHW-OAX-LOX. These increases represent more than a doubling of the mean annual CCX days in each cluster. This area corresponds to cluster 5 of the triple compound event, which has distinctive peaks in volume fraction in the El Niño years of 1997 and 2016 (Figure S20). Both the surface MHW from the east and the subsurface OAX and LOX from the west trace their driver to El Niño, thus having a single common driver, although operating through different processes on the different sides of the tropical Pacific.

The lack of a strong ENSO response in MHW-related CCX in the eastern tropical Pacific is different from the surface MHW correlations of Holbrook et al. (2019); Sen Gupta et al. (2020), where there is typically a strong response in the eastern equatorial Pacific. This was also reflected in their co-occurrence propensities (Figure 7. MHW induced on the surface during El Niño strongly stratify the surface, suppressing the upwelling of deep waters, pushing the thermocline down and therefore reducing the occurrence of OAX and LOX. Although some surface MHW induce co-located OAX due to the temperature effect on $[H^+]$, the associated changes in $[H^+]$ tend to be smaller than those induced by the changes in upwelling, such that the co-occurrence propensity of MHW and OAX is very low. As a consequence, ENSO is not a strong driver of CCX in the Eastern tropical Pacific, that is, in the region where it has the largest impact, even though ENSO drives substantial variability elsewhere in the global ocean.

5 Discussion

Most studies on marine extremes have so far focused on surface MHW, limiting their analyses to the drivers and impacts occurring in the surface layer. With the CCX detected in this study, there is a need to infer surface and subsurface drivers. Furthermore, CCX in this study with surface expressions extend at least 50 m into the subsurface, prompting an investigation of surface stratification and the mixed layer. Similarly, the associated impacts of CCX are relevant not only to organisms residing at a certain depth, but also to those who inhabit the entire upper ocean water column. These migrating organisms are affected to a greater extent as CCX shrink and divide their habitable space.

5.1 Climatic Drivers of Column-Compound Extreme Events

The most significant CCX clusters identified in Section 4.4 are summarised in Figure 12, with their corresponding metrics and vertical structure. With the analysis, we have also repeatedly identified ENSO events as the main driver of a large proportion of CCX. This is due to the large area of the Pacific Ocean that is typically affected by ENSO and the atmospheric and oceanic connections it has with other ocean basins. However, the mechanisms through which ENSO drives CCX vary by region. Furthermore, ENSO events can drive CCX through multiple mechanisms.

Some of these ENSO-driven CCX have been identified as being spatially co-occurring, where their constituent single extremes co-occur in the same grid cells and tend to be driven by similar mechanisms. The most prominent example is OAX-LOX, which occurs primarily in the subsurface. OAX-LOX clusters 1 and 2 exhibit this effect at different depths, depending on the location of the thermocline. La Niña events associated

with an increase in surface winds drive an anomalous upwelling of low-pH and low-oxygen waters in the California and Humboldt current systems, leading to events in the OAX-LOX 1 cluster. Furthermore, the increased biological productivity induced by the upwelled waters can further deplete oxygen through remineralisation and enrich the water with carbon, driving OAX. The depth of OAX and LOX during OAX-LOX events in the EBUS and east tropics cluster lies between $50-200$ m, which is consistent with the typical coastal and offshore upwelling source waters of $150-280$ m (Chhak & Di Lorenzo, 2007; Frischknecht et al., 2018; Bograd et al., 2015), and sits beneath the mean mixed layer depth (Ando & McPhaden, 1997; Fiedler & Talley, 2006). Furthermore, the shoaling of the thermocline in the east tropics intensifies OAX and LOX in the subsurface. The co-occurrence propensity and vertical location of these events correspond roughly with the locations of low oxygen zones or shadow zones (Luyten et al., 1983; Paulmier & Ruiz-Pino, 2009), which are often associated with low pH (Paulmier et al., 2011). In the western tropical Pacific corresponding to OAX-LOX cluster 2, El Niño events lead to the shoaling of the thermocline, bringing low pH and low oxygen waters closer to the surface, with mean depths corresponding to the mean mixed layer depth (Ando & McPhaden, 1997; Fiedler & Talley, 2006). In general, these events are deeper in the column than their eastern counterparts due to the deeper mixed layer depths in the western tropical Pacific. These events have the highest days per year among the identified clusters, increasing the most during ENSO events. The association of OAX-LOX events with a shallower thermocline and increased biological productivity has been shown in Section 4.4 through the odds ratio values of logistic regressions.

Another example of spatially co-occurring CCX driven by ENSO is MHW-OAX cluster 2, predominantly in the subtropics. Within this cluster, we see a positive association with both phases of ENSO (Figure 11. ENSO-driven temperature anomalies lead to MHW (Holbrook et al., 2019), which then induces OAX through shifts in the carbonate chemistry equilibrium (Zeebe & Wolf-Gladrow, 2001; Burger et al., 2022). The areas where MHW-OAX 2 occur tend to be areas without a tendency for deep water upwelling or thermocline shifts. The contribution of temperature to increases in $[H^+]$ was shown in Section 4.4 by computing the fraction contribution of temperature anomalies. For all MHW-OAX clusters, the temperature contribution is high (>0.6), but the highest is seen in MHW-OAX-2 with a value of 1.38

ENSO events can also drive CCX through multiple mechanisms, as seen in MHW-OAX-LOX cluster 5. MHW is induced throughout the column by strong surface heating during El Niño in the eastern tropical Pacific. Meanwhile, El Niño also drives the shoaling of the thermocline in the western tropical Pacific, inducing OAX and LOX in the subsurface. A deep MHW also persists in the subsurface even after being disconnected from the surface MHW. The resulting CCX is one that occupies the entire water column, driven by El Niño through different mechanisms. The MHW-OAX-LOX cluster 4 is another peculiar example, of which one occurrence in 2018 has been linked an El Niño event in 2014-2016 (Basyuk & Zuenko, 2020). Lateral advection of a warm water mass, enhanced southerly winds, and lower sea ice cover could be factors that lead to surface MHW in the Bering Sea. Anomalously low stratification then allows heat to be transmitted to the subsurface, possibly inducing OAX and LOX. Since our ENSO analysis does not account for lag times, it is difficult to link this event to ENSO. CCX in this cluster may also be driven by local processes and other modes of variability, such as the Pacific Decadal Oscillation (PDO). The mechanisms behind events in these two clusters involve vertical and lateral transfer of heat and/or water, occurring over timescales of months. Thus, it is a more complex driver attribution than can be achieved through the correlations employed in this study.

The CCX in the Southern Ocean (MHW-OAX clusters 3 and 4) could be driven by various climate modes. Within these clusters, strong sub-cluster enhancements and suppression have been found during ENSO events. Due to the regionally varying ENSO

response within the clusters, the cluster-mean change in days per year due to ENSO is rather muted. These CCX can be inferred to be driven by a combination of surface heating, strong winds causing diapycnal mixing (Ledwell et al., 2011; Tamsitt et al., 2017), anomalous sea-ice cover (Ramadhan et al., 2022; Gordon, 1981), and upwelling of the CDW along the Antarctic divergence zone (Morrison et al., 2015; Wilson et al., 2019; Ramadhan et al., 2022). In particular, we attributed the increased biological productivity found in these clusters to the CDW through a logistic regression. The inferred mechanisms can also be linked to other climate modes, such as the Southern Annular Mode and the Indian Ocean Dipole.

5.2 Potential Impacts of Column-Compound Extreme Events

Compounded extreme events can cause severe impacts when stressors interact synergistically (Gruber et al., 2021). This synergism can occur in different ways. The most direct effects occur when an organism experiences multiple stressors in the same place and time (Le Grix et al., 2021; Burger et al., 2022). In our study, we additionally consider the contraction of habitable space within the water column during CCX, where extremes may occur at different depths. This contraction may lead to indirect impacts related to predator evasion or food availability.

Co-located and co-temporal events exacerbate impacts on organisms to which multiple stressors are synergistically detrimental and are highly dependent on species and life stage (Kroeker et al., 2013; Deutsch et al., 2015; Gobler & Baumann, 2016). During compounded MHW and LOX, thermal stress increases metabolism and drives additional oxygen demand in ectotherms (Pörtner, 2002; K. E. Smith et al., 2023). The coinciding low-oxygen environment further hinders the ability of organisms to survive, grow, or recruit. Recent work has quantified this effect into a composite "metabolic" or "aerobic growth" index (Deutsch et al., 2015; Clarke et al., 2021). MHW and LOX occurring at the same place and time will pose a large threat in this case, although they have been shown to be relatively uncommon in this work. However, a strong MHW can simultaneously induce lower oxygen (due to lower solubility) and reduce the low oxygen tolerance threshold of the organism (through increased metabolism), effectively increasing the oxygen threshold beyond those used in this study. Furthermore, acidic conditions have been shown to increase metabolic stress (Pan et al., 2015; Engström-Öst et al., 2019; Tai et al., 2021; Lattuca et al., 2023). Thus, the co-occurrence of OAX adds another layer of metabolic demand. Every organism has a different metabolic threshold (Deutsch et al., 2015), and it is beyond the range of this study to identify the impacts on any particular species. However, higher-resolution regional studies (Franco et al., 2022) in conjunction with laboratory studies (Seibel et al., 2016) will be able to identify the impacts on metabolism of any given species.

Up to now, there has been very little work on the compression of marine habitats due to extreme events (Desmet et al., 2022; Köhn et al., 2022), and much less so with compounded extreme stressors. In this study, we show that when CCX occur, the remaining contiguous habitable space is less than half of the upper ocean water column on average. This fraction is reduced further when multiple extremes occur in different parts of the water column. Vertically migrating organisms are expected to be especially affected by CCX, as they depend on the habitable water column for essential biological activities. Diel vertical migration (DVM) is understood to be performed by planktonic species for the purpose of food gathering and predator avoidance (Ritz et al., 2011), and is a behavioural response to light (Cohen & Forward, 2019). Little is known about the impact of marine extremes on DVM, except that some species regularly migrate to low oxygen and low pH environments (Riquelme-Bugueño et al., 2020). When extreme conditions occur close to the surface, the habitable space of migrating organisms is reduced. They may avoid extreme conditions on the surface, thereby reducing food availability, or simply continue to migrate upward into extreme conditions, increasing metabolism

and food demand. In either case, the ability of organisms to grow and survive is reduced. In the event of a CCX that covers both the surface and the subsurface, the migrating organisms have no good choice to make and are simply subject to extreme conditions wherever they are. Habitat contraction may further affect organisms in more indirect ways. Extreme conditions on the surface may force marine fish to migrate to the subsurface (Jorda et al., 2020), decreasing the survivability of zooplankton species that use the darker environment to avoid predators. The impact of column extreme events on such vertically migrating organisms can be quantified with the choice of threshold. While a small vertical displacement of $[H^+]$ or $[O_2]$ anomalies may not lead to much impact, a choice of at least 50 m in this study implies that organisms could be 50 m away from waters with normal conditions, increasing the amount of time spent in extreme conditions.

Although we cannot yet identify the specific biological impacts of the compound extremes that we identified and described in this study, we point out that these CCX occur in ecologically and biogeochemically sensitive regions. Of particular concern is the tropical nature of many CCX, given that these regions contain the highest diversity across nearly all trophic levels (Tittensor et al., 2010), ranging from phytoplankton (Righetti et al., 2019), zooplankton (Benedetti et al., 2021), fish (Stuart-Smith et al., 2013), to top predators (Worm & Tittensor, 2018). Furthermore, these tropical regions are also the locations of major fisheries (Watson, 2017). The co-occurrence of many double and triple compound extremes in the central and eastern tropical Pacific make this region among the most vulnerable. Also of concern are the western tropical Pacific, Southeast Asian seas, and the Coral Sea where MHW-OAX and OAX-LOX are found to occur, while being characterised as the world's region with the highest marine biodiversity (Tittensor et al., 2010). Furthermore, the EBUS, home to some of the highest fishery catches, are subject to regular compound extremes (especially OAX-LOX). In addition, the frequent occurrence of very intense MHW-OAX events in the high-latitude Southern Ocean hits a very sensitive ecosystem, with a relatively high diversity (Chown et al., 2015) and home to very unique organisms and ecosystems (Hill et al., 2006; Constable et al., 2014).

5.3 Caveats and Limitations

In this study, extreme events in the model hindcast were evaluated with respect to surface MHW and OAX only. The evaluation of surface OAX with OceanSODA-ETHZ (Gregor & Gruber, 2021) showed a tendency of the model towards longer and more intense events on the surface. A large fraction of this bias is located in regions with strong thermocline variability, and hence we also expect it to apply to detected LOX, due to their high co-occurrence with OAX. On the other hand, some part of this bias may also be attributed to the relatively lower variability in the OceanSODA-ETHZ product (Ma et al., 2023). Overall, we expect the impact of potential biases on our results to be restricted to particular metrics, perhaps most importantly the intensity and duration of the events. In contrast, the spatial structure of the CCX and their co-occurrence propensity is likely much less affected, as these are related to their underlying physical and biogeochemical processes, which we consider well captured by the model. One option for the subsurface evaluation of these properties is emerging from the rapidly increasing number of observations from the Biogeochemical Argo float program (Johnson & Claustre, 2016). These observations could be used to evaluate $[H^+]$ and $[O_2]$ in the subsurface. In particular, we used the GOBAI-O2 product (Sharp et al., 2022) to evaluate the mean state of $[O_2]$, although the time period covered is too short to establish a baseline for LOX. We found that the CESM hindcast has a tendency to overestimate $[O_2]$ in confined regions within all ocean basins, particularly in oxygen-deficient zones, while making an underestimation elsewhere, such as in the west Pacific. This leads to biases in the 150 μM depth of $[O_2]$, by up to $\pm$40 m, and should be taken into account when considering the subsurface OAX and LOX. Still, we do not expect the main findings to be different, since the subsurface column extremes tend to extend over 100 m in range.

A second caveat concerns the relatively low spatial resolution of the CESM hindcast, particularly near the poles. Small-scale, local processes are not captured by the model, and thus we are unable conduct analyses regarding such physical mechanisms. The CCX identified in the Southern Ocean have been linked to variations in the upwelling of the CDW and surface wind stress, which are large enough to be represented by the CESM hindcast. Still, considering the moderate resolution of our model, our results are biased towards CCX extending over substantial spatial scales, and represent the low to mid latitudes better with a higher resolution.

The third caveat concerns the choice of criteria used to identify extremes. Our choices were made with the intention to investigate the co-occurrence of multiple stressors within the vertical column in a systematic and consistent manner, linking them to drivers and mechanisms based on their spatiotemporal characteristics. For this work, the moving baseline was primarily used, as it is more suitable for the investigation of drivers behind extreme events. However, in Figures 5 and 6, it was shown that the detected volume fraction is vastly different between the fixed and moving baselines. The results on the moving baseline are unable to show the worsening conditions of the global ocean under climate change, nor the change in propensity of extreme events under such conditions. For such an analysis, the fixed baseline may be a better choice.

Furthermore, the relative percentile thresholds used in this study are not targeted toward specific biological thresholds or marine organisms. Therefore, the biological impacts of the extremes identified in this study cannot be directly quantified. For example, MHW-OAX CCX are generally absent in the EBUS, although temperature-induced OAX are known to occur during MHW. This is likely because the OAX occurrences in these regions are dominated by anomalous upwelling events, which increase $[H^+]$ more strongly compared to MHW. Thus, we see more OAX-LOX occurring in the EBUS. However, this does not mean that the MHW-induced high $[H^+]$ is irrelevant, as organisms may still be affected. In such scenarios, it is better to rely on species-specific thresholds as the basis for extreme detection (Le Grix et al., 2023). This limitation on biological impacts also extends to the definition of CCX, where a vertical extent of at least 50 m of each extreme type is required. An organism whose metabolism is affected by temperature could be affected by either MHW or LOX, and not necessarily only when both occur. It may then be a better choice to define extreme conditions based on the metabolic rate of the particular organism and the oxygen concentration in the water.

Finally, the choice of the absolute threshold for oxygen was intended to exclude LOX detected in waters with sufficiently high $[O_2]$ for most higher trophic organisms. However, a case can also be made for a lower oxygen threshold to exclude waters which are permanently hypoxic ($0-60\,\mu$M), even if the relative threshold is exceeded. Such regions (seen in Figure S9) may already be uninhabitable for most species, and LOX detected there may have less ecological significance.

6 Summary and Conclusions

With this work on CCX, we took a first step in characterising extremes that are compounded in the vertical water column. CCX are detected in the global ocean on a CESM-BEC daily hindcast from 1961 to 2020. Key characteristics such as frequency, duration, intensity, and reduction of habitable space are assessed, to determine the regions where CCX are the most severe. These are the subtropics and Southern Ocean for MHW-OAX, and the tropics and north Pacific for OAX-LOX, MHW-LOX, and MHW-OAX-LOX. All CCX substantially increase in their intensity, frequency, and spatial extent, primarily driven by ocean warming and the increase in ocean acidity due to the oceanic uptake of anthropogenic CO_2 from the atmosphere.

Within the vertical column, the depths where single extremes occur during CCX are analysed to determine the mechanisms behind them. We find that ENSO-associated CCX tend to be driven by a single mechanism such as increased air-sea heat flux or increased upwelling, resulting in co-located compounded events. On the other hand, there is a significant proportion of CCX in which the single constitutive extremes occur in different parts of the vertical column. These tend to be driven by separate drivers and have a reduced association with ENSO events.

Marine extreme events can have a large impact on pelagic organisms, which are usually affected by multiple stressors, rather than a single stressor. These organisms swim or migrate vertically, experiencing various physical and chemical conditions. Therefore, the study of vertically compounded extremes advances our understanding of the impacts of extreme events on marine organisms. Furthermore, these extremes are likely to become more frequent and intense with the climate trend of increasing temperatures and atmospheric CO_2. Extreme conditions of the past may well become the mean state of the ocean in the future. Further analysis of such column-compound events on regional scales or with regard to specific organisms will extend our understanding of their future impacts.

Open Research

All data to reproduce the plots can be found in the following repository (Wong et al., 2024): `https://doi.org/10.3929/ethz-b-000654113`. The standard monthly output of the CESM model simulations is available through the RECCAP2 Zenodo repository (Müller, 2023): `https://zenodo.org/records/7990823`.

Conflict of Interest Statement

The authors have no conflicts of interest to declare.

Acknowledgments
This project has received funding from the European Union's Horizon 2020 research and innovation programme under grant agreement No 820989 (COMFORT). The authors thank Dr. Damian Loher for his modeling support, and Dr. Eike Köhn, Dr. Luke Gregor, and Dr. Fabio Benedetti for useful discussions. The authors also thank the two reviewers for their time and expertise in improving the quality and clarity of this manuscript.

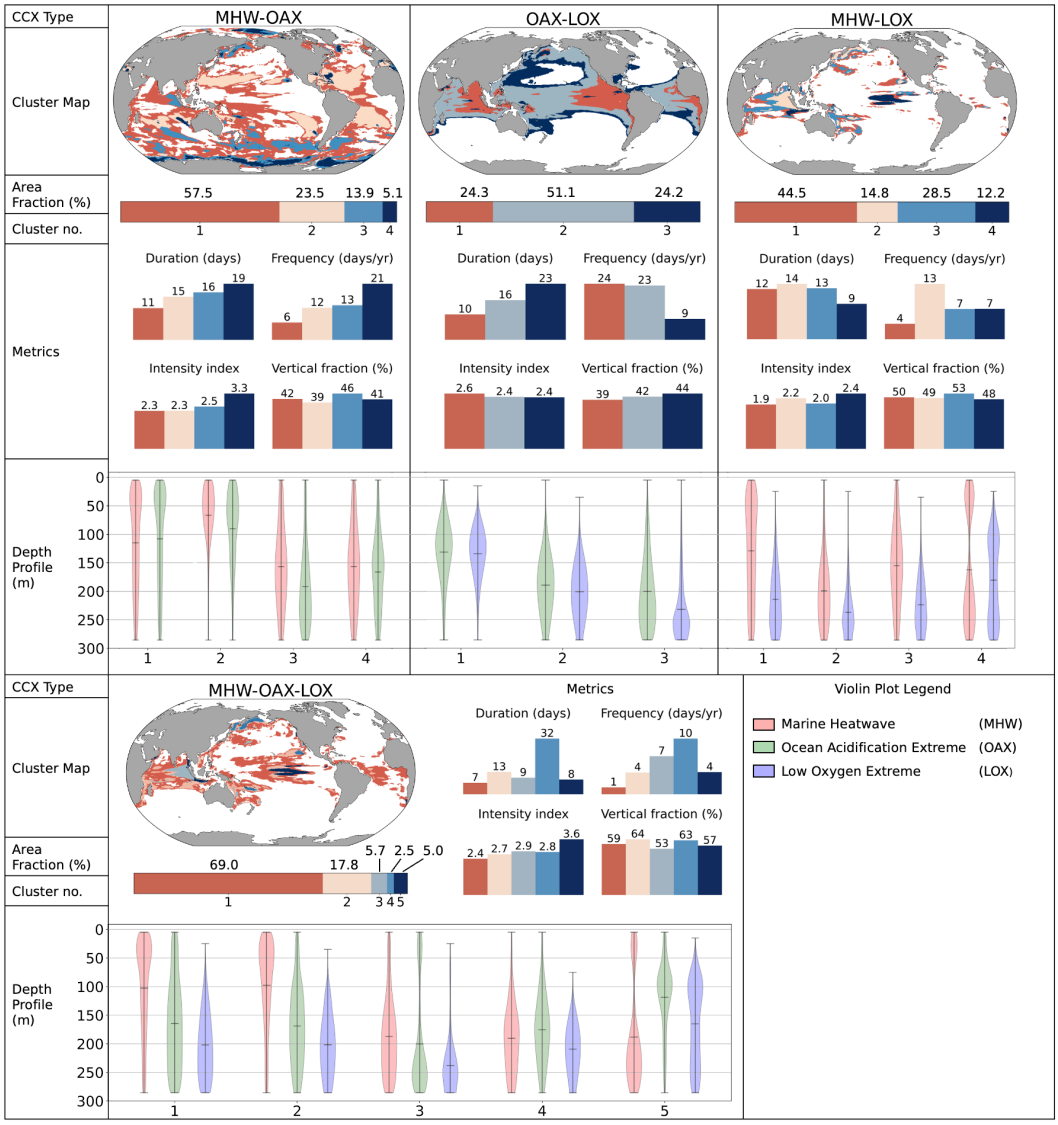

Figure 10. Summary of the main cluster characteristics identified by k-means clustering for each CCX type, i.e., MHW-LOX (top left column), OAX-LOX (top middle column), MHW-LOX (top right column), and the triple CCX MHW-OAX-LOX (bottom row). For each type, four groups of characteristics are provided (from the top): Horizontal distribution by a cluster map, cluster numbers and the area fraction occupied by each cluster as a horizontal bar plot, key metrics including cluster-averaged values of mean duration, mean days per year, mean annual column-maximum intensity index, and mean vertical fraction occupied by extremes as a vertical bar plots, and vertical distribution in the form of vertical violin plots. The latter show the sum of single grid-cell extreme occurrences during CCX, weighted by their intensity index.

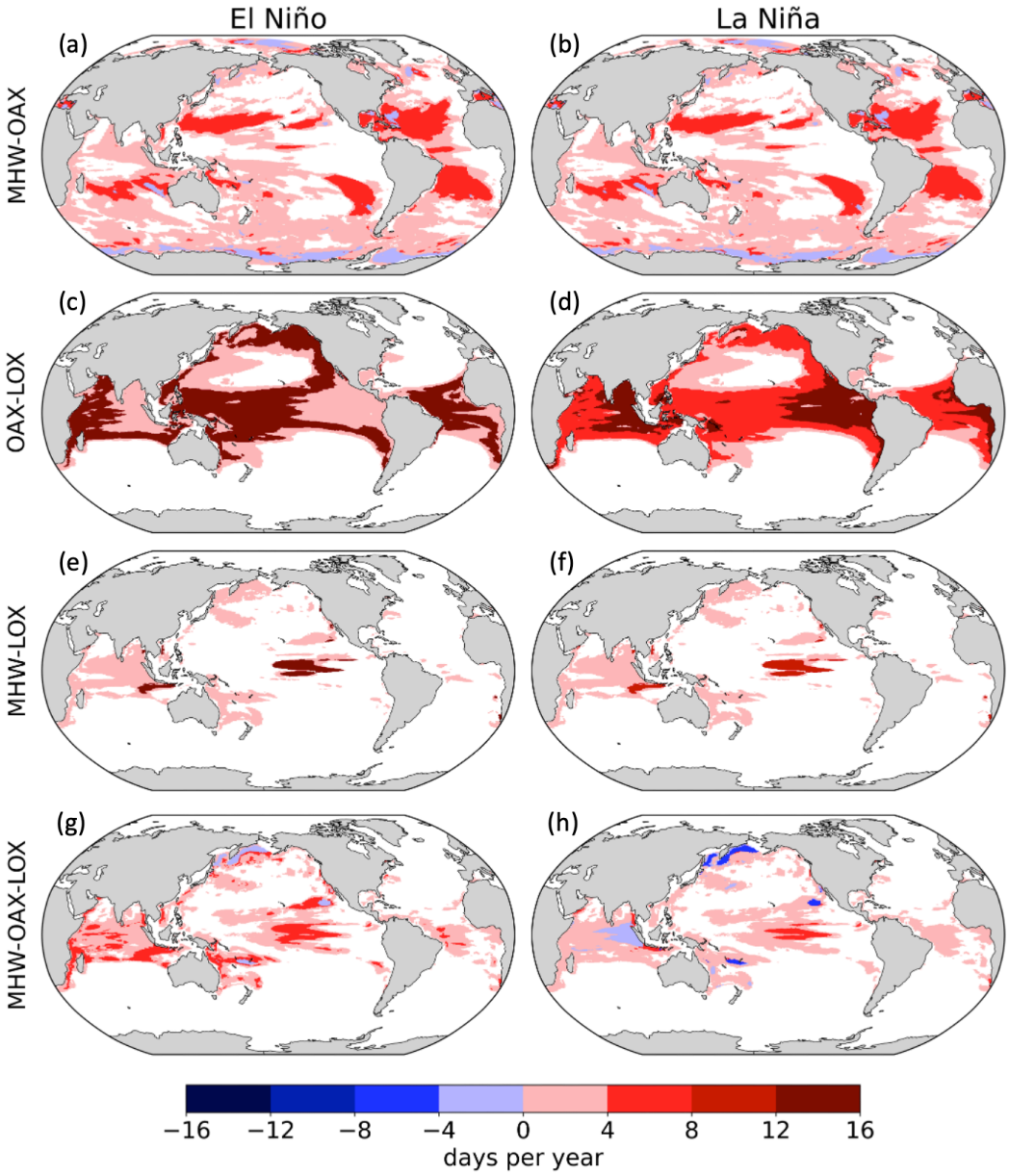

Figure 11. Maps illustrating the impact of ENSO on the number of extreme days for each CCX type, averaged by cluster. Shown are changes of annual CCX days during positive (left column) and negative (right column) ENSO phases, compared to a neutral ENSO phase. Each row corresponds to one CCX type, i.e. (a-b): MHW-OAX, (c-d): OAX-LOX, (e-f): MHW-LOX, (g-h): MHW-OAX-LOX. In this figure, a year is defined to begin in July and end in June of the next year. All values shown in this figure are significant ($p < 0.05$ Welch's t-test.)

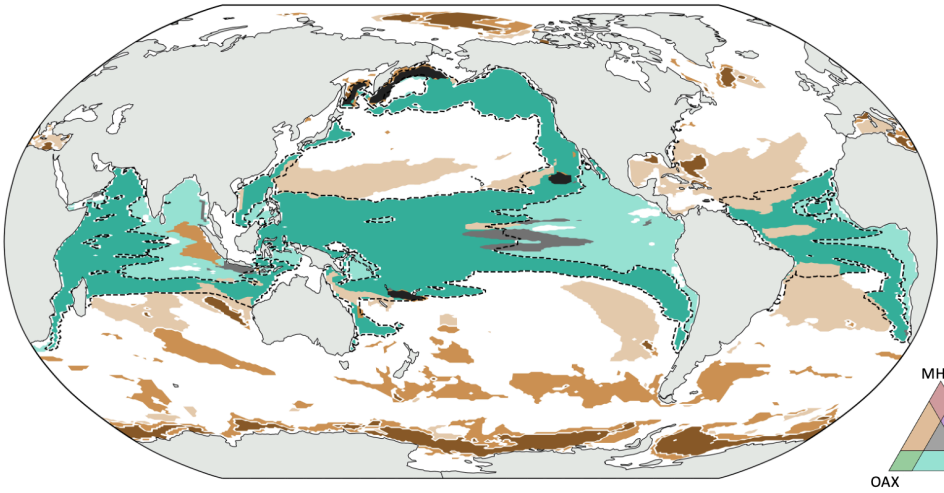

Cluster	MHW-OAX 2	MHW-OAX 3	MHW-OAX 4	OAX-LOX 1	OAX-LOX 2	MHW-OAX-LOX 4	MHW-OAX-LOX 5
Associated Regions	Subtropics, Tropics	Subantarctic	Antarctic	EBUS, East tropics	West tropics, OMZs	Western Subarctic Pacific	Central Tropical Pacific
Time-depth Schematic							
Duration (days)	15 (49)	16 (40)	19 (29)	10 (27)	16 (39)	32 (52)	8 (13)
Frequency (days per year)	12 (81)	13 (58)	21 (50)	24 (67)	23 (53)	10 (20)	4 (16)
Intensity Index	2.3 (11.5)	2.5 (9.7)	3.3 (7.8)	2.6 (5.6)	2.4 (5.9)	2.8 (4.5)	3.6 (5.4)
Vertical Extent (%)	39 (88)	46 (83)	41 (79)	39 (70)	42 (75)	63 (81)	57 (75)
ENSO (+/-) change (days)	+6/+5	+1/+1	-3/-4	+2/+14	+15/+7	-2/-5	+7/+5

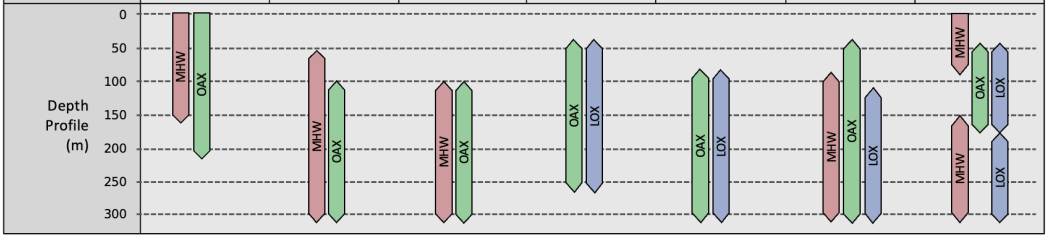

Figure 12. Synthesis figure of CCX properties in selected clusters. Map: Selected clusters of CCX in a composite plot. The extent of OAX-LOX 1 and OAX-LOX 2 are marked by dashed lines to indicate their overlap with other clusters. Table (from top to bottom): Cluster names and their associated regions. Time-depth schematics that are drawn to illustrate actual extreme conditions seen in the hindcast. Cluster mean values of mean duration, mean frequency, mean maximum intensity index, mean vertical extent, and change in number of CCX days during positive and negative ENSO periods. Values in parentheses are of the fixed baseline. Lastly, the approximate vertical locations of single extremes during CCX are represented with simplified bars.

References

Amaya, D. J., Jacox, M. G., Alexander, M. A., Scott, J. D., Deser, C., Capotondi, A., & Phillips, A. S. (2023, March). Bottom marine heatwaves along the continental shelves of North America. *Nature Communications*, *14*(1), 1038. doi: 10.1038/s41467-023-36567-0

Ando, K., & McPhaden, M. J. (1997). Variability of surface layer hydrography in the tropical Pacific Ocean. *Journal of Geophysical Research: Oceans*, *102*(C10), 23063–23078. doi: 10.1029/97JC01443

Basyuk, E., & Zuenko, Y. (2020). Extreme oceanographic conditions in the northwestern Bering Sea in 2017–2018. *Deep-Sea Research Part II: Topical Studies in Oceanography*, *181-182*. doi: 10.1016/j.dsr2.2020.104909

Bednaršek, N., Feely, R. A., Beck, M. W., Glippa, O., Kanerva, M., & Engström-Öst, J. (2018). El Niño-related thermal stress coupled with upwelling-related ocean acidification negatively impacts cellular to population-level responses in pteropods along the California current system with implications for increased bioenergetic costs. *Frontiers in Marine Science*, *5*, 1–17. doi: 10.3389/fmars.2018.00486

Benedetti, F., Vogt, M., Elizondo, U. H., Righetti, D., Zimmermann, N. E., & Gruber, N. (2021). Major restructuring of marine plankton assemblages under global warming. *Nature Communications*, *12*(1), 5226. doi: 10.1038/s41467-021-25385-x

Bertrand, A., Ballón, M., & Chaigneau, A. (2010). Acoustic observation of living organisms reveals the upper limit of the oxygen minimum zone. *PLoS ONE*, *5*(4). doi: 10.1371/journal.pone.0010330

Bian, C., Jing, Z., Wang, H., Wu, L., Chen, Z., Gan, B., & Yang, H. (2023). Oceanic mesoscale eddies as crucial drivers of global marine heatwaves. *Nature Communications*, *14*(1), 2970. doi: 10.1038/s41467-023-38811-z

Bianchi, D., & Mislan, K. A. (2016). Global patterns of diel vertical migration times and velocities from acoustic data. *Limnology and Oceanography*, *61*(1), 353–364. doi: 10.1002/lno.10219

Bianchi, D., Stock, C., Galbraith, E. D., & Sarmiento, J. L. (2013). Diel vertical migration: Ecological controls and impacts on the biological pump in a one-dimensional ocean model. *Global Biogeochemical Cycles*, *27*(2), 478–491. doi: 10.1002/gbc.20031

Bograd, S. J., Buil, M. P., Lorenzo, E. D., Castro, C. G., Schroeder, I. D., Goericke, R., ... Whitney, F. A. (2015). Changes in source waters to the Southern California Bight. *Deep-Sea Research Part II: Topical Studies in Oceanography*, *112*, 42–52. doi: 10.1016/j.dsr2.2014.04.009

Boyd, P. W., & Brown, C. J. (2015). Modes of interactions between environmental drivers and marine biota. *Frontiers in Marine Science*, *2*, 1–7. doi: 10.3389/fmars.2015.00009

Braun, C. D., Kaplan, M. B., Horodysky, A. Z., & Llopiz, J. K. (2015). Satellite telemetry reveals physical processes driving billfish behavior. *Animal Biotelemetry*, *3*(1). doi: 10.1186/s40317-014-0020-9

Burger, F. A., & Frölicher, T. L. (2023). Drivers of Surface Ocean Acidity Extremes in an Earth System Model. *Global Biogeochemical Cycles*, *37*(9), e2023GB007785. doi: 10.1029/2023GB007785

Burger, F. A., John, J. G., & Frölicher, T. L. (2020). Increase in ocean acidity variability and extremes under increasing atmospheric CO_2. *Biogeosciences*, *17*(18), 4633–4662. doi: 10.5194/bg-17-4633-2020

Burger, F. A., Terhaar, J., & Frölicher, T. L. (2022). Compound marine heatwaves and ocean acidity extremes. *Nature Communications*, 1–12. doi: 10.1038/s41467-022-32120-7

Carvalho, K. S., Smith, T. E., & Wang, S. (2021, September). Bering Sea marine heatwaves: Patterns, trends and connections with the Arctic. *Journal of Hy-*

drology, *600*, 126462. doi: 10.1016/j.jhydrol.2021.126462

Chan, F., Barth, J. A., Lubchenco, J., Kirincich, A., Weeks, H., Peterson, W. T., & Menge, B. A. (2008). Emergence of anoxia in the California current large marine ecosystem. *Science*, *319*(5865), 920. doi: 10.1126/science.1149016

Chhak, K., & Di Lorenzo, E. (2007). Decadal variations in the California Current upwelling cells. *Geophysical Research Letters*, *34*(14), 1–6. doi: 10.1029/2007GL030203

Chiswell, S. M. (2022). Global Trends in Marine Heatwaves and Cold Spells: The Impacts of Fixed Versus Changing Baselines. *Journal of Geophysical Research: Oceans*, *127*(10), e2022JC018757. doi: 10.1029/2022JC018757

Chown, S. L., Clarke, A., Fraser, C. I., Cary, S. C., Moon, K. L., & McGeoch, M. A. (2015). The changing form of Antarctic biodiversity. *Nature*, *522*(7557), 431–438. doi: 10.1038/nature14505

Clarke, T. M., Wabnitz, C. C., Striegel, S., Frölicher, T. L., Reygondeau, G., & Cheung, W. W. (2021). Aerobic growth index (AGI): An index to understand the impacts of ocean warming and deoxygenation on global marine fisheries resources. *Progress in Oceanography*, *195*. doi: 10.1016/j.pocean.2021.102588

Cohen, J. H., & Forward, R. B. (2019). Vertical Migration of Aquatic Animals. In J. C. Choe (Ed.), *Encyclopedia of Animal Behavior (Second Edition)* (pp. 546–552). Oxford: Academic Press. doi: 10.1016/B978-0-12-809633-8.01257-7

Collins, M., Sutherland, M., Bouwer, L., Cheong, S.-M., Frölicher, T., Des Combes, H. J., ... Tibig, L. (2019). *Extremes, Abrupt Changes and Managing Risks* (Tech. Rep.).

Constable, A. J., Melbourne-Thomas, J., Corney, S. P., Arrigo, K. R., Barbraud, C., Barnes, D. K. A., ... Ziegler, P. (2014). Climate change and Southern Ocean ecosystems I: how changes in physical habitats directly affect marine biota. *Global Change Biology*, *20*(10), 3004–3025. doi: 10.1111/gcb.12623

Crain, C. M., Kroeker, K., & Halpern, B. S. (2008). Interactive and cumulative effects of multiple human stressors in marine systems. *Ecology Letters*, *11*(12), 1304–1315. doi: 10.1111/j.1461-0248.2008.01253.x

Deser, C., Phillips, A. S., Alexander, M. A., Amaya, D. J., Capotondi, A., Jacox, M. G., & Scott, J. D. (2024). Future Changes in the Intensity and Duration of Marine Heat and Cold Waves: Insights from Coupled Model Initial-Condition Large Ensembles. *Journal of Climate*, *37*(6), 1877–1902. doi: 10.1175/JCLI-D-23-0278.1

Desmet, F., Gruber, N., Köhn, E. E., Münnich, M., & Vogt, M. (2022). Tracking the space-time evolution of ocean acidification extremes in the California Current System and Northeast Pacific. *Journal of Geophysical Research: Oceans*, 1–30. doi: 10.1029/2021jc018159

Deutsch, C., Ferrel, A., Seibel, B., Pörtner, H.-O., & Huey, R. B. (2015). Climate change tightens a metabolic constraint on marine habitats. *Science*, *348*(6239), 1132–1136. doi: DOI:10.1126/science.aaa1605

DeVries, T., Yamamoto, K., Wanninkhof, R., Gruber, N., Hauck, J., Müller, J. D., ... Zeng, J. (2023). Magnitude, Trends, and Variability of the Global Ocean Carbon Sink From 1985 to 2018. *Global Biogeochemical Cycles*, *37*(10). doi: 10.1029/2023GB007780

Diaz, R. J., & Rosenberg, R. (2008). Spreading Dead Zones and Consequences for Marine Ecosystems. *Science*, *321*(5891), 926–929. doi: 10.1126/science.1156401

Di Lorenzo, E., & Mantua, N. (2016). Multi-year persistence of the 2014/15 North Pacific marine heatwave. *Nature Climate Change*, *6*(11), 1042–1047. doi: 10.1038/nclimate3082

Dinniman, M. S., Klinck, J. M., & Smith, W. O. (2011). A model study of Circumpolar Deep Water on the West Antarctic Peninsula and Ross Sea continental shelves. *Deep Sea Research Part II: Topical Studies in Oceanography*, *58*(13-

16), 1508–1523. doi: 10.1016/j.dsr2.2010.11.013

Ebita, A., Kobayashi, S., Ota, Y., Moriya, M., Kumabe, R., Onogi, K., ... Ishimizu, T. (2011). The Japanese 55-year Reanalysis "JRA-55": An Interim Report. *Sola*, *7*, 149–152. doi: 10.2151/sola.2011-038

Elzahaby, Y., Schaeffer, A., Roughan, M., & Delaux, S. (2021). Oceanic Circulation Drives the Deepest and Longest Marine Heatwaves in the East Australian Current System. *Geophysical Research Letters*, *48*(17), e2021GL094785. doi: 10.1029/2021GL094785

Engström-Öst, J., Glippa, O., Feely, R. A., Kanerva, M., Keister, J. E., Alin, S. R., ... Bednaršek, N. (2019). Eco-physiological responses of copepods and pteropods to ocean warming and acidification. *Scientific Reports*, *9*(1), 1–13. doi: 10.1038/s41598-019-41213-1

Feng, M., Zhang, N., Liu, Q., & Wijffels, S. (2018). The Indonesian throughflow, its variability and centennial change. *Geoscience Letters*, *5*(1), 3. doi: 10.1186/s40562-018-0102-2

Fiedler, P. C. (2010). Comparison of objective descriptions of the thermocline. *Limnology and Oceanography: Methods*, *8*(6), 313–325. doi: 10.4319/lom.2010.8.313

Fiedler, P. C., & Lavín, M. F. (2017). Oceanographic Conditions of the Eastern Tropical Pacific. In P. W. Glynn, D. P. Manzello, & I. C. Enochs (Eds.), *Coral Reefs of the Eastern Tropical Pacific: Persistence and Loss in a Dynamic Environment* (pp. 59–83). Dordrecht: Springer Netherlands. doi: 10.1007/978-94-017-7499-4_3

Fiedler, P. C., & Talley, L. D. (2006). Hydrography of the eastern tropical Pacific: A review. *Progress in Oceanography*, *69*(2-4), 143–180. doi: 10.1016/j.pocean.2006.03.008

Filho, W. L. F. C., Lucio, P. S., & Spyrides, M. H. C. (2013). Precipitation Extremes Analysis over the Brazilian Northeast via Logistic Regression. *Atmospheric and Climate Sciences*, *2014*. doi: 10.4236/acs.2014.41007

Fragkopoulou, E., Sen Gupta, A., Costello, M. J., Wernberg, T., Araújo, M. B., Serrão, E. A., ... Assis, J. (2023, September). Marine biodiversity exposed to prolonged and intense subsurface heatwaves. *Nature Climate Change*, 1–8. doi: 10.1038/s41558-023-01790-6

Franco, A. C., Kim, H., Frenzel, H., Deutsch, C., Ianson, D., Sumaila, U. R., & Tortell, P. D. (2022). Impact of warming and deoxygenation on the habitat distribution of Pacific halibut in the Northeast Pacific. *Fisheries Oceanography*, *31*(6), 601–614. doi: 10.1111/fog.12610

Friedlingstein, P., Jones, M. W., Sullivan, M. O., Andrew, R. M., Bakker, D. C. E., Hauck, J., ... Peters, W. (2022). Global Carbon Budget 2021. *Earth System Science Data*, 1917–2005. doi: 10.5194/essd-14-4811-2022

Frischknecht, M., Münnich, M., & Gruber, N. (2018). Origin, Transformation, and Fate: The Three-Dimensional Biological Pump in the California Current System. *Journal of Geophysical Research: Oceans*, *123*(11), 7939–7962. doi: 10.1029/2018JC013934

Frölicher, T. L., Fischer, E. M., & Gruber, N. (2018). Marine heatwaves under global warming. *Nature*, *560*(7718), 360–364. doi: 10.1038/s41586-018-0383-9

Gent, P. R., Danabasoglu, G., Donner, L. J., Holland, M. M., Hunke, E. C., Jayne, S. R., ... Zhang, M. (2011). The Community Climate System Model Version 4. *Journal of Climate*, *24*(19), 4973–4991. doi: 10.1175/2011JCLI4083.1

Gilly, W. F., Michael Beman, J., Litvin, S. Y., & Robison, B. H. (2013). Oceanographic and biological effects of shoaling of the oxygen minimum zone. *Annual Review of Marine Science*, *5*, 393–420. doi: 10.1146/annurev-marine-120710-100849

Gleckler, P. J., Durack, P. J., Stouffer, R. J., Johnson, G. C., & Forest, C. E. (2016). Industrial-era global ocean heat uptake doubles in recent decades.

Nature Climate Change, *6*(4), 394–398. doi: 10.1038/nclimate2915

Gobler, C. J., & Baumann, H. (2016). Hypoxia and acidification in ocean ecosystems: Coupled dynamics and effects on marine life. *Biology Letters*, *12*(5). doi: 10.1098/rsbl.2015.0976

Gordon, A. L. (1981). Seasonality of Southern Ocean Sea Ice. *Journal of Geophysical Research*, *86*(C5), 4193–4197. doi: 10.1029/JC086iC05p04193

Gregor, L., & Gruber, N. (2021). OceanSODA-ETHZ: A global gridded data set of the surface ocean carbonate system for seasonal to decadal studies of ocean acidification. *Earth System Science Data*, *13*(2), 777–808. doi: 10.5194/essd-13-777-2021

Gruber, N., Boyd, P. W., Frölicher, T. L., & Vogt, M. (2021). Ocean Biogeochemical Extremes and Compound Events. *Nature*, *600*, 395–407. doi: 10.1038/s41586-021-03981-7

Hauck, J., Gregor, L., Nissen, C., Patara, L., Hague, M., Mongwe, P., ... Terhaar, J. (2023). The Southern Ocean Carbon Cycle 1985–2018: Mean, Seasonal Cycle, Trends, and Storage. *Global Biogeochemical Cycles*, *37*(11), e2023GB007848. doi: 10.1029/2023GB007848

Hauck, J., Zeising, M., Le Quéré, C., Gruber, N., Bakker, D. C. E., Bopp, L., ... Séférian, R. (2020). Consistency and Challenges in the Ocean Carbon Sink Estimate for the Global Carbon Budget. *Frontiers in Marine Science*, *7*.

Hauri, C., Gruber, N., McDonnell, A. M., & Vogt, M. (2013). The intensity, duration, and severity of low aragonite saturation state events on the California continental shelf. *Geophysical Research Letters*, *40*(13), 3424–3428. doi: 10.1002/grl.50618

Hauri, C., Pagès, R., Hedstrom, K., Doney, S. C., Dupont, S., Ferriss, B., & Stuecker, M. F. (2024). More Than Marine Heatwaves: A New Regime of Heat, Acidity, and Low Oxygen Compound Extreme Events in the Gulf of Alaska. *AGU Advances*, *5*(1), e2023AV001039. doi: 10.1029/2023AV001039

Hauri, C., Pagès, R., McDonnell, A. M., Stuecker, M. F., Danielson, S. L., Hedstrom, K., ... Doney, S. C. (2021). Modulation of ocean acidification by decadal climate variability in the Gulf of Alaska. *Communications Earth and Environment*, *2*(1), 1–7. doi: 10.1038/s43247-021-00254-z

Hill, S. L., Murphy, E. J., Reid, K., Trathan, P. N., & Constable, A. J. (2006). Modelling Southern Ocean ecosystems: krill, the food-web, and the impacts of harvesting. *Biological Reviews*, *81*(4), 581–608. doi: 10.1017/S1464793106007123

Hobday, A. J., Alexander, L. V., Perkins, S. E., Smale, D. A., Straub, S. C., Oliver, E. C., ... Wernberg, T. (2016). A hierarchical approach to defining marine heatwaves. *Progress in Oceanography*, *141*, 227–238. doi: 10.1016/j.pocean.2015.12.014

Hobday, A. J., Oliver, E. C., Gupta, A. S., Benthuysen, J. A., Burrows, M. T., Donat, M. G., ... Smale, D. A. (2018). Categorizing and naming marine heatwaves. *Oceanography*, *31*(2), 162–173. doi: 10.5670/oceanog.2018.205

Hofmann, A. F., Peltzer, E. T., Walz, P. M., & Brewer, P. G. (2011). Hypoxia by degrees: Establishing definitions for a changing ocean. *Deep-Sea Research Part I: Oceanographic Research Papers*, *58*(12), 1212–1226. doi: 10.1016/j.dsr.2011.09.004

Holbrook, N. J., Claar, D. C., Hobday, A. J., McInnes, K. L., Oliver, E. C. J., Gupta, A. S., ... Zhang, X. (2020). ENSO-Driven Ocean Extremes and Their Ecosystem Impacts. *El Niño Southern Oscillation in a Changing Climate*, 409–428.

Holbrook, N. J., Scannell, H. A., Sen Gupta, A., Benthuysen, J. A., Feng, M., Oliver, E. C., ... Wernberg, T. (2019). A global assessment of marine heatwaves and their drivers. *Nature Communications*, *10*(1), 1–13. doi: 10.1038/s41467-019-10206-z

Holbrook, N. J., Sen Gupta, A., Oliver, E. C. J., Hobday, A. J., Benthuysen,

J. A., Scannell, H. A., ... Wernberg, T. (2020). Keeping pace with marine heatwaves. *Nature Reviews Earth & Environment*, *1*(9), 482–493. doi: 10.1038/s43017-020-0068-4

Huang, B., Liu, C., Banzon, V., Freeman, E., Graham, G., Hankins, B., ... Zhang, H.-M. (2021, April). Improvements of the Daily Optimum Interpolation Sea Surface Temperature (DOISST) Version 2.1. *Journal of Climate*, *34*(8), 2923–2939. doi: 10.1175/JCLI-D-20-0166.1

Hunke, E., & Lipscomb, W. (2008). *CICE: The Los Alamos sea ice model documentation and software user's manual version 4.0* (Tech. Rep.). Los Alamos NM 87545: T-3 Fluid Dynamics Group, Los Alamos National Laboratory.

Jacox, M. G. (2019). Marine heatwaves in a changing climate. *Nature*, *571*(7766), 485–487. doi: 10.1038/d41586-019-02196-1

Johnson, K., & Claustre, H. (2016). The scientific rationale, design, and implementation plan for a Biogeochemical-Argo float array. *Biogeochemical-Argo Planning Group*. doi: 10.13155/46601

Jorda, G., Marbà, N., Bennett, S., Santana-Garcon, J., Agusti, S., & Duarte, C. M. (2020). Ocean warming compresses the three-dimensional habitat of marine life. *Nature Ecology and Evolution*, *4*(1), 109–114. doi: 10.1038/s41559-019-1058-0

Kroeker, K. J., Kordas, R. L., Crim, R., Hendriks, I. E., Ramajo, L., Singh, G. S., ... Gattuso, J. P. (2013). Impacts of ocean acidification on marine organisms: Quantifying sensitivities and interaction with warming. *Global Change Biology*, *19*(6), 1884–1896. doi: 10.1111/gcb.12179

Kwiatkowski, L., & Orr, J. C. (2018). Diverging seasonal extremes for ocean acidification during the twenty-first century. *Nature Climate Change*, *8*(2), 141–145. doi: 10.1038/s41558-017-0054-0

Kwiatkowski, L., Torres, O., Bopp, L., Aumont, O., Chamberlain, M., Christian, J. R., ... Ziehn, T. (2020). Twenty-first century ocean warming, acidification, deoxygenation, and upper-ocean nutrient and primary production decline from CMIP6 model projections. *Biogeosciences*, *17*(13), 3439–3470. doi: 10.5194/bg-17-3439-2020

Köhn, E. E., Münnich, M., Vogt, M., Desmet, F., & Gruber, N. (2022). Strong Habitat Compression by Extreme Shoaling Events of Hypoxic Waters in the Eastern Pacific. *Journal of Geophysical Research: Oceans*, *127*(6). doi: 10.1029/2022jc018429

Lattuca, M. E., Vanella, F. A., Malanga, G., Rubel, M. D., Manríquez, P. H., Torres, R., ... Fernández, D. A. (2023). Ocean acidification and seasonal temperature extremes combine to impair the thermal physiology of a sub-Antarctic fish. *Science of the Total Environment*, *856*. doi: 10.1016/j.scitotenv.2022.159284

Lauvset, S. K., Key, R. M., Olsen, A., van Heuven, S., Velo, A., Lin, X., ... Watelet, S. (2016, August). A new global interior ocean mapped climatology: the $1^\circ \times 1^\circ$ GLODAP version 2. *Earth System Science Data*, *8*(2), 325–340. doi: 10.5194/essd-8-325-2016

Ledwell, J. R., St. Laurent, L. C., Girton, J. B., & Toole, J. M. (2011). Diapycnal mixing in the antarctic circumpolar current. *Journal of Physical Oceanography*, *41*(1), 241–246. doi: 10.1175/2010JPO4557.1

Le Grix, N., Cheung, W. L., Reygondeau, G., Zscheischler, J., & Frölicher, T. L. (2023). Extreme and compound ocean events are key drivers of projected low pelagic fish biomass. *Global Change Biology*, *29*(23), 6478–6492. doi: 10.1111/gcb.16968

Le Grix, N., Zscheischler, J., Laufkötter, C., Rousseaux, C. S., & Frölicher, T. L. (2021). Compound high-temperature and low-chlorophyll extremes in the ocean over the satellite period. *Biogeosciences*, *18*(6), 2119–2137. doi: 10.5194/bg-18-2119-2021

Le Grix, N., Zscheischler, J., Rodgers, K. B., Yamaguchi, R., & Frölicher, T. L. (2022). Hotspots and drivers of compound marine heatwaves and low net primary production extremes. *Biogeosciences*, *19*(24), 5807–5835. doi: 10.5194/bg-19-5807-2022

Leung, S., Mislan, K. A. S., Muhling, B., & Brill, R. (2019). The significance of ocean deoxygenation for open ocean tunas and billfishes. In *'Laffoley, D. & Baxter, J.M. (eds.) (2019). Ocean deoxygenation: Everyone's problem - Causes, impacts, consequences and solutions.* (pp. 277–308). IUCN, Gland, Switzerland. doi: 10.2305/IUCN.CH.2019.13.en

Leung, S., Thompson, L. A., McPhaden, M. J., & Mislan, K. A. (2019). ENSO drives near-surface oxygen and vertical habitat variability in the tropical Pacific. *Environmental Research Letters*, *14*(6). doi: 10.1088/1748-9326/ab1c13

Luo, J. J., Zhang, R., Behera, S. K., Masumoto, Y., Jin, F. F., Lukas, R., & Yamagata, T. (2010). Interaction between El Niño and extreme Indian Ocean dipole. *Journal of Climate*, *23*(3), 726–742. doi: 10.1175/2009JCLI3104.1

Luyten, R., J., Pedlosky, J., & Stommel, J. (1983). The Ventilated Thermocline. *Journal of Physical Oceanography*. doi: 10.1175/1520-0485(1983)013⟨0292:TVT⟩2.0.CO;2

Ma, D., Gregor, L., & Gruber, N. (2023). Four Decades of Trends and Drivers of Global Surface Ocean Acidification. *Global Biogeochemical Cycles*, *37*(7), e2023GB007765. doi: 10.1029/2023GB007765

MacQueen, J. (1967). Some methods for classification and analysis of multivariate observations. In *Proceedings of the fifth Berkeley symposium on mathematical statistics and probability* (Vol. 1, pp. 281–297). Oakland, CA, USA.

Mahlstein, I., Martius, O., Chevalier, C., & Ginsbourger, D. (2012). Changes in the odds of extreme events in the Atlantic basin depending on the position of the extratropical jet. *Geophysical Research Letters*, *39*(22). doi: 10.1029/2012GL053993

Marin, M., Feng, M., Bindoff, N. L., & Phillips, H. E. (2022). Local Drivers of Extreme Upper Ocean Marine Heatwaves Assessed Using a Global Ocean Circulation Model. *Frontiers in Climate*, *4*. doi: 10.3389/fclim.2022.788390

Masson-Delmotte, V., P. Z., A. Pirani, S. L. Connors, C. Péan, S. Berger, ... B. Zhou (eds.) (2021). *IPCC, 2021: Summary for Policymakers. In: Climate Change 2021: The Physical Science Basis. Contribution of Working Group I to the Sixth Assessment Report of the Intergovernmental Panel on Climate Change* (Tech. Rep.).

Maulida, T., Wirasatriya, A., Ismunarti, D. H., & Puryajati, A. D. (2022). Physical drivers of the 2013 marine heatwave in the seas of the southern Java-Nusa Tenggera. *Geographia Technica*, *17*, 129–139. doi: 10.21163/GT_2022.171.10

McAdam, R., Masina, S., & Gualdi, S. (2022). Seasonal forecasting of subsurface marine heat waves. *Submitted to Nature Communications*(2023), 1–11. doi: 10.1038/s43247-023-00892-5

Moore, J. K., Doney, S. C., & Lindsay, K. (2004). Upper ocean ecosystem dynamics and iron cycling in a global three-dimensional model. *Global Biogeochemical Cycles*, *18*(4), 1–21. doi: 10.1029/2004GB002220

Moore, J. K., Lindsay, K., Doney, S. C., Long, M. C., & Misumi, K. (2013). Marine ecosystem dynamics and biogeochemical cycling in the community earth system model [CESM1(BGC)]: Comparison of the 1990s with the 2090s under the RCP4.5 and RCP8.5 scenarios. *Journal of Climate*, *26*(23), 9291–9312. doi: 10.1175/JCLI-D-12-00566.1

Morrison, A. K., Frölicher, T. L., & Sarmiento, J. L. (2015). Upwelling in the Southern Ocean. *Physics Today*, *68*(1), 27–32. doi: 10.1063/PT.3.2654

Müller, J. D. (2023). *RECCAP2-ocean data collection* [Dataset]. Zenodo. Retrieved 2024-05-08, from `https://zenodo.org/records/7990823` doi: 10.5281/zenodo.7990823

Nam, S., Kim, H. J., & Send, U. (2011). Amplification of hypoxic and acidic events by la Niña conditions on the continental shelf off California. *Geophysical Research Letters*, *38*(22), 1–5. doi: 10.1029/2011GL049549

Negrete-García, G., Lovenduski, N. S., Hauri, C., Krumhardt, K. M., & Lauvset, S. K. (2019). Sudden emergence of a shallow aragonite saturation horizon in the Southern Ocean. *Nature Climate Change*, *9*(4), 313–317. doi: 10.1038/s41558-019-0418-8

Oliver, E. C., Benthuysen, J. A., Darmaraki, S., Donat, M. G., Hobday, A. J., Holbrook, N. J., ... Gupta, A. S. (2021). Marine Heatwaves. *Annual Review of Marine Science*, *13*(1), 1–30. doi: 10.1146/annurev-marine-032720-095144

Oliver, E. C., Donat, M. G., Burrows, M. T., Moore, P. J., Smale, D. A., Alexander, L. V., ... Wernberg, T. (2018). Longer and more frequent marine heatwaves over the past century. *Nature Communications*, *9*(1), 1–12. doi: 10.1038/s41467-018-03732-9

Orr, J. C., & Epitalon, J. M. (2015). Improved routines to model the ocean carbonate system: Mocsy 2.0. *Geoscientific Model Development*, *8*(3), 485–499. doi: 10.5194/gmd-8-485-2015

Orr, J. C., Fabry, V. J., Aumont, O., Bopp, L., Doney, S. C., Feely, R. A., ... Yool, A. (2005). Anthropogenic ocean acidification over the twenty-first century and its impact on calcifying organisms. *Nature*, *437*, 681–686. doi: 10.1038/nature04095

Pan, T. C., Applebaum, S. L., & Manahan, D. T. (2015). Experimental ocean acidification alters the allocation of metabolic energy. *Proceedings of the National Academy of Sciences of the United States of America*, *112*(15), 4696–4701. doi: 10.1073/pnas.1416967112

Paulmier, A., & Ruiz-Pino, D. (2009). Oxygen minimum zones (OMZs) in the modern ocean. *Progress in Oceanography*, *80*(3-4), 113–128. Retrieved from `http://dx.doi.org/10.1016/j.pocean.2008.08.001` doi: 10.1016/j.pocean.2008.08.001

Paulmier, A., Ruiz-Pino, D., & Garçon, V. (2011). CO2 maximum in the oxygen minimum zone (OMZ). *Biogeosciences*, *8*(2), 239–252. doi: 10.5194/bg-8-239-2011

Pellichero, V., Sallée, J.-B., Schmidtko, S., Roquet, F., & Charrassin, J.-B. (2017). The ocean mixed layer under Southern Ocean sea-ice: Seasonal cycle and forcing. *Journal of Geophysical Research: Oceans*, *122*(2), 1608–1633. doi: 10.1002/2016JC011970

Pirotta, E., Thomas, L., Costa, D. P., Hall, A. J., Harris, C. M., Harwood, J., ... Tyack, P. L. (2022). Understanding the combined effects of multiple stressors: A new perspective on a longstanding challenge. *Science of the Total Environment*, *821*, 153322. doi: 10.1016/j.scitotenv.2022.153322

Pörtner, H. O. (2002). Climate variations and the physiological basis of temperature dependent biogeography: Systemic to molecular hierarchy of thermal tolerance in animals. *Comparative Biochemistry and Physiology - A Molecular and Integrative Physiology*, *132*(4), 739–761. doi: 10.1016/S1095-6433(02)00045-4

Pörtner, H. O., & Knust, R. (2007). Climate Change Affects Marine Fishes Through the Oxygen Limitation of Thermal Tolerance. *Science*, *315*, 95–97. doi: 10.1259/0007-1285-53-633-920-b

Qi, R., Zhang, Y., Du, Y., & Feng, M. (2022). Characteristics and Drivers of Marine Heatwaves in the Western Equatorial Indian Ocean. *Journal of Geophysical Research: Oceans*, *127*(10), e2022JC018732. doi: 10.1029/2022JC018732

Ramadhan, A., Marshall, J., Meneghello, G., Illari, L., & Speer, K. (2022). Observations of Upwelling and Downwelling Around Antarctica Mediated by Sea Ice. *Frontiers in Marine Science*, *9*. doi: 10.3389/fmars.2022.864808

Righetti, D., Vogt, M., Gruber, N., Psomas, A., & Zimmermann, N. E. (2019). Global pattern of phytoplankton diversity driven by temperature and environ-

mental variability. *Science Advances*, *5*(5). doi: 10.1126/sciadv.aau6253

Riquelme-Bugueño, R., Pérez-Santos, I., Alegría, N., Vargas, C. A., Urbina, M. A., & Escribano, R. (2020). Diel vertical migration into anoxic and high-pCO2 waters: acoustic and net-based krill observations in the Humboldt Current. *Scientific Reports*, *10*(1), 1–11. doi: 10.1038/s41598-020-73702-z

Ritz, D. A., Hobday, A. J., Montgomery, J. C., & Ward, A. J. W. (2011). Chapter Four - Social Aggregation in the Pelagic Zone with Special Reference to Fish and Invertebrates. In M. Lesser (Ed.), *Advances in Marine Biology* (Vol. 60, pp. 161–227). Academic Press. doi: 10.1016/B978-0-12-385529-9.00004-4

Rose, K., Gutiérrez, D., Breitburg, D., Conley, D., Craig, K., Froehlich, H., ... Prema, D. (2019). Impacts of ocean deoxygenation on fisheries. In *'Laffoley, D. & Baxter, J.M. (eds.) (2019). Ocean deoxygenation: Everyone's problem - Causes, impacts, consequences and solutions.* (pp. 519–544). IUCN, Gland, Switzerland. doi: 10.2305/IUCN.CH.2019.13.en

Rosselló, P., Pascual, A., & Combes, V. (2023). Assessing marine heat waves in the Mediterranean Sea: a comparison of fixed and moving baseline methods. *Frontiers in Marine Science*, *10*, 1168368. doi: 10.3389/fmars.2023.1168368

Roy, C., & Reason, C. (2001). ENSO related modulation of coastal upwelling in the eastern Atlantic. *Progress in Oceanography*, *49*(1-4), 245–255. doi: 10.1016/S0079-6611(01)00025-8

Sallée, J. B., Speer, K. G., & Rintoul, S. R. (2010, April). Zonally asymmetric response of the Southern Ocean mixed-layer depth to the Southern Annular Mode. *Nature Geoscience*, *3*(4), 273–279. Retrieved 2024-02-29, from `https://www.nature.com/articles/ngeo812` (Publisher: Nature Publishing Group) doi: 10.1038/ngeo812

Samuels, T., Rynearson, T. A., & Collins, S. (2021). Surviving Heatwaves: Thermal Experience Predicts Life and Death in a Southern Ocean Diatom. *Frontiers in Marine Science*, *8*. doi: 10.3389/fmars.2021.600343

Santoso, A., Mcphaden, M. J., & Cai, W. (2017). The Defining Characteristics of ENSO Extremes and the Strong 2015/2016 El Niño. *Reviews of Geophysics*, *55*(4), 1079–1129. doi: 10.1002/2017RG000560

Sarmiento, J. L., & Gruber, N. (2006). *Ocean Biogeochemical Dynamics*. Princeton University Press. doi: 10.2307/j.ctt3fgxqx

Scannell, H. A., Johnson, G. C., Thompson, L., Lyman, J. M., & Riser, S. C. (2020). Subsurface Evolution and Persistence of Marine Heatwaves in the Northeast Pacific. *Geophysical Research Letters*, *47*(23), 1–10. doi: 10.1029/2020GL090548

Schaeffer, A., & Roughan, M. (2017). Subsurface intensification of marine heatwaves off southeastern Australia: The role of stratification and local winds. *Geophysical Research Letters*, *44*(10), 5025–5033. doi: 10.1002/2017GL073714

Seibel, B. A. (2011). Critical oxygen levels and metabolic suppression in oceanic oxygen minimum zones. *Journal of Experimental Biology*, *214*(2), 326–336. doi: 10.1242/jeb.049171

Seibel, B. A., Schneider, J. L., Kaartvedt, S., Wishner, K. F., & Daly, K. L. (2016). Hypoxia Tolerance and Metabolic Suppression in Oxygen Minimum Zone Euphausiids: Implications for Ocean Deoxygenation and Biogeochemical Cycles. *Integrative and Comparative Biology*, *56*(4), 510–523. doi: 10.1093/icb/icw091

Sen Gupta, A. (2023). *Marine heatwaves: definition duel heats up.*

Sen Gupta, A., Thomsen, M., Benthuysen, J. A., Hobday, A. J., Oliver, E., Alexander, L. V., ... Smale, D. A. (2020). Drivers and impacts of the most extreme marine heatwaves events. *Scientific Reports*, *10*(1), 1–15. doi: 10.1038/s41598-020-75445-3

Sharp, J. D., Fassbender, A. J., Carter, B. R., Johnson, G. C., Schultz, C., & Dunne, J. P. (2022). GOBAI-O $_2$: temporally and spatially resolved fields

of ocean interior dissolved oxygen over nearly two decades. doi: 10.5194/essd-2022-308

Smale, D. A., Wernberg, T., Oliver, E. C. J., Thomsen, M., Harvey, B. P., Straub, S. C., ... Moore, P. J. (2019). Marine heatwaves threaten global biodiversity and the provision of ecosystem services. *Nature Climate Change*, *9*(4), 306–312. doi: 10.1038/s41558-019-0412-1

Smith, K. E., Burrows, M. T., Hobday, A. J., King, N. G., Moore, P. J., Sen Gupta, A., ... Smale, D. A. (2023). Biological Impacts of Marine Heatwaves. *Annual review of marine science*, *15*, 119–145. doi: 10.1146/annurev-marine-032122-121437

Smith, R., & Gent, P. (2010). *The Parallel Ocean Program (POP) reference manual* (Tech. Rep.). National Center for Atmospheric Research Boulder, Colorado: National Center for Atmospheric Research Boulder, Colorado.

Stabeno, P. J., & Bell, S. W. (2019). Extreme Conditions in the Bering Sea (2017–2018): Record-Breaking Low Sea-Ice Extent. *Geophysical Research Letters*, *46*(15), 8952–8959. doi: 10.1029/2019GL083816

Stuart-Smith, R. D., Bates, A. E., Lefcheck, J. S., Duffy, J. E., Baker, S. C., Thomson, R. J., ... Edgar, G. J. (2013). Integrating abundance and functional traits reveals new global hotspots of fish diversity. *Nature*, *501*(7468), 539–542. doi: 10.1038/nature12529

Susanto, R. D., Gordon, A. L., & Zheng, Q. (2001). Upwelling along the coasts of Java and Sumatra and its relation to ENSO. *Geophysical Research Letters*, *28*(8), 1599–1602. doi: 10.1029/2000GL011844

Tai, T. C., Sumaila, U. R., & Cheung, W. W. (2021). Ocean Acidification Amplifies Multi-Stressor Impacts on Global Marine Invertebrate Fisheries. *Frontiers in Marine Science*, *8*, 1–12. doi: 10.3389/fmars.2021.596644

Tamsitt, V., Drake, H. F., Morrison, A. K., Talley, L. D., Dufour, C. O., Gray, A. R., ... Weijer, W. (2017). Spiraling pathways of global deep waters to the surface of the Southern Ocean. *Nature Communications*, *8*(1), 1–10. doi: 10.1038/s41467-017-00197-0

Tittensor, D. P., Mora, C., Jetz, W., Lotze, H. K., Ricard, D., Berghe, E. V., & Worm, B. (2010). Global patterns and predictors of marine biodiversity across taxa. *Nature*, *466*(7310). doi: 10.1038/nature09329

Turi, G., Alexander, M., Lovenduski, N. S., Capotondi, A., Scott, J., Stock, C., ... Jacox, M. (2018). Response of O_2 and pH to ENSO in the California Current System in a high-resolution global climate model. *Ocean Science*, *14*(1), 69–86. doi: 10.5194/os-14-69-2018

Vogt, L., Burger, F. A., Griffies, S. M., & Frölicher, T. L. (2022). Local Drivers of Marine Heatwaves: A Global Analysis With an Earth System Model. *Frontiers in Climate*, *4*. doi: 10.3389/fclim.2022.847995

Wang, Y., Zhou, M., Zhang, Z., & Dinniman, M. S. (2023). Seasonal variations in Circumpolar Deep Water intrusions into the Ross Sea continental shelf. *Frontiers in Marine Science*, *10*.

Watson, R. A. (2017). A database of global marine commercial, small-scale, illegal and unreported fisheries catch 1950–2014. *Scientific Data*, *4*(1), 170039. doi: 10.1038/sdata.2017.39

Wilson, E. A., Riser, S. C., Campbell, E. C., & Wong, A. P. (2019). Winter upper-ocean stability and ice-ocean feedbacks in the sea ice-covered Southern Ocean. *Journal of Physical Oceanography*, *49*(4), 1099–1117. doi: 10.1175/JPO-D-18-0184.1

Wong, J., Gruber, N., & Münnich, M. (2024). *Column-Compound Extremes in the Global Ocean* [Dataset]. ETH Research Collection. doi: 10.3929/ethz-b-000654113

Worm, B., & Tittensor, D. P. (2018). *A theory of global biodiversity* (No. 60). Princeton, New Jersey: Princeton University Press.

Xu, K., Huang, R. X., Wang, W., Zhu, C., & Lu, R. (2017). Thermocline fluctuations in the equatorial pacific related to the two types of El Niño events. *Journal of Climate*, *30*(17), 6611–6627. doi: 10.1175/JCLI-D-16-0291.1

Yang, S., & Gruber, N. (2016). The anthropogenic perturbation of the marine nitrogen cycle by atmospheric deposition: Nitrogen cycle feedbacks and the 15N Haber-Bosch effect. *Global Biogeochemical Cycles*, *30*(10), 1418–1440. doi: 10.1002/2016GB005421

Zeebe, R. E., & Wolf-Gladrow, D. (2001). *CO2 in seawater : equilibrium, kinetics, isotopes*. Burlington: Elsevier Burlington.

Zhang, Y., Du, Y., Feng, M., & Hu, S. (2021). Long-Lasting Marine Heatwaves Instigated by Ocean Planetary Waves in the Tropical Indian Ocean During 2015–2016 and 2019–2020. *Geophysical Research Letters*, *48*(21), e2021GL095350. doi: 10.1029/2021GL095350

Zscheischler, J., & Seneviratne, S. I. (2017). Dependence of drivers affects risks associated with compound events. *Science Advances*, *3*(6), 1–11. doi: 10.1126/sciadv.1700263

Zuo, H., Balmaseda, M. A., Tietsche, S., Mogensen, K., & Mayer, M. (2019). The ECMWF operational ensemble reanalysis–analysis system for ocean and sea ice: a description of the system and assessment. *Ocean Science*, *15*(3), 779–808. doi: 10.5194/os-15-779-2019

(a)

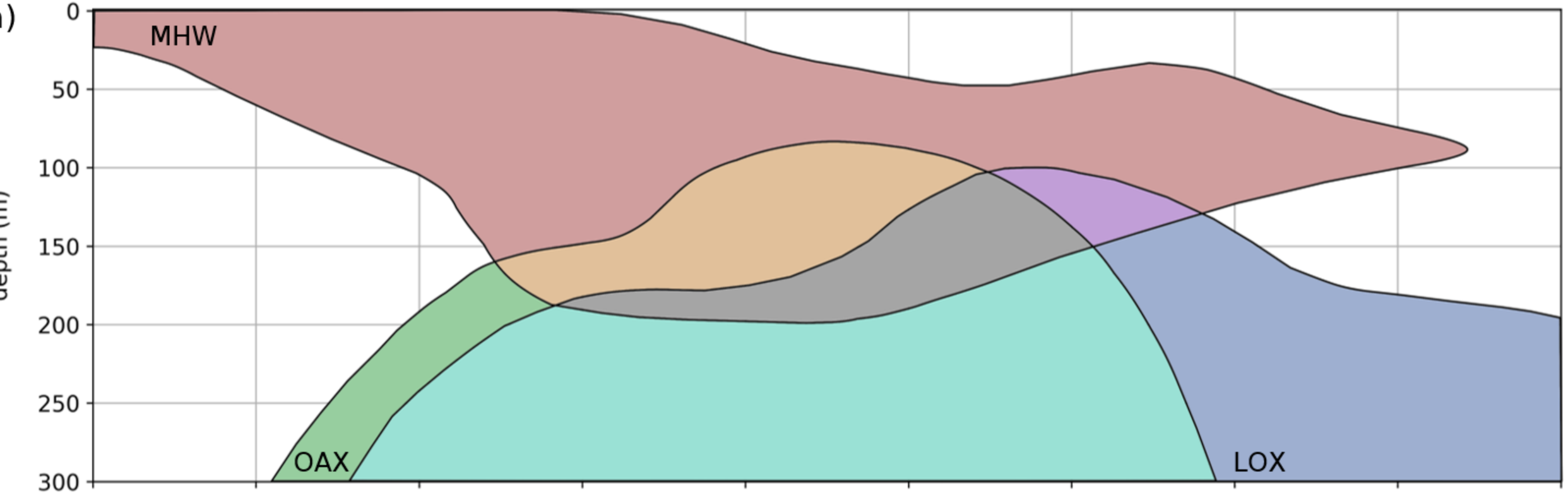
MHW
OAX
LOX
depth (m)
0
50
100
150
200
250
300

(b)

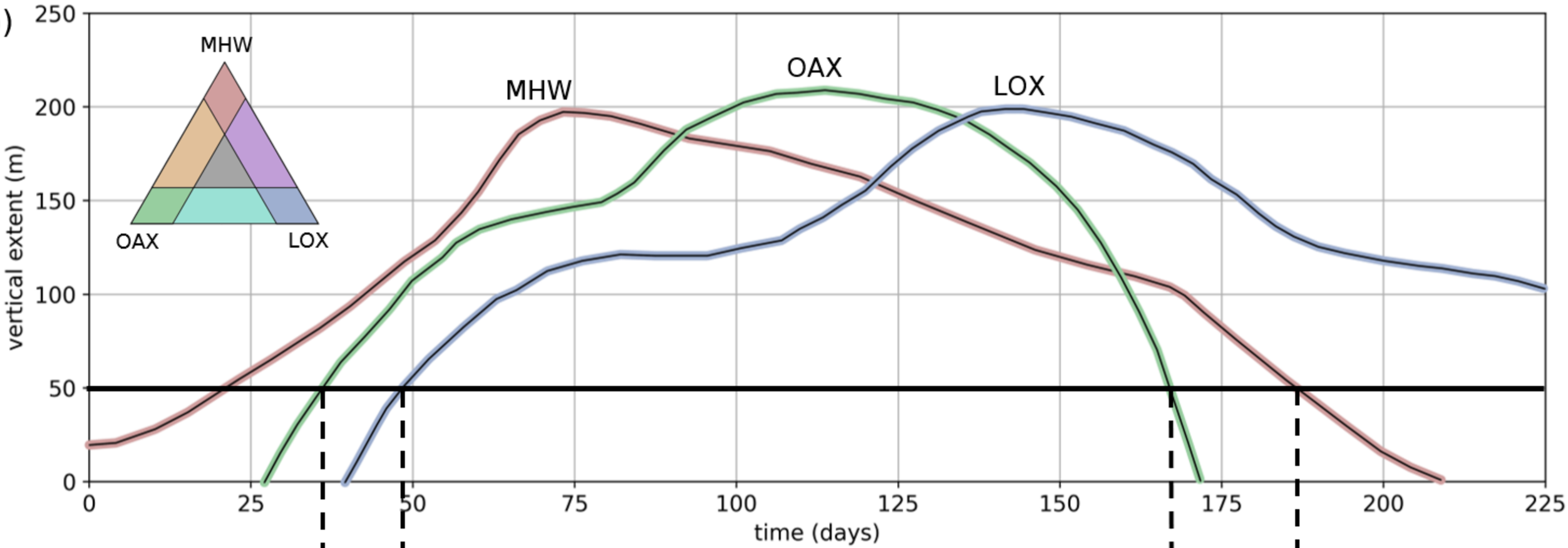
MHW
OAX
LOX
vertical extent (m)
time (days)
0
25
50
75
100
125
150
175
200
225
250
200
150
100
50
0


CCX duration
MHW-OAX
MHW-LOX
OAX-LOX
MHW-OAX-LOX

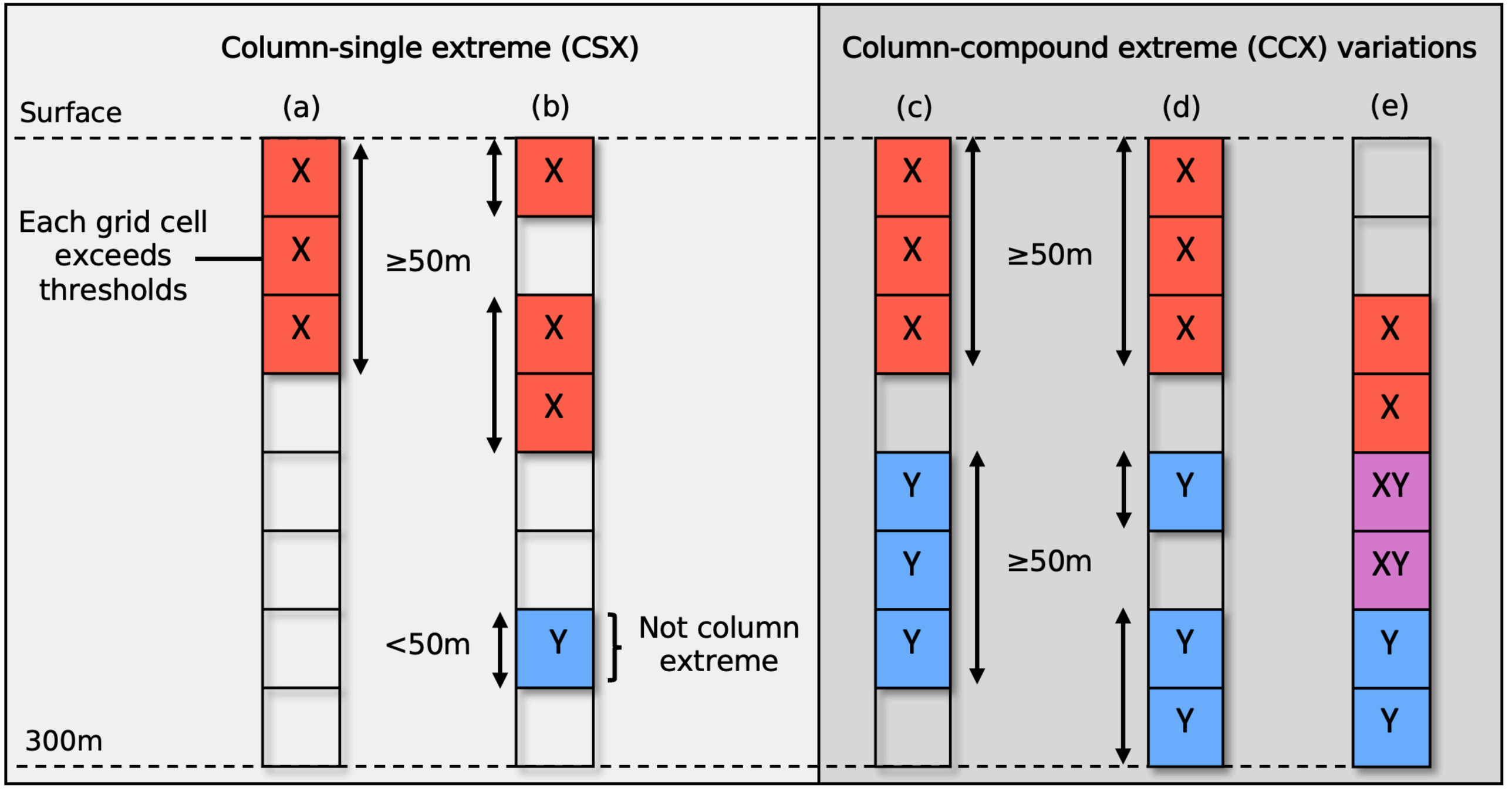
Column-single extreme (CSX)
Column-compound extreme (CCX) variations
Surface
(a)
(b)
(c)
(d)
(e)
Each grid cell exceeds thresholds
X
Y
≥50m
<50m
Not column extreme
300m

(a)

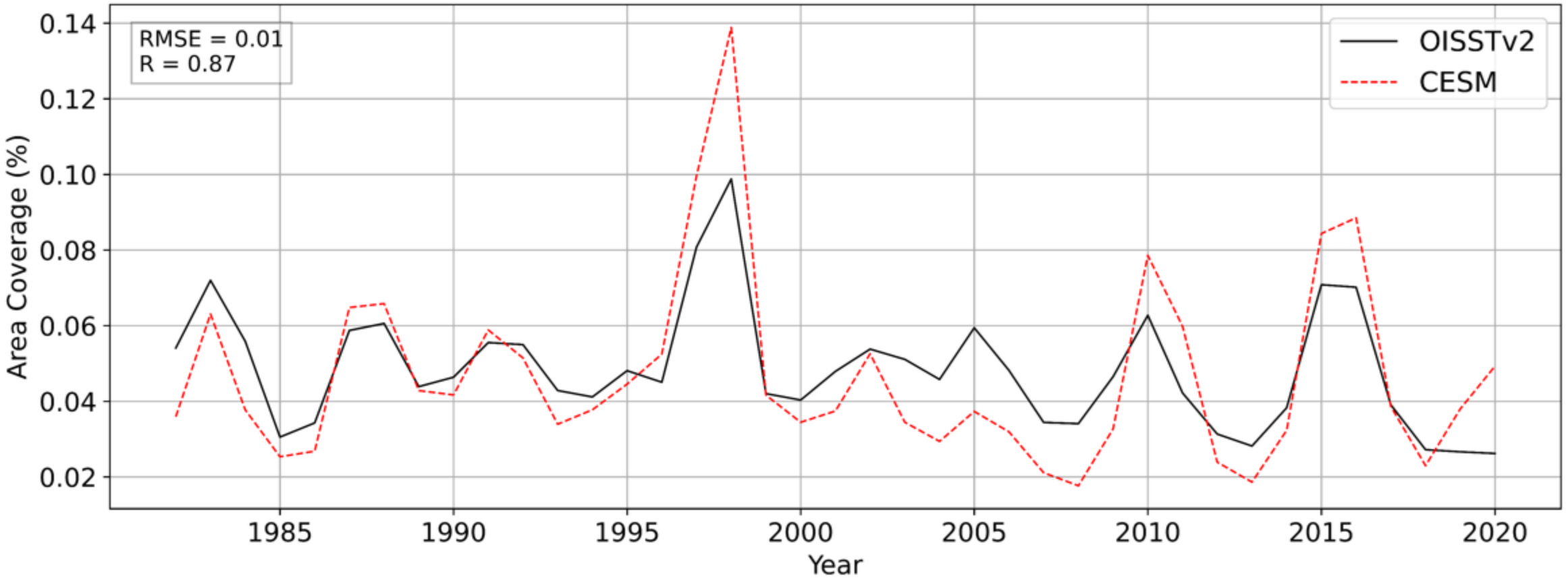
RMSE = 0.01
R = 0.87
OISSTv2
CESM
Area Coverage (%)
0.14
0.12
0.10
0.08
0.06
0.04
0.02
1985
1990
1995
2000
2005
2010
2015
2020
Year

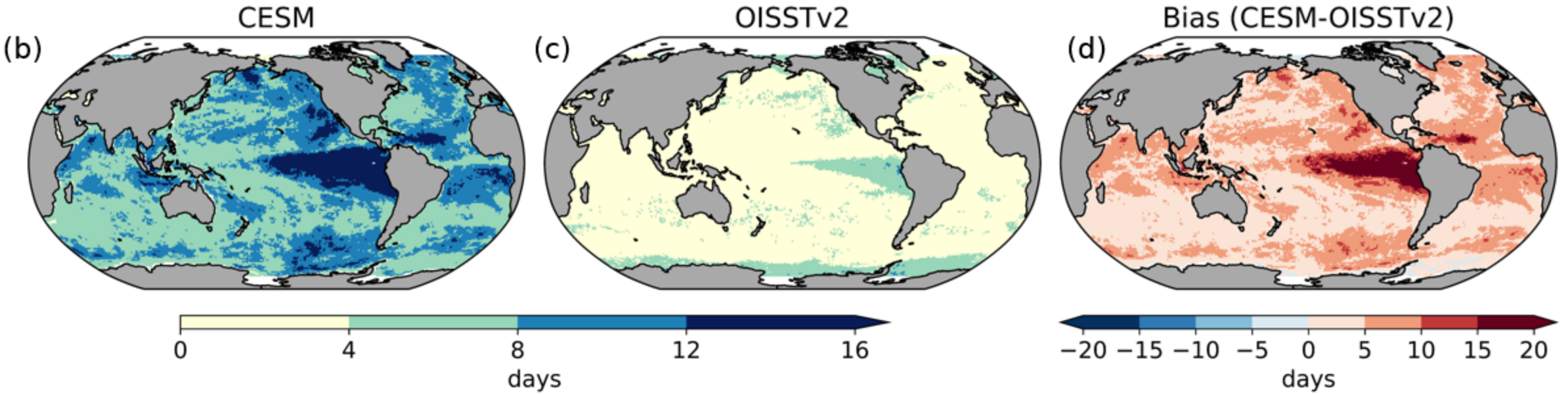
(b)
CESM
(c)
OISSTv2
(d)
Bias (CESM-OISSTv2)
0
4
8
12
16
days
−20 −15 −10 −5 0 5 10 15 20
days
(e)
(f)
(g)
0.0
0.3
0.6
0.9
1.2
1.5
°C
−0.6 −0.4 −0.2 0.0 0.2 0.4 0.6
°C

(a)

RMSE = 0.02
R = 0.69

OceanSoda-ETHZ
CESM

Area Coverage (%)

0.12
0.10
0.08
0.06
0.04
0.02

1985 1990 1995 2000 2005 2010 2015 2020

Year

CESM

(b)

OceanSODA-ETHZ

(c)

Bias (CESM-OceanSODA)

(d)

1 2 3 4 5 6

months

−4 −3 −2 −1 0 1 2 3 4

months

(e)

(f)

(g)

0.00 0.04 0.08 0.12 0.16 0.20

µmol/m^3

−0.16 −0.08 0.00 0.08 0.16

µmol/m^3

Fixed Baseline

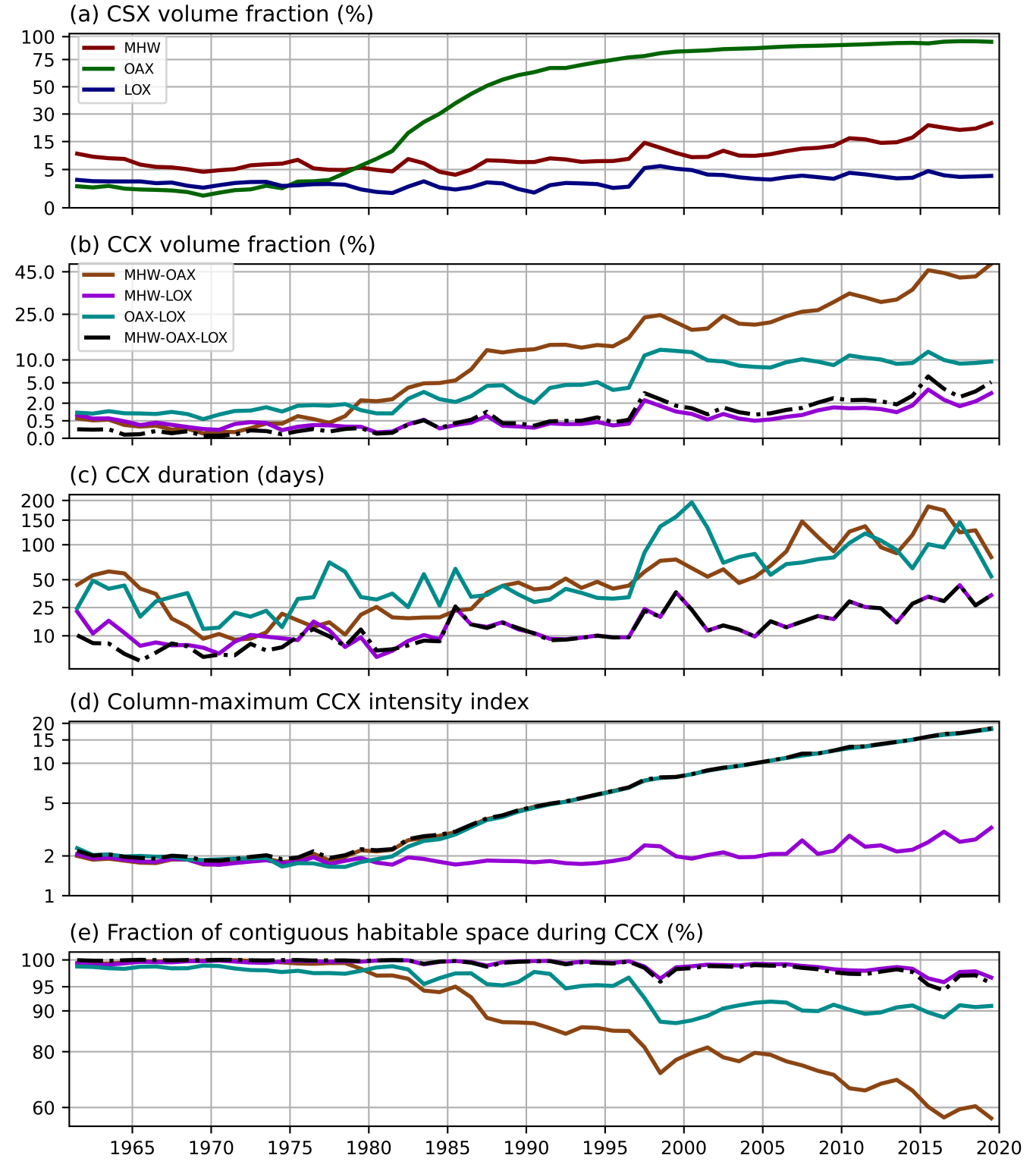

Moving Baseline

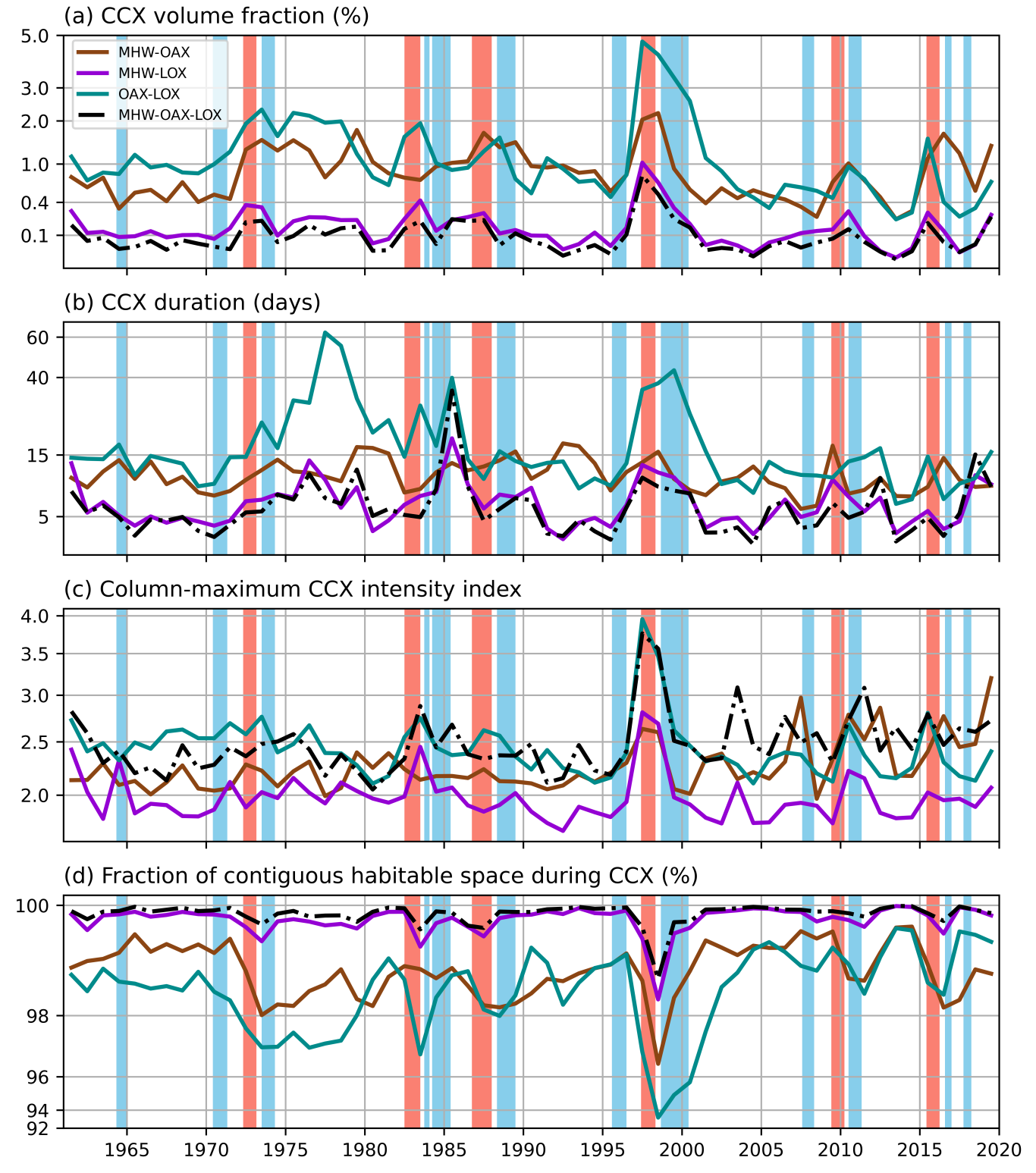

MHW-OAX

(a)

(b)

OAX-LOX

(c)

(d)

MHW-LOX

(e)

(f)

MHW-OAX-LOX

(g)

(h)

0 5 10 15 20 25

Days per year

−1.0 −0.5 0.0 0.5 1.0

Co-occurrence propensity

Key Metrics of the **MHW-OAX** Column-Compound Extreme

(a) Duration

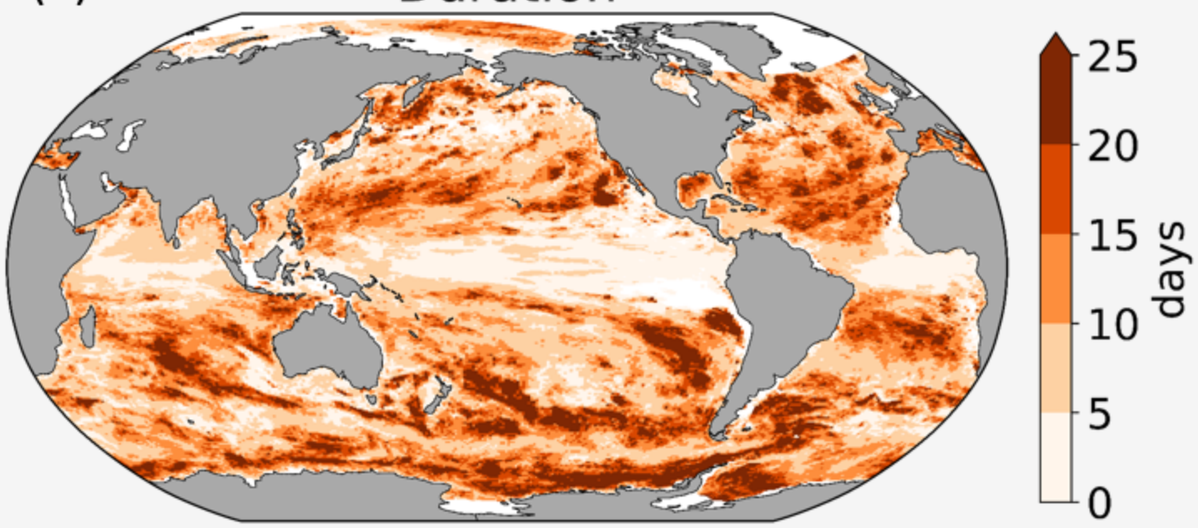

(b) Intensity index

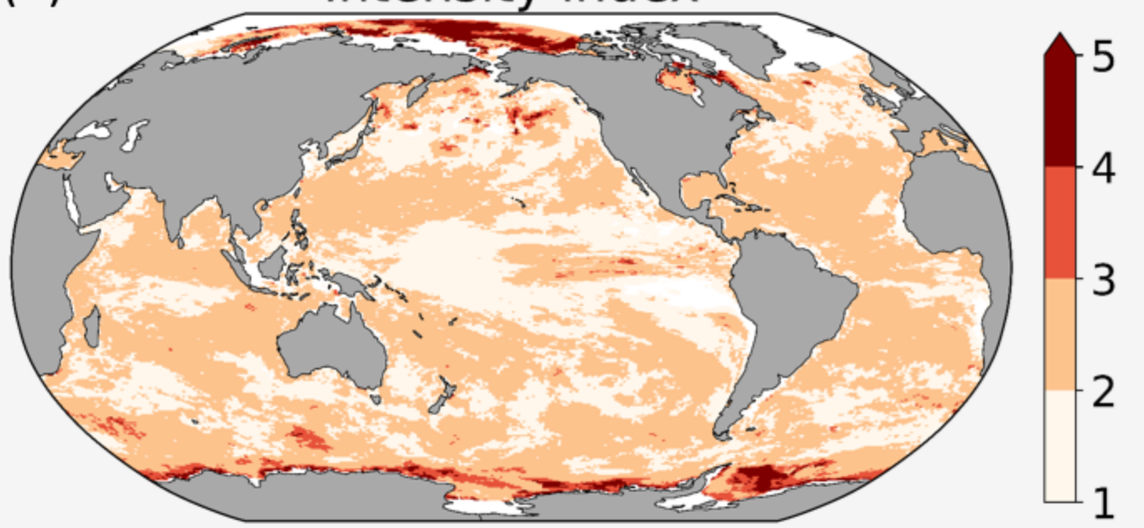

(c) CCX days per year

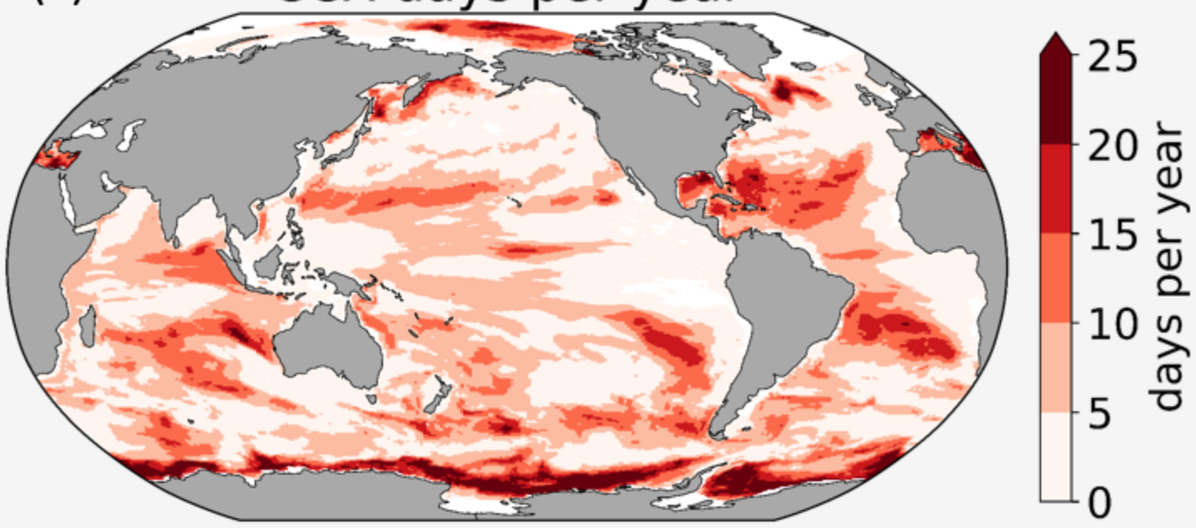

(d) Co-occurrence propensity

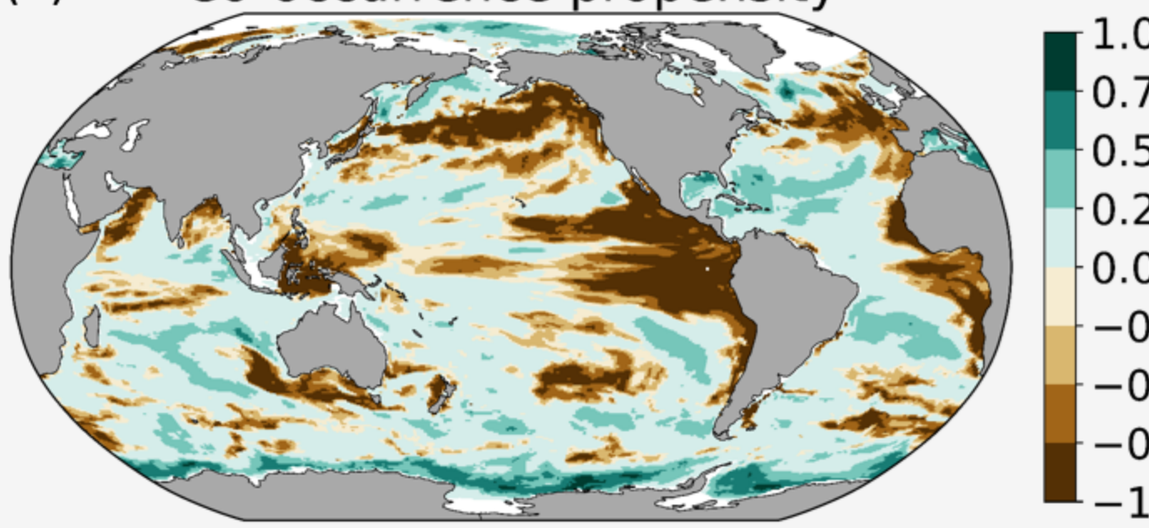

(e) Vertical fraction

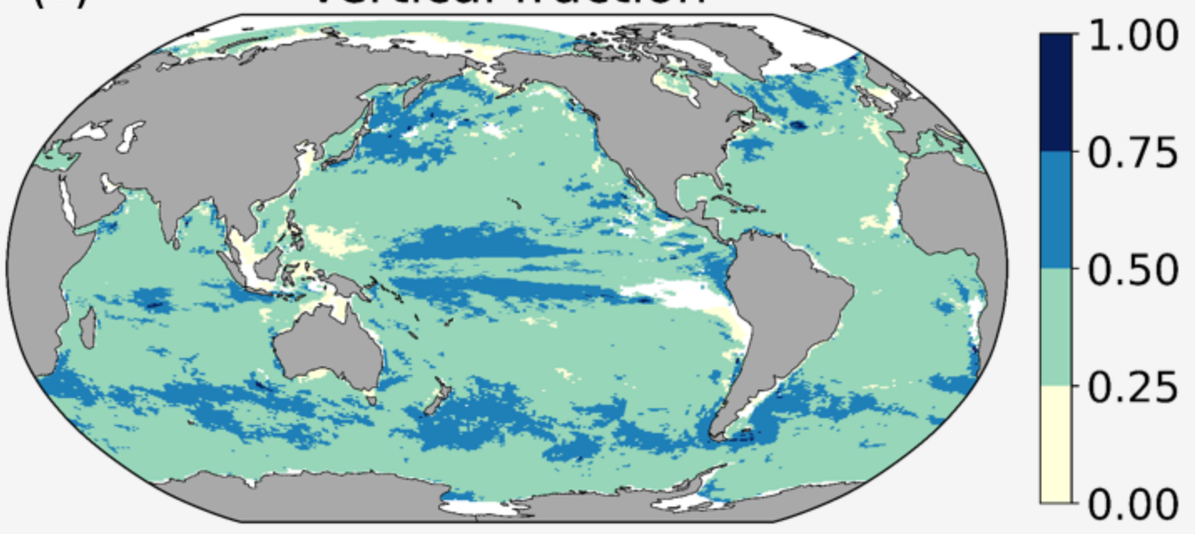

(f) Contiguous habitable space

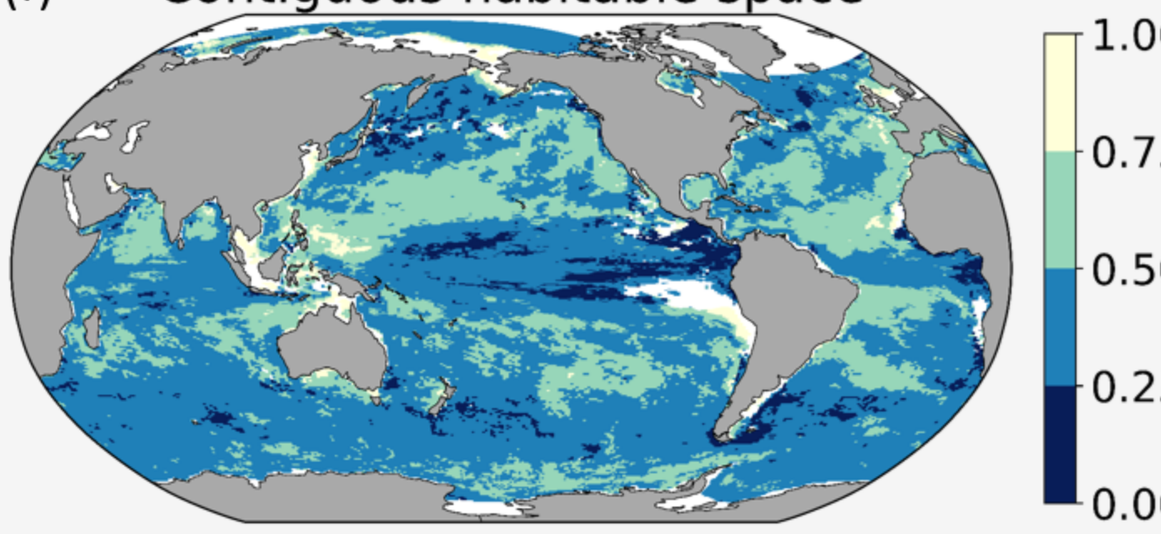

Key Metrics of the **MHW-OAX-LOX** Column-Compound Extreme

(a) Duration

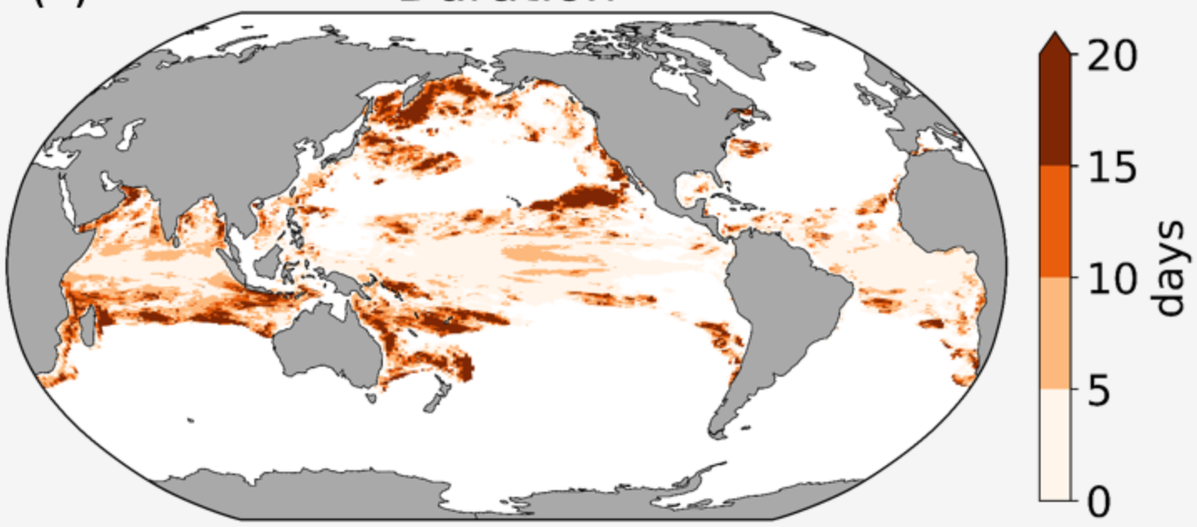

(b) Intensity index

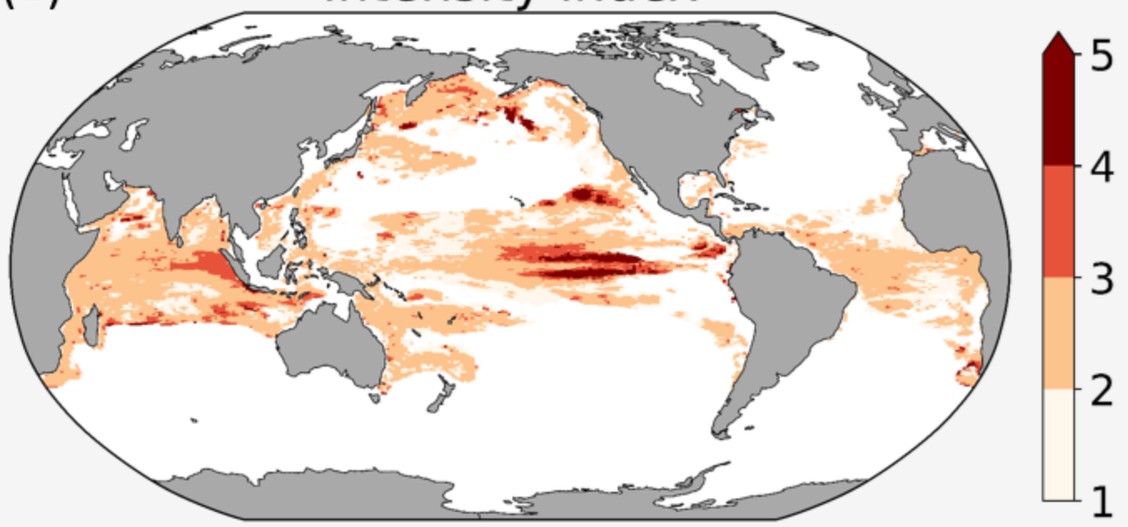

(c) CCX days per year

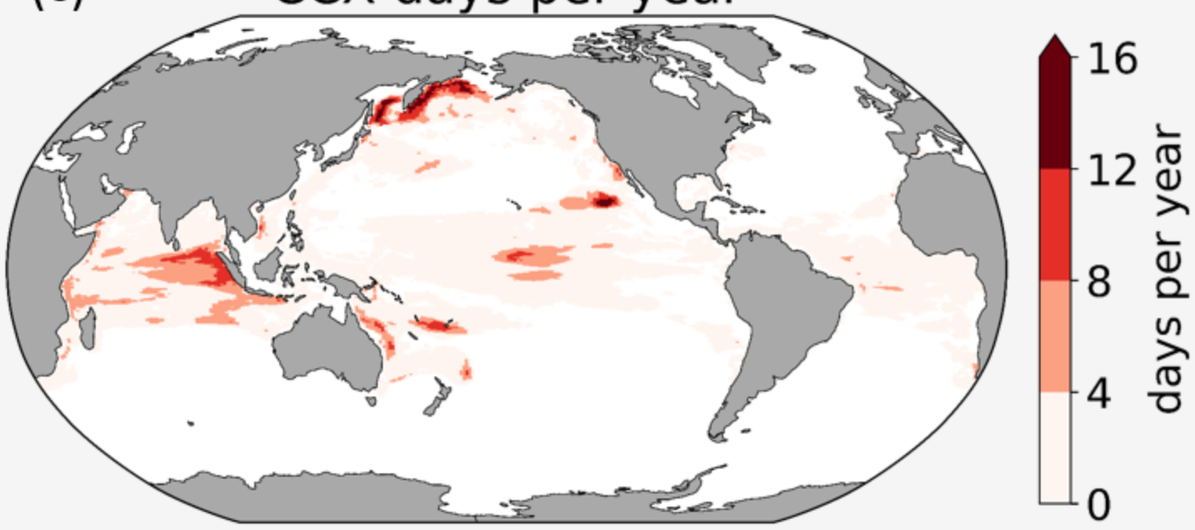

(d) Co-occurrence propensity

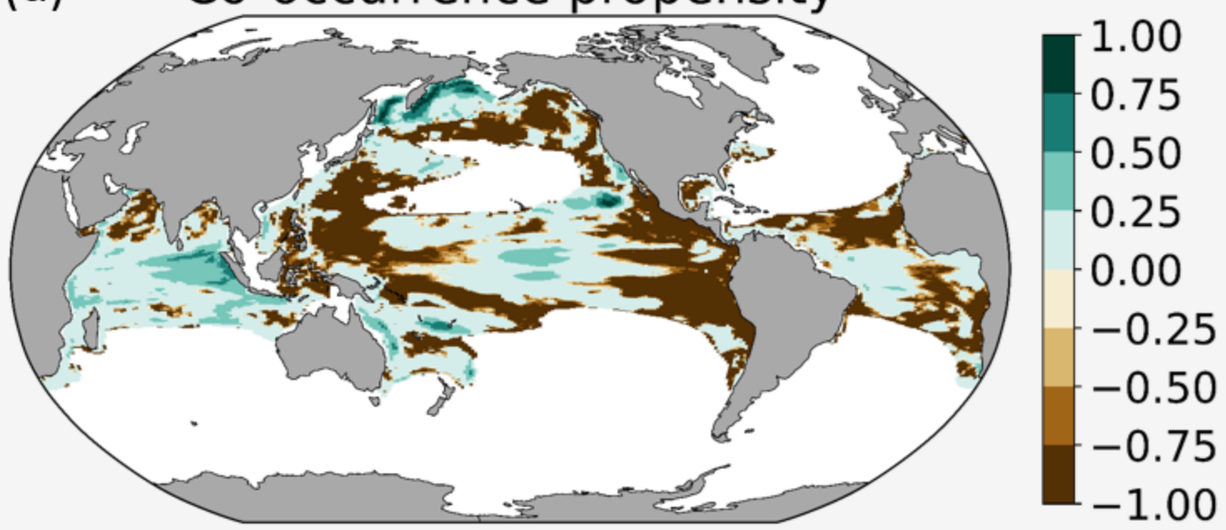

(e) Vertical fraction

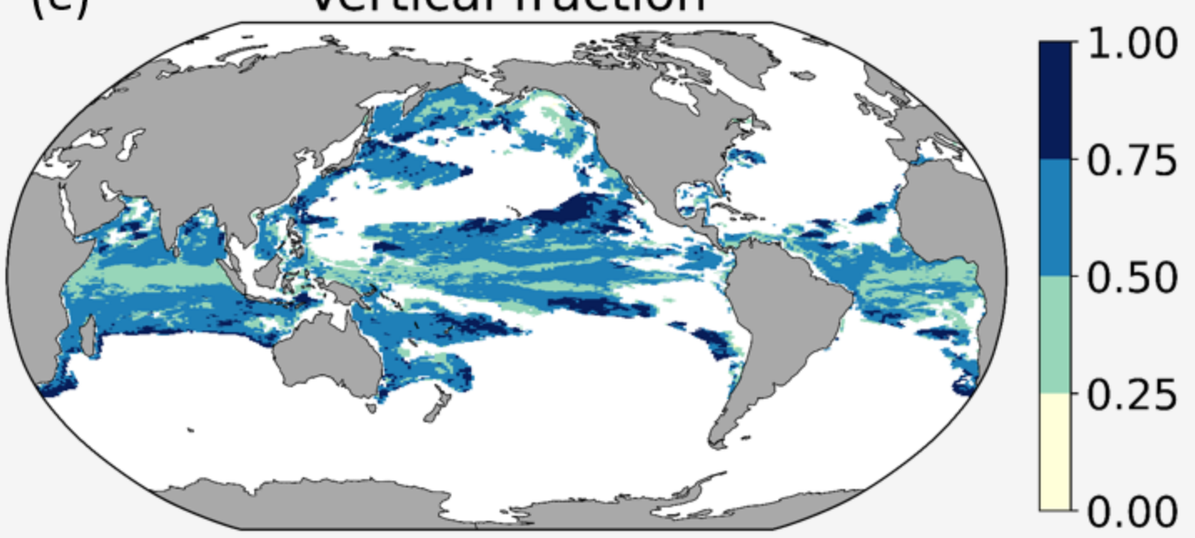

(f) Contiguous habitable space

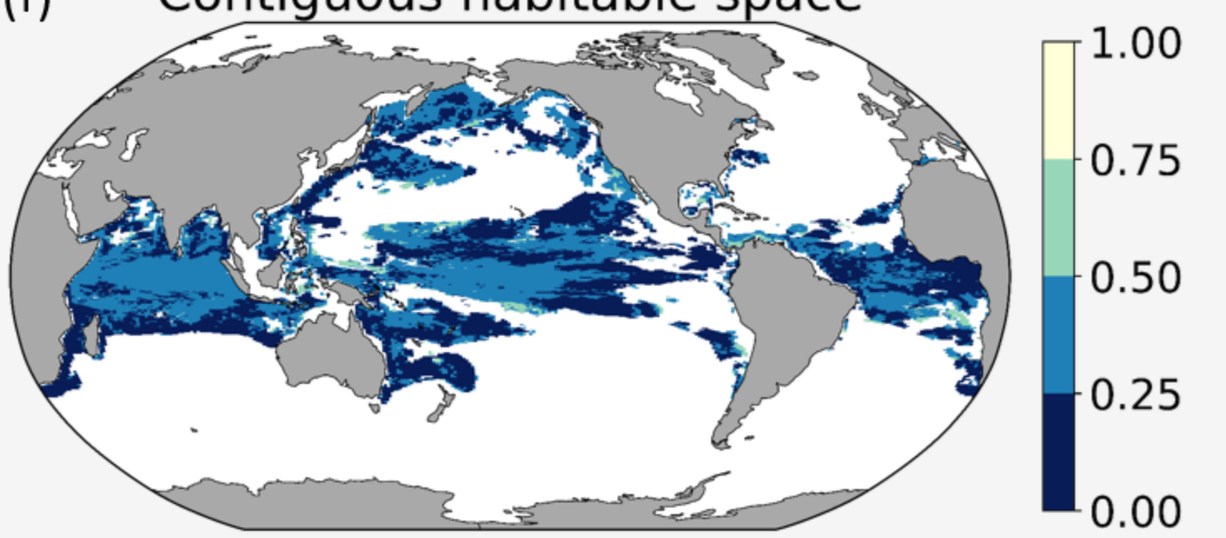

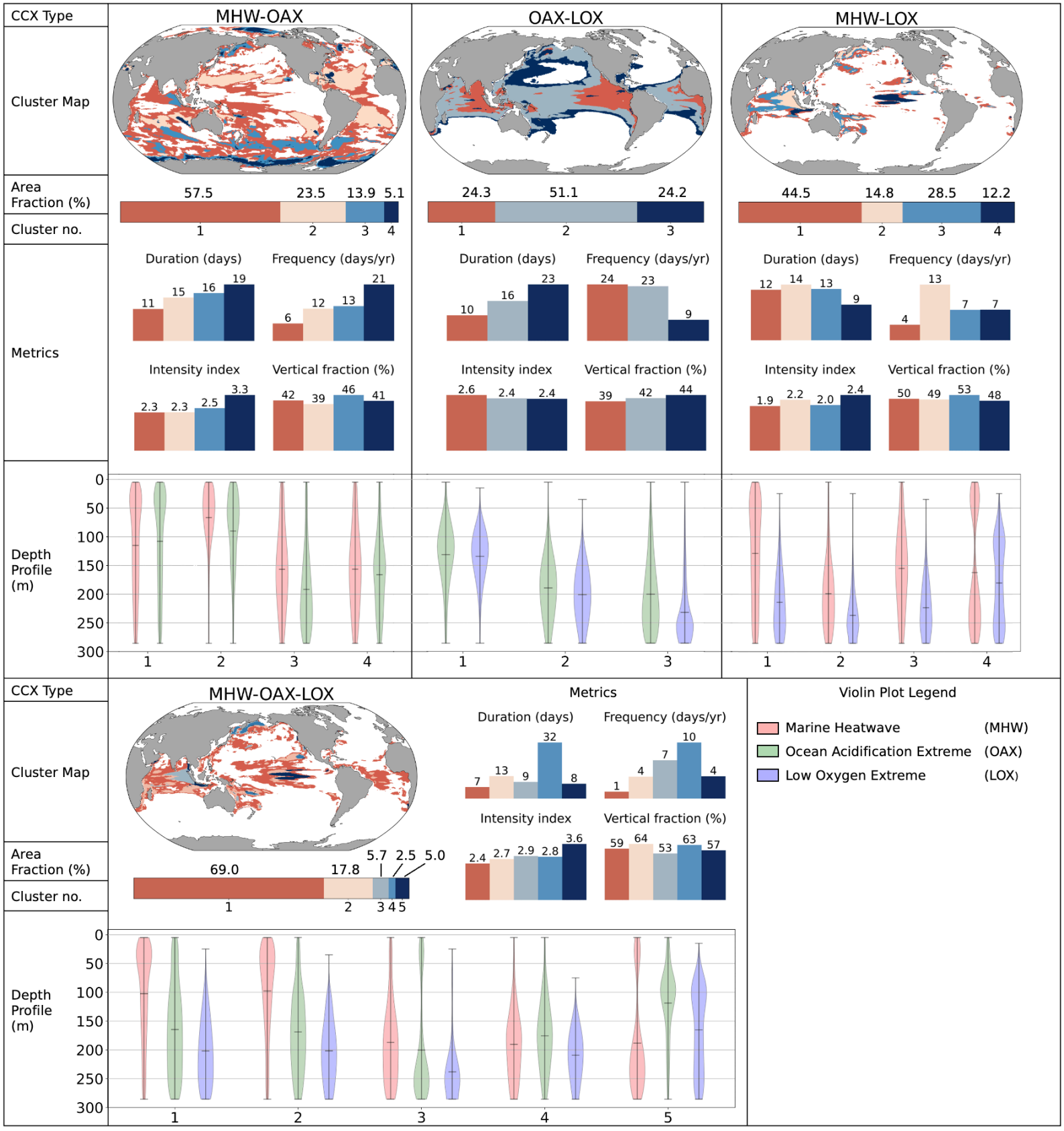
CCX Type
MHW-OAX
OAX-LOX
MHW-LOX
Cluster Map
Area Fraction (%)
57.5 23.5 13.9 5.1
24.3 51.1 24.2
44.5 14.8 28.5 12.2
Cluster no.
1 2 3 4
1 2 3
1 2 3 4
Metrics
Duration (days)
11 15 16 19
10 16 23
12 14 13 9
Frequency (days/yr)
6 12 13 21
24 23 9
4 13 7 7
Intensity index
2.3 2.3 2.5 3.3
2.6 2.4 2.4
1.9 2.2 2.0 2.4
Vertical fraction (%)
42 39 46 41
39 42 44
50 49 53 48
Depth Profile (m)
0 50 100 150 200 250 300
1 2 3 4
1 2 3
1 2 3 4
CCX Type
MHW-OAX-LOX
Cluster Map
Area Fraction (%)
69.0 17.8 5.7 2.5 5.0
Cluster no.
1 2 3 4 5
Metrics
Duration (days)
7 13 9 32 8
Frequency (days/yr)
1 4 7 10 4
Intensity index
2.4 2.7 2.9 2.8 3.6
Vertical fraction (%)
59 64 53 63 57
Depth Profile (m)
0 50 100 150 200 250 300
1 2 3 4 5
Violin Plot Legend
Marine Heatwave (MHW)
Ocean Acidification Extreme (OAX)
Low Oxygen Extreme (LOX)

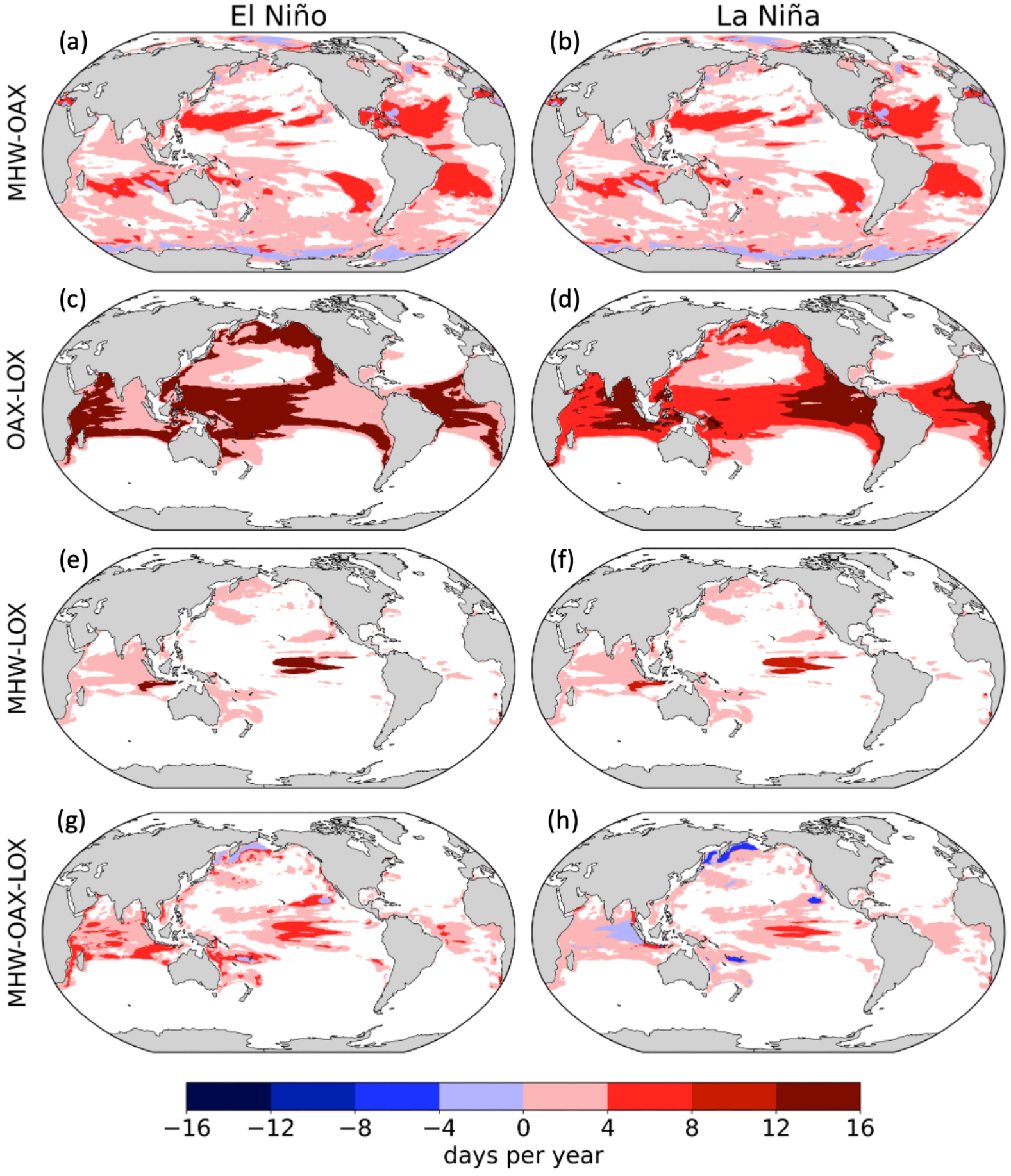
El Niño
La Niña
(a)
(b)
(c)
(d)
(e)
(f)
(g)
(h)
MHW-OAX
OAX-LOX
MHW-LOX
MHW-OAX-LOX
−16
−12
−8
−4
0
4
8
12
16
days per year

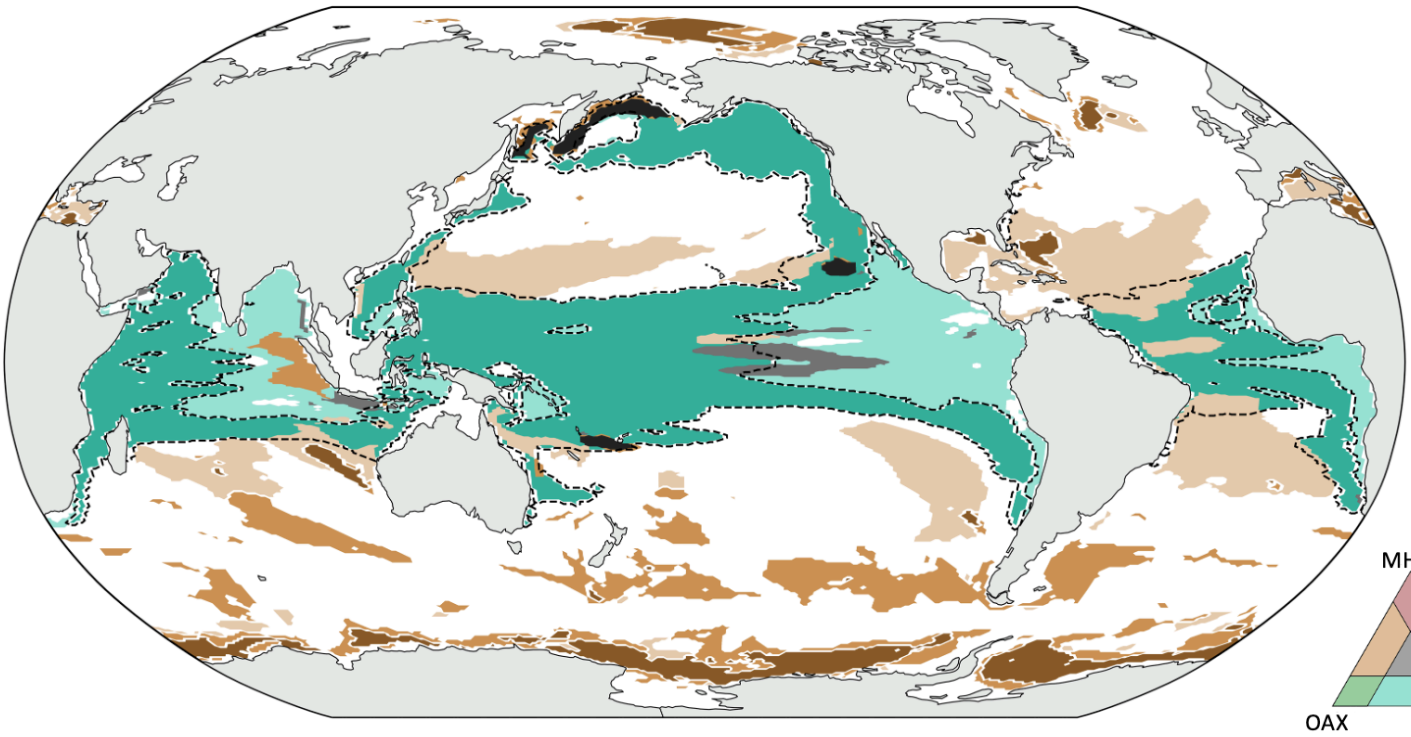

Cluster	MHW-OAX 2	MHW-OAX 3	MHW-OAX 4	OAX-LOX 1	OAX-LOX 2	MHW-OAX-LOX 4	MHW-OAX-LOX 5
Associated Regions	Subtropics, Tropics	Subantarctic	Antarctic	EBUS, East tropics	West tropics, OMZs	Western Subarctic Pacific	Central Tropical Pacific
Time-depth Schematic	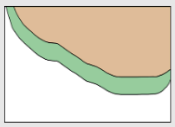	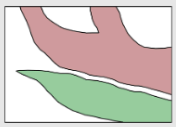	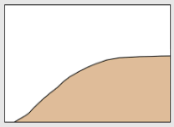	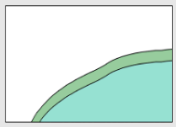		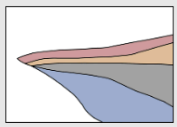	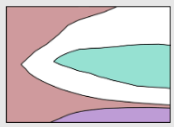
Duration (days)	15 (49)	16 (40)	19 (29)	10 (27)	16 (39)	32 (52)	8 (13)
Frequency (days per year)	12 (81)	13 (58)	21 (50)	24 (67)	23 (53)	10 (20)	4 (16)
Intensity Index	2.3 (11.5)	2.5 (9.7)	3.3 (7.8)	2.6 (5.6)	2.4 (5.9)	2.8 (4.5)	3.6 (5.4)
Vertical Extent (%)	39 (88)	46 (83)	41 (79)	39 (70)	42 (75)	63 (81)	57 (75)
ENSO (+/-) change (days)	+6/+5	+1/+1	-3/-4	+2/+14	+15/+7	-2/-5	+7/+5
Depth Profile (m)